



저작자표시-비영리-변경금지 2.0 대한민국

이용자는 아래의 조건을 따르는 경우에 한하여 자유롭게

- 이 저작물을 복제, 배포, 전송, 전시, 공연 및 방송할 수 있습니다.

다음과 같은 조건을 따라야 합니다:



저작자표시. 귀하는 원저작자를 표시하여야 합니다.



비영리. 귀하는 이 저작물을 영리 목적으로 이용할 수 없습니다.



변경금지. 귀하는 이 저작물을 개작, 변형 또는 가공할 수 없습니다.

- 귀하는, 이 저작물의 재이용이나 배포의 경우, 이 저작물에 적용된 이용허락조건을 명확하게 나타내어야 합니다.
- 저작권자로부터 별도의 허가를 받으면 이러한 조건들은 적용되지 않습니다.

저작권법에 따른 이용자의 권리는 위의 내용에 의하여 영향을 받지 않습니다.

이것은 [이용허락규약\(Legal Code\)](#)을 이해하기 쉽게 요약한 것입니다.

[Disclaimer](#)

Dissertation for the Degree of Doctor of Philosophy

Conjugated Polymer Electrolyte for High-Performance Polymer Solar Cells



by

Sabrina Aufar Salma

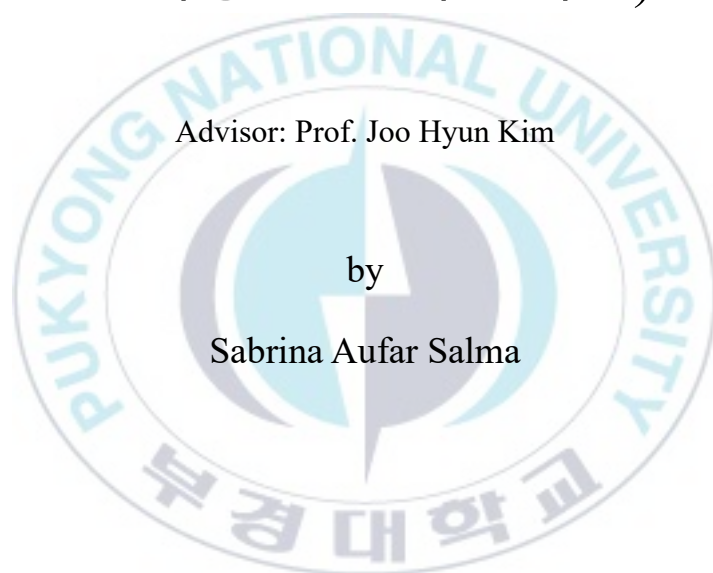
Department of Polymer Engineering

The Graduate School

Pukyong National University

February, 2023

Conjugated Polymer Electrolyte for
High-Performance Polymer Solar Cells
(고성능 고분자 태양전지를 위한
공액형 고분자 전해질)



Advisor: Prof. Joo Hyun Kim

by

Sabrina Aufar Salma

A dissertation submitted in partial fulfillment of the requirements
for the degree of
Doctor of Philosophy

in Department of Polymer Engineering, The Graduate School,
Pukyong National University

February, 2023





Conjugated Polymer Electrolyte for High Performance Polymer Solar Cells

A dissertation

By

Sabrina Aufar Salma

Approved by:


(Chairman) Seong Il Yoo
(Member) Prof. Seyoung Kee
(Member) Prof. Hyun Sung Kim
(Member) Prof. Jaewon Chang
(Member) Prof. Joo Hyun Kim

February 17, 2023

Contents

CONJUGATED POLYMER ELECTROLYTE FOR HIGH PERFORMANCE POLYMER	
SOLAR CELLS	II
CHAPTER I	1
1. ORGANIC / POLYMERIC SOLAR CELLS	2
1). PHOTOGENERATION MECHANISM	4
(1) ABSORPTION OF PHOTONS.....	8
(2) REFLECTION	8
(3) EXCITON DIFFUSION.....	8
(4) CHARGE SEPARATION.....	9
(5) CHARGE TRANSPORT.....	9
(6) CHARGE COLLECTION	9
2). PHOTOACTIVE LAYER	10
3). ELECTRODE MATERIALS	15
4). INTERFACIAL LAYER	16
(1) ANODE BUFFER LAYER.....	16
(2) CATHODE BUFFER LAYER	17
5). PHOTOVOLTAIC CHARACTERIZATION	20
(1) POWER CONVERSION EFFICIENCY	20
(2) OPEN CIRCUIT VOLTAGE.....	25

(3) PHOTOCURRENT.....	26
CHAPTER II.....	29
INVESTIGATING THE EFFECT OF DIVERSE STRUCTURAL VARIATION OF CONJUGATED POLYMER ELECTROLYTES AS THE INTERLAYER ON PHOTOVOLTAIC PROPERTIES	30
2. RESULT AND DISCUSSION	36
1). OPTICAL AND ELECTROCHEMICAL PROPERTIES	36
2). THEORETICAL CALCULATION OF THE POLYMERS	43
3). OPTICAL SIMULATION CHARACTERISTIC OF CPEs USING TRANSFER MATRIX FORMALISM.....	47
4). INVESTIGATION OF CPE-COVERED ZnO SURFACE	50
5). PHOTOVOLTAIC PROPERTIES.....	55
6). ELECTRONIC IMPEDANCE SPECTROSCOPY (EIS) OF PSCs	71
3. CONCLUSION.....	73
CHAPTER III	74
EFFECT OF THE SIDE CHAIN FUNCTIONALITY OF THE CONJUGATED POLYELECTROLYTES AS A CATHODE INTERLAYER MATERIAL ON THE PHOTOVOLTAIC PERFORMANCES.....	75
1. INTRODUCTION	75

2. RESULT AND DISCUSSION	80
1.) OPTICAL AND ELECTROCHEMICAL PROPERTIES	80
2.) THEORETICAL CALCULATION OF THE POLYMERS	82
3.) INVESTIGATION OF THE ZnO SURFACE COVERED WITH CPEs	84
4.) PHOTOVOLTAIC PROPERTIES	88
3. CONCLUSION.....	96
REFERENCES.....	97
ACKNOWLEDGEMENT.....	126



List of Figures

- Figure 1. The photovoltaic process: absorption of photons (A), generation of carriers (G), collection of carriers (C)
- Figure 1. Conversion steps and loss mechanism of light
- Figure 2. Chemical structure of common organic
- Figure 3. Device structure of common organic solar cell
- Figure 4. Chemical structure of neutral, salt, and OH salt
- Figure 5. UV–Vis spectra of (a) PFN-T series, (b) PFN-BT series, and (c) PFN-TBT series films.
- Figure 6. DFT-optimized geometries and dipolar properties of (a) PFN-T (b) PFN-BT (c) PFN-TBT calculated by B3LYP/6-31G (d) level
- Figure 7. Cyclic voltammograms of CPEs
- Figure 8. Frontier molecular orbitals of two-repeating unit models with HOMO/LUMO energy levels calculated at the B3LYP/6-31G** level for (a) PFN-T, (b) PFN-BT, and (c) PFN-TBT.
- Figure 9. Optical electric field intensity of (a, b) pristine, (c, d) PFN-T, (e, f) PFN-BT, and (g, h) PFN-TBT by TMF optical
- Figure 10. Static water contact angle data of ZnO, ZnO/neutral polymers, ZnO/salt polymers, and ZnO/OH salt polymers
- Figure 11. Energy level diagrams of (a) ZnO/neutral, (b) ZnO/salt, and (c) ZnO/OH salt polymer categories.
- Figure 12. (a) Device architecture, J-V curves of PSCs based on (b) neutral, (c) salt, and (d) OH salt polymer

- Figure 13. IPCE graph of (a) neutral polymer category, (b) salt polymer category, (c) OH salt polymer category
- Figure 14. Correlation of (a) J_{sc} and R_s as function ΔWF (WF of ZnO with interlayer – WF of ZnO) work function as a function of J_{sc} and (b) R_{rec} and R_{sh} as a function of FF
- Figure 15. Photocurrent (J_{ph}) density vs. effective voltage (V_{eff}) of (a) neutral, (b) salt, and (c) OH salt polymer category.
- Figure 16. The dependence of J_{sc} on light intensity of (a) neutral, (b) salt, and (c) OH salt polymer category.
- Figure 17. The dependence of V_{oc} on the light intensity of (a) neutral polymer category, (b) salt polymer category, (c) OH salt polymer category
- Figure 18. Impedance spectra of (a) neutral, (b) salt, and (c) OH salt polymer category
- Figure 19. Chemical structure of the interlayer
- Figure 20. UV-Vis spectra of PFN, PFN salt, PFN-OH salt
- Figure 21. Cyclic voltammograms of PFN.
- Figure 22. DFT-optimized geometries and dipolar properties of PFN calculated by B3LYP/6-31G (d) level.
- Figure 23. Frontier molecular orbitals of two-repeating unit models with HOMO/LUMO energy levels calculated at the B3LYP/6-31G** level for PFN
- Figure 24. Static water contact angle data of ZnO, ZnO/PFN, ZnO/PFN-salt, and ZnO/PFN-OH salt.
- Figure 25. Energy level diagrams of ZnO/PFN, ZnO/PFN salt, and ZnO/PFN-OH salt.

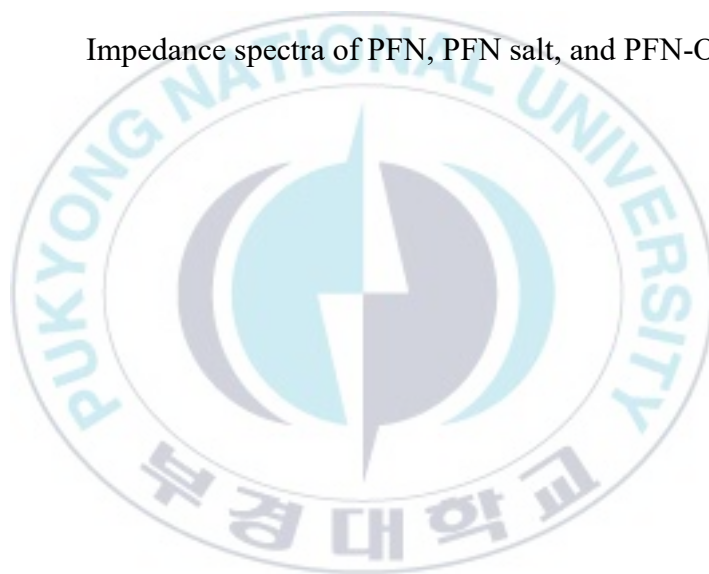
Figure 26. IPCE graph of (a) neutral polymer category, (b) salt polymer category, (c) OH salt polymer category.

Figure 27. (a) device architecture and (b). J-V curves of PFN, PFN salt, PFN-OH salt

Figure 28. Dependence of J_{sc} on light intensity of PFN, PFN salt, and PFN-OH

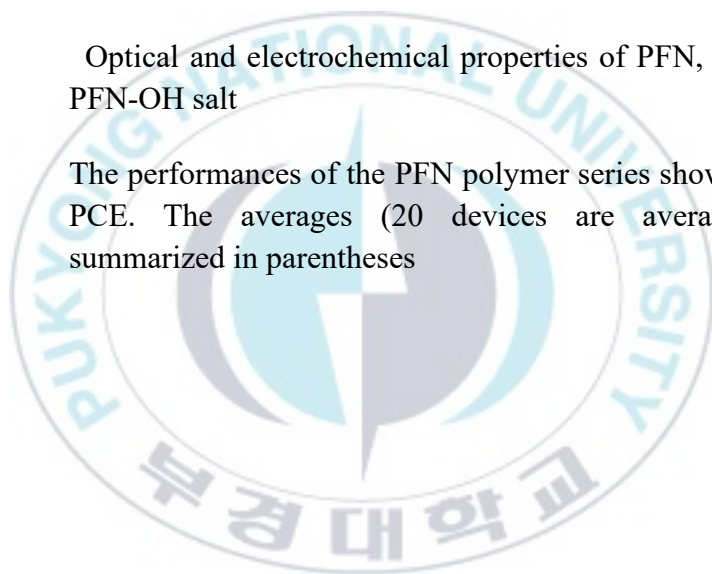
Figure 29. The dependence of V_{oc} on the light intensity of PFN, PFN salt, and PFN-OH salt

Figure 30. Impedance spectra of PFN, PFN salt, and PFN-OH salt



List of Tables

- Table 1. Cathode buffer layers work function, optimized thickness, and their deposition process
- Table 2. Optical and electrochemical properties of CPE.
- Table 3. The performances of the PSCs with CPEs with the best PCE. The averages (20 devices are averaged) are summarized in parentheses.
- Table 4. Optical and electrochemical properties of PFN, PFN salt, PFN-OH salt
- Table 5. The performances of the PFN polymer series show the best PCE. The averages (20 devices are averaged) are summarized in parentheses



Conjugated Polymer Electrolyte for High-Performance Polymer Solar Cells

Sabrina AUFAR SALMA

Department of Polymer Engineering, The Graduate School

Pukyong National University

Abstract

A series of conjugated polymer electrolytes (CPEs) based on dimethylamino propyl fluorene (FN), thiophene (T), benzothiadiazole (BT), and dithienyl benzothiadiazole (TBT) were synthesized by the Suzuki coupling reaction. Quaternarized polyelectrolytes were obtained from the post-polymerization treatment of the amino-terminal group. The incorporation of electron-rich (T), electron-deficient moieties (BT), and their combination (TBT) in the polymer backbone represent the different effects of polarity. Conjugated backbones are strengthened by varying their electron affinity and conjugated planarity. We systematically investigated the effect of applying CPEs with different backbones and functionalities in the side chain. Different backbones produce different molecular dipoles, and the side chain functionality induces an interfacial dipole. Inverted polymer solar cells (iPSCs) based on a bulk heterojunction (BHJ) were

fabricated with the ITO/ZnO/CPE/PTB7- Th:PC71BM/MoO₃/Ag structure. The device performance enhancement was achieved by inserting CPEs as the interlayer. Modifying the polymer backbone leads to improved efficiency and modifying the side chain functionality improves the performance compared with that of the interlayered neutral polymer.



I 고성능 고분자 태양전지를 위한 공액형 고분자전해질

사브리나 아우파 살마

부경대학교 대학원 고분자공학전공

요약

Dimethylamino propyl fluorene(FN)을 기반으로 하는 공액 고분자 전해질(CPEs)의 thiophene(T), benzothiadiazole(BT) 및 dithienyl benzothiadiazole(TBT)는 스즈키 커플링 반응에 의해서 합성되는 고분자 전해질이다. 쿼터너리 된 고분자전해질은 고분자를 합성한 이후에 아미노의 말단기 그룹을 변화시켰고 이 공액 주쇄는 전자 친화력 및 공액 평면화에 의해서 실질적으로 강화된다. 전자가 풍부한 thiophene (T)과 전자가 부족한 benzothiadiazole (BT), 그리고 두개의 조합인(TBT) 그룹들의 서로 다른 극성 효과의 성질을 이용하여 dimethylamino propyl fluorene (FN) 고분자의 주쇄에 각각 추가하였고 이를 통해 고분자 전해질(CPE)의 주쇄에서의 효과 및 측쇄의 말단기 변화를 통한 효과를 연구하였다. 서로 다른 주쇄들이 다른 분자들의 쌍극자를 유도하고, 측쇄의 기능기는 계면의 쌍극자를 유도한다. Bulk heterojunction (BHJ)를 기반으로 inverted polymer solar cells (iPSCs)의 소자를 ITO/ZnO/CPE/PTB7-Th:PC₇₁BM/MoO₃/Ag의 구조로 제작하였다. 소자의 성능은 중간층인 CPE를 추가 및 고분자 전해질의 주쇄를 변화시켰을 때

향상되었으며, 측쇄의 말단기가 변화함으로써 아미노 중성 고분자에 비해 높은 효율을 얻을 수 있게 되었다.



Chapter I

General Introduction

Research on renewable energies (such as solar energy and wind energy) is becoming essential for researchers as a result of the rise in electricity demand and the significant environmental risk posed by the use of fossil fuels to generate electricity. Solar photovoltaic cells are used in solar energy generation to transform solar energy into electricity. The efficiency of this device is improving by improving the materials used in manufacturing it.¹

Currently, the first two generations mostly serve the market. The first generation is made up of well-known medium- and low-cost technologies that produce average yields. Devices in the second generation (thin-film technology) have lesser efficiency but are less expensive to produce. The third generation uses pricey but very effective cells, a wide variety of designs, and innovative materials. Despite being the fourth generation, the assessment stated that performance and stability were still lacking.²

Solar energy is directly converted into electricity using photovoltaic solar cells, free from the intervention of a heat engine. In order to use new materials that are more effective at converting solar energy into electricity, research mostly focuses on the photovoltaic industry.³ The power conversion

efficiency Since the beginning of this decade, photovoltaic (PV) solar cell power conversion efficiency has increased from 1% to over 20%.⁴

1. Organic / Polymeric Solar Cells

Polymer solar cells are generally flexible solar cells due to the polymer substrate. Due to the complexity of modeling complicated junction geometries and the accompanying exciton dissociation processes, it is challenging to determine the maximum feasible power conversion efficiency from the ground up; however, an upper bound of 20% has been recorded.⁵

The organic solar cell is currently a fascinating alternative for harvesting sunlight. The optoelectronic characteristics of conventional semiconductors are combined with the good mechanical and processing characteristics of polymeric materials, such as plastic, in the semiconducting polymer. Using straightforward and less expensive deposition techniques like spin coating or blade coating, they can be treated from solution at room temperature onto a flexible substrate.⁶

Conjugated polymers have been used to create effective light-emitting diodes, field effect transistors, and photovoltaic diodes ever since their electroluminescence was discovered in them. When opposed to electrochemical cells, polymeric photovoltaic cells have several advantages, most notably the lack of a liquid electrolyte, which causes issues with

airtightness, as well as the potential for even more affordable production employing large area devices and flexible substrates. Small disposable solar cells for smart plastic cards that can show the remaining value, photodetectors in vast area scanners for medical imaging, and solar power applications for uneven surfaces are just a few examples of potential uses.⁷

The organic conjugated molecules or polymers are semiconductors that can self-assemble. The electrons are delocalized within the conjugated backbone of molecules where the p_z atomic orbitals overlap to produce conjugation molecular orbitals. Van der Waals interactions and aromatic $\pi - \pi$ interactions, which are significant in the solid state, are what cause inter-molecular contacts to develop.⁸

The bandgap of the materials is defined as the energy difference between the highest occupied molecular orbital (HOMO) and lowest unoccupied molecular orbital (LUMO) levels. By subtracting one electron from the HOMO level or adding electrons to the LUMO level, the organic semiconductor can be either p-doped or n-doped, respectively. The P-type is material with electron donor capability, easy to transport holes, and is referred to as the material with a high HOMO level. The n-type is a material with a low LUMO level that easily transports electrons and has electron acceptor capability.⁹

Charge carriers move easily in the conjugated backbone of polymers, but inter-molecular charge transport in organic materials is much more difficult. Hopping from one molecule to another limits macroscopic charge transport. As a result, organic materials have significantly lower charge mobility than inorganic materials such as silicon semiconductors. However, because organic chromophores have a high absorption coefficient, organic semiconductors can capture most of the photons within the absorption range using very thin layers while avoiding charge recombination.^{10,11}

Because of their low dielectric constant, the electron-hole pairs are tightly bound in the conjugated polymer. The exciton has a binding energy of 0.3-1 eV, while the binding energy of free electron-hole pairs in an inorganic semiconductor is comparable to thermal energy at room temperature. To effectively separate the tightly bound exciton, an organic hetero-junction composed of n-type and p-type materials with sufficient energy band offset is required. Because of this property of organic semiconductors, very different organic solar cell device architectures and processing techniques are used to achieve high power conversion efficiency (PCE).^{12,13}

1). Photogeneration Mechanism

The absorption of a photon results in the creation of an excited state, or the bound electron-hole pair (exciton), which is followed by exciton diffusion

to a region where exciton dissociation, or charge separation, takes place, and charge transport within the organic semiconductor to the appropriate electrodes.¹⁴

In polymer semiconductors, photoexcitation often leads to the generation of bound excitons with binding energy rather than free carriers, as was previously mentioned. These excitons need to be separated before the charges may be moved through the film and gathered at the electrodes. At the interface between electron-donor and electron-acceptor semiconductor materials, as well as the Schottky contact in single-layer devices, exciton dissociation can take place. More excitons can reach and detach from it if this contact region is greater.¹⁵

Typically, charge separation between the chains is necessary for the photogeneration of charged excitation. Photoexcitation with a polarized beam perpendicular to the polymer backbone is the most efficient method of generation. Exciton binding energy E_b conjugated polymers is valued at about 0.4 eV. The excitons are separated from the conduction band (CB) and the valence band (VB) by less than or equal to 0.2 eV since the binding energy is not greater than roughly 0.4 eV. But for the exciton to disintegrate at normal temperature, there still needs to be a clear offset between the materials.¹⁶ The description of different types of exciton were described as follows :

- Frenkel exciton: Only one chemical unit can contain the electron-hole pair.
- Mott-Wannier exciton: Compared to the gap between unit cells, the distance between an electron and a hole is substantially higher. According to calculations made with a lower effective mass, their energy levels can be compared to the bound state of hydrogen.
- Charge transfer exciton: Only a few nearby molecular units are covered by the exciton.
- Inter-chain excitons: To denote that the constituent charges are situated along the same polymer chain, the phrase is used to describe polymeric semiconductors. According to current thinking, the primary species that forms in conjugated polymers after photoexcitation is intra-chain excitons.¹⁷

The production of electric energy from sunlight is the result of a chain process (Figure 1). Sunlight photons are absorbed inside the device (A), carriers are then generated from exciton dissociation (G), and carriers are collected by the electrodes and driven into the external circuit (C). These are the productive events of the PV process. A more detailed analysis permits us to understand and eventually improve the different steps of the PV effect (Figure 2).¹⁴

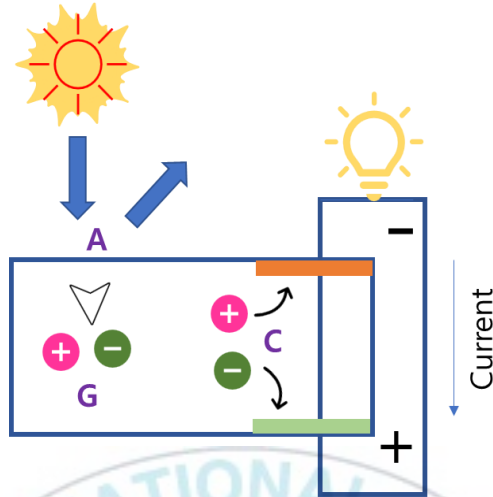


Figure 31. The photovoltaic process: absorption of photons (A), generation of carriers (G), collection of carriers (C)

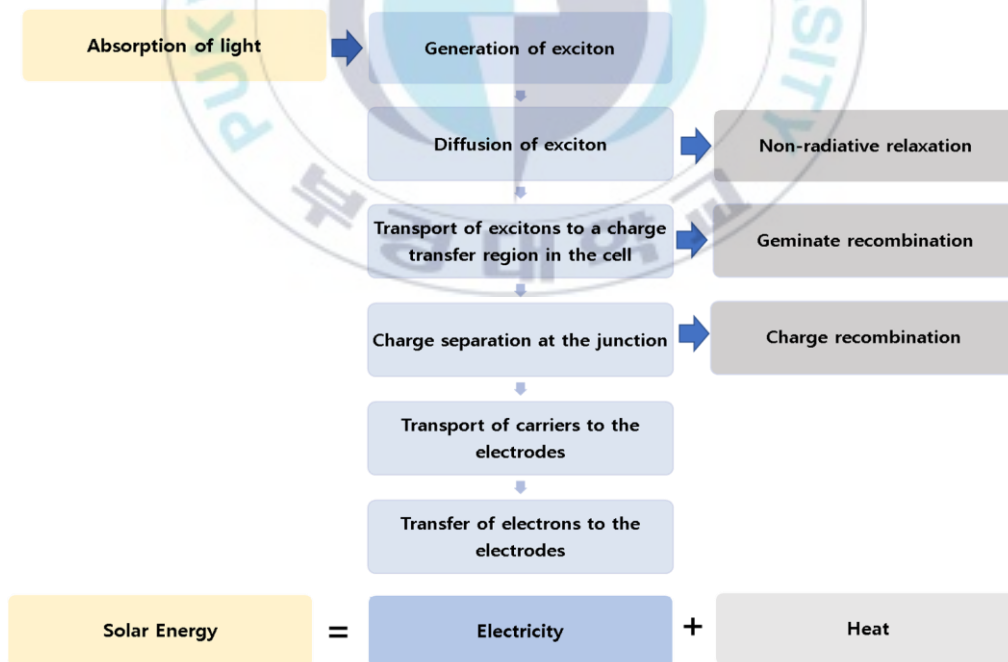


Figure 32. Conversion steps and loss mechanism of light

(1) Absorption of photons

In most organic devices only a small portion of the incident light is absorbed because the bandgap is too high. A bandgap of 1.1 eV (1100 nm) is required to absorb 77% of the solar radiation on earth whereas the majority of semiconducting polymers have bandgaps higher than 2.0 eV (600 nm), limiting the possible absorption to about 30%. The organic layer is too thin. Low charge carriers and exciton mobilities require layer thickness in the order of 100 nm. Fortunately, the absorption coefficient of organic materials is generally much higher than in silicon only about 100 nm are necessary to absorb between 60 and 90% if a reflective back contact is used.^{14,18}

(2) Reflection

Reflection losses are probably significant, but little investigated in these materials. Systematic measurements of photovoltaic materials are desired to provide knowledge of their impact on absorption losses. Anti-reflection coatings as used in inorganic devices may then prove useful once other losses such as re- combination become less dominant.^{14,18}

(3) Exciton diffusion

Ideally, all photoexcited excitons should reach a dissociation site. Since such a site may be at the other end of the semiconductor, their diffusion length should be at least equal to the layer thickness (for sufficient absorption),

otherwise, they recombine, and photons are wasted. Exciton diffusion ranges in polymers and pigments are usually around 10 nm.^{14,18}

(4) Charge separation

Charge separation is known to occur at organic semiconductor/metal interfaces, at impurities such as oxygen, or between materials with sufficiently different electron affinities (EA) and ionization potentials (IA). In the latter, one material can then act as an electron acceptor (A) while the other keeps the positive charge and is referred to as an electron donor (D). If the difference in IA and EA is not sufficient, the exciton may just hop onto the material with the lower bandgap without splitting up its charges. Eventually, it will recombine without contributing charges to the photocurrent.^{14,18}

(5) Charge transport

The transport of charges is affected by recombination during the journey to the electrodes, particularly if the same material serves as a transport medium for both electrons and holes. Also, interaction with atoms or other charges may slow down the travel speed and thereby limit the current.^{14,18}

(6) Charge collection

To enter an electrode material with a relatively low work function (Al or Ca) the charges often have to overcome the potential barrier of a thin oxide

layer. In addition, the metal may have formed a blocking contact with the semiconductor so that it cannot immediately reach the metal.^{14,18}

2). Photoactive Layer

Polymers used in OPV are characterized by being conjugated: the conjugation of a polymer refers to the presence of a backbone chain of alternating double and single bonds. The sp^2 hybridized carbon centers have a valence electron in the P_z orbital (π) which is orthogonal to the other σ bonds. The overlapping of π/π bonds determines the creation of delocalized energy states within the structure, which promotes intermolecular transport and allows for the transport of charge.

The active layer used in polymer solar cells consists of a donor-acceptor blend, where a conjugated polymer acts as a donor, and generally a fullerene derivative acts as an acceptor. The most common materials used in this work for the active layer are Poly (3-hexylthiophene) (P3HT) PTB7Th, and Phenyl-C61-butyric acid methyl ester (PCBM), whose chemical composition is reported in Figure 3. Advanced polymers can be synthesized to improve the PCE of a solar cell, for example, it is possible to combine two units in the structure, one that acts as an acceptor and one that acts as a donor, by forming a donor-acceptor (D-A) copolymer. In these polymers, the HOMO and LUMO mostly depend on the HOMO of the donor and the LUMO of the

acceptor, respectively. This helps optimize the efficiency by engineering both the EGAP and the LUMO alignment with the fullerene, by choosing the appropriate donor-acceptor unit. Moreover, to help the extraction of charge in OSC by reducing charge recombination and improving exciton dissociation, two additional functional layers are used: a Hole Transport Layer (HTL) which is characterized by good hole mobility that tends to act as an electron blocker, and an Electron Transport Layer (ETL) which conversely has good electron mobility and tends to act as a hole blocker. The HTL used in this thesis is Poly (3,4- ethylene dioxythiophene) polystyrene sulfonate (PEDOT: PSS) (Figure 3), while the ETL is zinc oxide (ZnO).

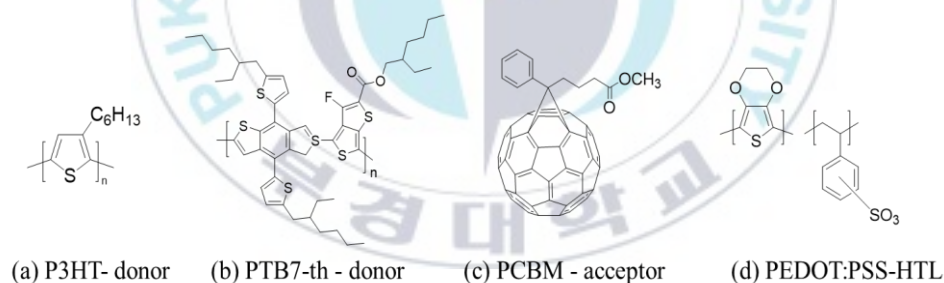


Figure 33. Chemical structure of common organic

Two possible architectures of a bulk heterojunction (BHJ) solar cell are shown in Figure 4. The first type of polymer solar cells employed Indium Tin Oxide (ITO) as a transparent anode. In such a structure, the back electrode is the cathode which has a low work function and can easily oxidize due to its

direct air exposure. This configuration is called the normal structure and it is still largely used, see Figure 4 (a).

In another structure, the cathode and anode are flipped in the positions, resulting in the placement of the high-work function anode at the back of the cell. This approach was developed to be able to utilize high-work function electrodes, such as silver, as the back electrode. The latter can be printed from a liquid paste and therefore, the such architecture enables the possibility of scalable processing of devices using roll-to-roll machinery.¹⁹

It was later shown that silver was more resistant to humid environments compared to aluminum and therefore could significantly improve the device stability under certain test conditions.²⁰ Such a structure is called an inverted structure Figure 4(b).

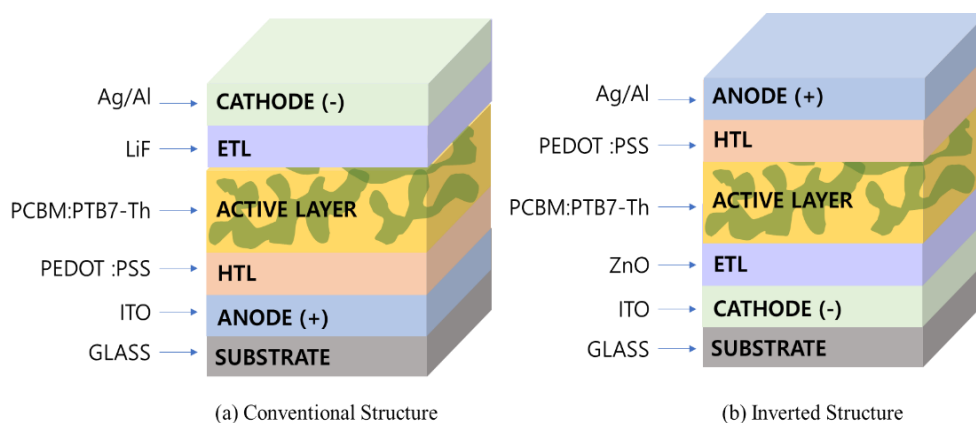


Figure 34. Device structure of common organic solar cell

In polymer solar cells, the thin film morphology of the BHJ active layer plays a critical role in determining the performance of the device. Due to the relatively low dielectric constant of the BHJ composite, large exciton-binding energy gives rise to strongly localized electron-hole pairs in BHJ active layers, which requires the additional driving force to separate the pair of electrons and holes. The energy level offsets between D and A provide an additional electric field with different electrochemical potentials at the molecular interface to separate the excitons into weakly bounded Coulombic pairs, and thereafter separate into free charge carriers.^{21,22} To enlarge the D/A interface, the BHJ concept was further introduced to simultaneously enlarge the charge dissociation.^{7,23,24}

Therefore, the manipulation of the film morphology of the BHJ active layer has always been the focus in the field of organic photovoltaic (OPVs).²⁵ For OPVs, almost all the organic active layers are processed from solution, and the difference in surface energy of D and A will lead to an inhomogeneous vertical distribution (or concentration gradient) and phase separation throughout the BHJ active layer, causing “vertical phase separation”, which is crucial to the charge transport and device efficiency.²⁶ The model of the vertical composition profile of the P3HT:PC₆₁BM system using variable-angle spectroscopic ellipsometry was reported by Clamoxyquine’s *et al.* A concentration gradient varying from PC₆₁BM-rich

domains near the PEDOT: PSS side to P3HT-rich domains adjacent to the free (air) surface was reported in the conventional OPVs, where such a composition profile was inefficient for corresponding charge transport and collection. Alternatively, inverted OPVs with reversed charge transport directions showed an advantage over conventional OPVs because of the vertical phase separation. In inverted OPVs, the surface energy difference induces a D-rich phase close to the anode on the top and the A-rich phase close to the cathode beneath, thus shortening charge transport pathways and reducing charge recombination at the electrodes.

Several strategies have been pursued to extend the absorption range of donor polymers for organic solar cells. These include strategies aimed at extending the conjugation length of the π -conjugated segments, for example, by replacing phenyl rings with thiophene rings that help to planarize the polymer backbone through a reduced steric effect or by planarizing neighboring monomers by using a bridging atom. Planarization may reduce the optical gap further by enabling π -stacked aggregates to form an alternative approach to vary the heteroatoms in the conjugated backbone: replacing the sulfur atom in polythiophene with selenium leads to a lowered LUMO energy but unchanged HOMO, due to the influence of the heteroatom on the LUMO in this molecule. A third route, which is now widely used, is to combine electron-rich (e.g., thiophene-containing) and electron-poor (e.g.,

benzothiadiazole [BT]) units in the polymer backbone in a so-called 'push-pull' structure. Here, the HOMO of the copolymer is dominated by the HOMO of the electron-deficient unit and the LUMO by that of the electron-rich unit. The strategy is widely adopted, due to the large range of 'push' and 'pull' units that can be used and the ability to control copolymer HOMO and LUMO energies independently. Notable advances in OPV efficiency were made using push-pull copolymers based on thiophene - BT structures carbazole - BT structures, and dithienobenzene - modified BT structures and diketopyrrolopyrrole - thiophene structures.²⁷

3). Electrode Materials

The development of new photoactive materials has been accompanied by growing research into new electrode and interlayer materials. This has been motivated partly by the need to find electrodes of higher or lower work function to achieve Ohmic contacts with new photoactive materials of higher-lying LUMO or lower-lying HOMO energy, but also by the search for transparent conductive layers of lower cost and embedded energy than the widely used indium tin oxide, and by the search for more stable substitutes for reactive cathode metals. Alternative electrode interlayers studied in OPV include high-work function oxides such as NiO²⁸, WO₃, MoO₃²⁹, stable low-work function oxides such as TiO₂, ZnO^{30,31}, polymer interlayers³², and organic conducting layers such as high conductivity PEDOT³³ vapor phase

polymerized PEDOT61, carbon nanotube³⁴, and metal nanowire-based layers. Solution processable oxide layers and conducting polymer layers are preferred for large-scale processing.²⁷

4). Interfacial Layer

(1) Anode Buffer Layer

The primary task of the anode is the extraction of photo-generated holes from the active layer. In general, transparent conductive oxide substrates such as indium tin oxide (ITO), fluorine-doped tin oxide (FTO), aluminum-doped zinc oxide (AZO), etc. coated glasses are used as anode (in conventional). An ITO has a favorable work function (≈ 4.7 eV) concerning the typical energy levels of the active layer materials; hence it can collect both positive and negative charge carriers. Therefore, ITO cannot provide the required selectivity. In addition, polycrystalline ITO thin films induce a significant surface roughness at the nanometer scale.^{35,36}

This surface roughness is regarded as a major cause of leakage current in the resultant devices.³⁷ Also, ITO electrodes were reported to interact chemically with the organic material, and that contributes toward the degradation of OSCs device performances^{36,38,39} By considering all these factors, an ABL coating is needed, and it should fulfill the following requirements: 1) Establish ohmic contact with the donor material; 2) transport

positive charge carriers efficiently (hole transporting); 3) block negative carriers (electron blocking); 4) smoothen the ITO surface to reduce surface recombination; 5) should be stable and transparent.⁴⁰

The PEDOT: PSS is the most commonly used ABL and is a p-type semiconductor with the work function of 5.2 eV. It allows a favorable band alignment with the HOMO level of the donor molecules. Furthermore, it also forms a smooth film and improves the contact between the polymer and the ITO, thereby preventing any short-circuit probability due to ITO surface roughness. Unfortunately, the acidic nature of PEDOT:PSS and its UV-prone degradation have restricted its further use.⁴¹ Moreover, the processing method of PEDOT: PSS leads to water insertion in the active layer, as it is coated from a water-based solution.⁴² Even after baking, water traces persist on the surface owing to its hygroscopic nature, hence it can be a potential threat to the device's lifetime. This has led to the emergence of alternative ABLs including small organic molecules, polymers, metals, and inorganic metal oxides.⁴³

(2) Cathode Buffer Layer

The primary role of a CBL is to facilitate the collection of electrons at the electrode. For smooth device functioning, CBL also performs several other crucial tasks, such as 1) forming an electron selective and transport

interlayer, 2) forming an ohmic contact with the acceptor molecule, 3) transporting negative charge carriers efficiently (electron-transporting), 4) blocking the reverse charge carriers, 5) protecting the active layer in conventional device structure from the hot metal atoms during thermal deposition of the cathode; For efficient OSCs, the selection of an appropriate CBL to optimize the electron collection and transport is highly important. An ideal CBL should be good at electron extraction and transport. It must have a suitable energy level that facilitates electron transport, with high transparency, good compactness, and high stability. Several commonly used CBLs were first established for organic light-emitting diodes (OLEDs) and then transferred to OSCs fabrication. In the past few years, several materials have been explored as CBL in conventional and inverted type OSCs and which are summarized in Table 1.

Table 6. Cathode buffer layers work function, optimized thickness, and their deposition process

Cathode Buffer Layer	Work Function(eV)	Optimized Thickness (nm)	Deposition Process	Conventional /Inverted
Barium (Ba)	2.7	20	Thermal evaporation	Conventional
Calcium (Ca)	2.9	20	Thermal evaporation	Both
Cesium carbonate (Cs ₂ CO ₃)	1.9	1	Thermal evaporation	Both
Aluminum oxide (Al ₂ O ₃)	3.89-4.02	2	Thermal evaporation	Inverted
Zinc oxide (ZnO)	4.3-4.5	30-60	Spin coating	Both
Titanium dioxide (TiO ₂)	4.5-4.6	10-20	Spin coating	Both

Zinc Oxide (ZnO): In recent years, CBLs comprising of pristine ZnO, doped-ZnO, and ZnO-based composites, as well as the surface-modified ZnO-based layers have been used by several research groups for enhancing the device parameters of inverted architecture OSCs. The ZnO is one of the potential choices as CBL in inverted OSCs owing to its enhanced electron mobility, high transparency, easy synthesis, and high stability. Takahashi et al.⁴⁴ used the electrodeposition method to insert the ZnO into the OSCs, and they observed remarkable performance enhancement. The standard device ITO/CBL/PV/MEH-PPV/PEDOT:PSS/Au, (where PV: bisbenzimidazole [2,1-a:2',1'-a'] anthracene [2,1,9-def:6,5,10-d'e'f'] diisoquinoline-6,11-dione), had PCE of 1.24% than control device (0.21%). The low-thickness ZnO-based CBL devices suffer from low mechanical robustness and devices go under degradation due to chemical or physical reactions between the active layer and the electrode.

To overcome this issue, researchers have come up with solutions such as doping new materials into ZnO. The doping not only improves its optical and electrical properties simultaneously, but also helps in resolving the thickness-related issue of ZnO CBL, and improvement in its conductivity. There are several reports in which researchers have used doped ZnO as CBL, and they have achieved improvement in device parameters of i-OSCs.⁴⁵ Commonly used dopants are I, II, and III group elements. Besides these, transition metal

ions and rare-earth elements are also doped in ZnO to improve its optical properties, thereby contributing to PCE enhancement

5). Photovoltaic Characterization

(1) Power Conversion Efficiency

The photoexcited electron can decrease its potential energy by losing energy to phonons until it reaches the lowest lying level in the CB - the LUMO. Since the phonon energy dissipates into heat this process is known as thermalization. As a consequence of thermalization, the semiconductor bandgap is often regarded as a measure of the achievable voltage. The higher the bandgap the higher the voltage can be. On the other hand, a low bandgap material can absorb more photons and thus increase the number of photogenerated charge carriers i.e., the photocurrent. The lower the bandgap, the higher the photocurrent. Hence, there must be an optimal bandgap for a given illumination spectrum. Shockley and Queasier were the first who calculated the maximum power conversion efficiency for a semiconductor with a given bandgap assuming only radiative recombination and the solar radiation o earth. They obtained a value of 30% for a semiconductor with a bandgap of 1.12eV like Si.

Thus, considering the voltage dependence of the $J - V$ curve the maximum power is the maximum product of J and V that can be found amongst the data points in the fourth quadrant. This maximum area is larger the more the $J - V$ curve resembles a rectangle with the area $V_{oc} \times J_{sc}$. The ratio between these two areas represents a measure of the quality of the shape of the JV characteristics:

thus:

$$FF \equiv \frac{(JV)_{\max}}{V_{oc} J_{sc}} \quad (\text{eq.1})$$

$$P_{\max} = (JV)_{\max} = V_{oc} \cdot J_{sc} \cdot FF \quad (\text{eq.2})$$

The higher FF the more the JV characteristics resemble a constant current source with a maximum voltage and the higher the electric power that can be extracted. The voltage/current ($V_p \cdot I_p$) combination that gives the largest power rectangle is called the maximum power point. Thus, any appliance connected to a solar cell can utilize the maximum output power only if its supply voltage is around V_p or in other words: The load resistor $R = V_p / I_p$. Otherwise, power would be wasted in heating the series resistor ($V < V_p$) or via increased current losses through the ideal diode and shunt resistor ($V > V_p$).

To describe the power conversion efficiency η of a solar cell the maximum output power P_{max} has to be related to the power of the incident light (P_{light}). Using Eq. (2) to express P_{max} considering the wavelength dependence of the parameters involved we can write:

$$\eta(\lambda) \equiv \frac{I_{sc}(\lambda) \cdot V_{oc}(\lambda) \cdot FF(\lambda)}{P_{light}} \quad (\text{eq.3})$$

Because of the wavelength and intensity, dependence power conversion efficiencies are only meaningful for a given spectral distribution and intensity. This can be the solar spectrum or the spectrum of artificial illumination for indoor applications.

Equivalent circuit diagrams (ECDs) are frequently used to describe the electric behavior of more complex semiconductor devices with a network of ideal electrical components such as diodes, current or voltage sources, and resistors. Although the specific physical processes in organic semiconductors may be different and therefore lead to other parameters, the principal loss mechanisms are the same and we may therefore apply the same circuit. We suggest associating the processes with the single components in the ECD:

- The current source generates current upon illumination. $I_L =$ a number of dissociated excitons /s = number of free electron/hole pairs

immediately after generation - before any recombination can take place.

- The shunt resistor R_{sh} , is due to the recombination of charge carriers near the dissociation site (e.g D/A interface). Provided the series resistor R_s is at least one order of magnitude lower than R_{sh} , it may also include recombination further away from the dissociation site e.g., near the electrode. Otherwise, an extra shunt resistor R_{sh2} has to be considered. R_{sh} can be derived by taking the inverse slope around 0V:

$$R_{sh} \approx \left(\frac{I}{V}\right)^{-1}$$

(eq.4)

This is because at very small voltages the diode D is not conducting and the current driven by the external voltage (positive or negative) is only determined by $R_{sh} + R_s$ with R_{sh} (typically) being much larger.

- The series resistor R_s considers conductivity i.e., mobility of the specific charge carrier in the respective transport medium. For example, mobility of holes in a p-type conductor or electron donor material. The mobility can be affected by space charges and traps or

other barriers (hopping). R_s is also increased with a longer traveling distance of the charges in e.g., thicker transport layers. R_s can be estimated from the (inverse) slope at a positive voltage $> V_{OC}$ where the IV curves become linear:

$$R_{sh} \approx \left(\frac{I}{V}\right)^{-1}$$

(eq.5)

This is because at high positive external voltages V the diode D becomes much more conducting than R_{sh} so that R_s can dominate the shape of the IV curve.

- Solar cell voltage V . The cell can generate a voltage between 0 and V_{OC} depending on the size of the load resistor. To obtain IV curve data in other voltage ranges ($V < 0$ and $V_{OC} < V$) in the IV curve an external voltage source is required. We note that also the voltage drops across a load resistor in the range between 0 and V_{OC} can be simulated by the same voltage source so that the entire range can be scanned by applying an external voltage.

Note that the current for $V > V_{OC}$ and the extra current for $V < 0V$ is delivered from the external voltage source. The external voltage source can then act as a current amplifier to boost the photosensitivity,

but the actual photon-to-current conversion efficiency (EQE) of the solar cell or photodiode cannot be increased.

(2) Open Circuit Voltage

First, we consider the case of an ideal solar cell that comprises only the ideal diode D in the dark so that $R_s = 0$ and $R_{sh} = \infty$

$$I_d = I_0 \left(e^{\frac{qV}{nkT}} - 1 \right) \quad (\text{eq.6})$$

$$I_d = I_0 \left(e^{\frac{qV}{nkT}} - 1 \right) - I_L \quad (\text{eq.7})$$

$$V_{oc} = \frac{nkT}{q} \ln \left(\frac{I_L}{I_0} + 1 \right) \quad (\text{eq.8})$$

$$V_{oc} = \frac{nkT}{q} \ln \left(\frac{I_L - V_{oc}/R_{sh}}{I_0} + 1 \right) \quad (\text{eq.9})$$

This equation relates the maximum output voltage not only to the light-generated current I_L but also to the reverse saturation current and the shunt resistor. Now, also the formula for V_{oc} becomes transcendent and requires

numerical modeling to find a solution. The value of V_{OC} still depends on the ratio I_L/I_0 but now I_L is decreased by the presence of a finite R_{sh} whereas R_s is unimportant since there is no current flowing through it that can create a voltage drop (loss).

(3) Photocurrent

The short circuit current is simply the light current I_L (photogenerated charge carriers/s i.e., number of split excitons/s) reduced by the current through the shunt I_{sh} and the diode D , I_d :

$$I_{sc} = I_L - I_{sh} - I_d \quad (\text{eq.10})$$

This is the highest current that can be extracted from a solar cell. The light current increases linearly with the illumination intensity. To extract a quantity that describes how efficiently photons are converted into charges in the external circuit, I_{sc} has to be related to light intensity. This leads to the definition of the spectral response:

$$SR(\lambda) = \frac{J_L(\lambda)}{\phi(\lambda)} \quad (\text{eq.11})$$

with ϕ being the light intensity per illuminated area (W/m^2) and J_{sc} representing the current density (A/m^2) in short circuit mode. The spectral response (SR) thus gives the current in the external circuit per watt incident light (A/W). This quantity is frequently used to characterize the light sensitivity of photodiodes since the product $SR \cdot J_{sc}$ gives immediate light intensity. For the characterization of solar cells, a quantity that considers the actual fraction of the incident photons that can be converted into electrons in an external circuit is of higher interest:

$$EQE = \frac{\text{number of electron in external circuit}}{\text{number of incident photon}} \quad (\text{eq.12})$$

EQE stands for external quantum efficiency and represents, together with the power conversion efficiency η , the most interesting parameter of a solar cell. The EQE can be derived from the spectral response considering that the energy of a photon $E_p = hc/\lambda$ with h being Planck's constant, c the speed of light, and q the elementary charge using the following formula

$$EQE(\lambda) = SR(\lambda) \frac{hc}{q\lambda} \quad (\text{eq.13})$$

Note that the EQE gives higher values for shorter wavelengths when compared with the SR spectrum. This is because the spectral response relates to the energy of photons whereas the EQE refers only to the number of particles. Since the output current is determined by the number of electrons that can be “pumped” into the CB regardless of their energy, the EQE represents a true measure of the photon-to-current conversion efficiency in contrast to SR. The EQE can be converted into the internal quantum efficiency IQE if only the fraction of the absorbed photons is considered:

$$IQE(\lambda) = \frac{EQE(\lambda)}{1 - R(\lambda) - T(\lambda)} \quad (\text{eq.14})$$

with $R(\lambda)$ denoting the fraction of reflected light and $T(\lambda)$ the fraction of the transmitted light. The IQE is very helpful and frequently used in inorganic devices to investigate the physical processes in the semiconductor material. In contrast to inorganic solar cells where the complete bulk absorbs light and contributes to the photocurrent, organic devices have typically large regions that act only as an optical filter. In addition, interference effects would have to be considered because of the very thin films compared to inorganic cells.

Chapter II

Investigating The Effect of Diverse Structural Variation of Conjugated Polymer Electrolytes as The Interlayer on Photovoltaic Properties



Reproduces with permission from

[Chemical Engineering Journal 420 (2021) 129895]

Copyright © 2021 Elsevier B.V

Investigating The Effect of Diverse Structural Variation of Conjugated Polymer Electrolytes as The Interlayer on Photovoltaic Properties

1. Introduction

Polymer solar cells (PSCs) are a promising alternative source of clean and renewable energy. In recent decades, PSCs have been under immense focus owing to their mechanical flexibility, low weight, low-cost energy sources, large-scale fabrication, and roll-to-roll printing.^{46–49} PSCs based on the combination of an electron donor and electron acceptor with a bulk heterojunction (BHJ) are advantageous as an emerging photovoltaic technology over the conventional device structure.

The idea of BHJ was introduced by Yu et. al.⁵⁰ wherein blending donor (D) and acceptor (A) materials were very close to each other, typically less than 10 nm apart. Such distances are within the exciton pair mean free-path lengths (the minimum diffusion distance before the exciton can be annihilated via recombination).^{51,52} An interpenetrating network with a large donor-acceptor interfacial area can be achieved by controlling the phase. Therefore, present PSCs studies are focused on enhancing the device PCE. Selectively or simultaneously enhancing the short-circuit current (J_{SC}), open-circuit voltage (V_{OC}), and fill factor (FF) is critical to increasing PCEs. The

J_{SC} determined by the bandgap, thickness, morphology, and breadth of the absorption band of the active layer materials. Because those parameters influence the charge transport to the electrodes.⁵³ Additionally, V_{OC} can be increased either by tuning the lowest unoccupied molecular orbital (LUMO) or the highest occupied molecular orbital (HOMO) energy levels of the acceptors or polymer donors, respectively.⁵⁴ FF can be increased by improving the active layer morphologies for balanced charge transport.^{55–58} In addition to the synthesis of photoactive materials, interlayer modification is essential for solving the intrinsic limitations of mismatched energy levels, unbalanced carrier mobility, and improved device efficiency and stability in OSCs.^{12,13}

Interfacial engineering is a fundamental approach to increasing PCEs. The anode/cathode buffer layers are inserted between the active layer and electrodes.⁵⁹ These buffers can alleviate the interfacial energy barriers and facilitate charge transporting/collection capability when holes are collected at the anode and electrons are extracted at the cathode.⁶⁰ Appropriate materials could efficiently hamper charge recombination and lower contact resistance at the active layer/electrode interface leading to enhanced hole/electron extraction. As a result, J_{SC} , V_{OC} , and FF , in a single device, can be selectively or simultaneously enhanced.⁶¹

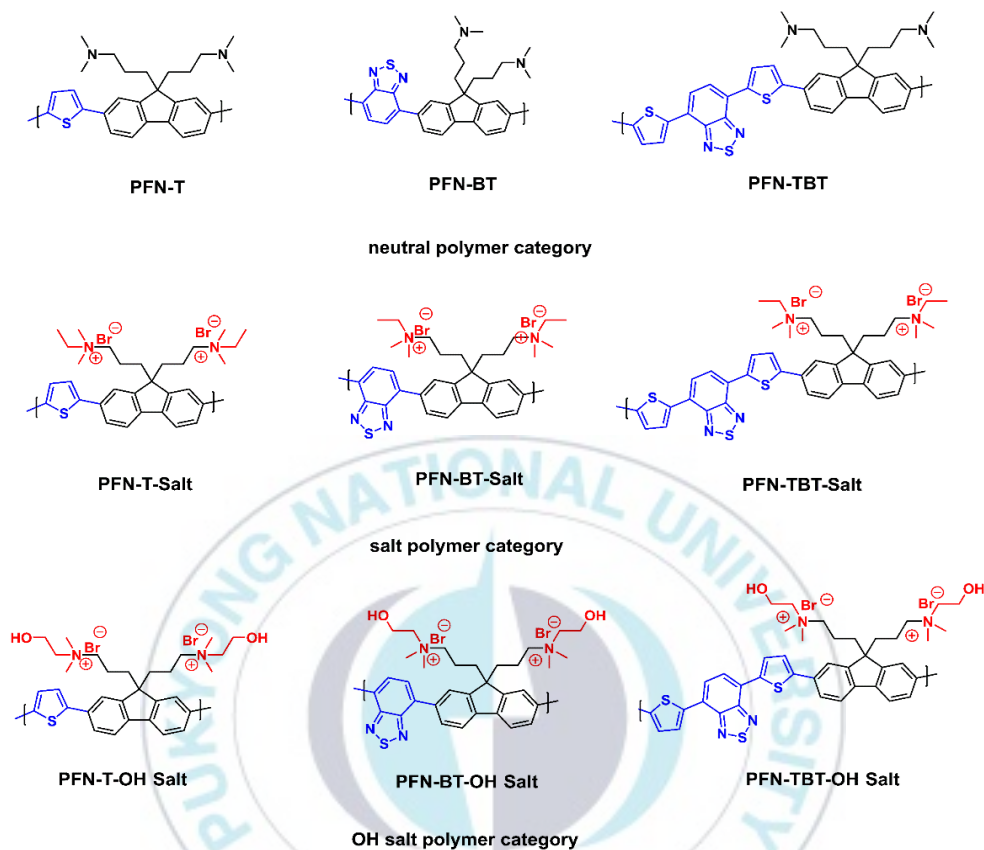


Figure 35. Chemical structure of neutral, salt, and OH salt

Among many material types, conjugated polymer electrolytes (CPEs) used as interlayer materials in PSCs have been reported to improve the PCE. CPEs consist of a conjugated polymer backbone and a polar ionic side group. The alcohol-soluble CPEs are efficient interfacial materials owing to their unique properties including intimate contact with the hydrophobic organic active layer and hydrophilic electrode alcohol-soluble fabrication without intermixing with the halogenated solvent-processed active layer.^{62,63} The alcohol-soluble CPE forms an interfacial dipole at the cathode interface and

improves the built-in electrical field.^{64,65} Therefore, many high-performance fluorene-based CPEs, such as the widely used PFN (poly[(9,9-bis(3-(N,N-dimethylamino)propyl)-2,7-fluorene)-alt-2,7-(9,9-dioctyl fluorene)]) contain hydrophilic amino groups and hydrophobic aliphatic side chains.^{66–68}

In this study, we designed and synthesized diverse CPEs to investigate the effect of their backbone and side chain structures, based on dimethylaminopropyl fluorene (FN) interlayer, on photovoltaic properties. Figure 5 shows a series of CPEs with different side chains divided into three categories.

The first category is FN polymers as a neutral precursor (neutral polymer category) with FN backbone with thiophene named PFN-T (poly[(9,9-bis(3'-(N,N-dimethylamino)propyl)-2,7-fluorene)-alt-4,7 (thiophene)]), FN backbone with a benzothiadiazole named PFN-BT (poly[(9,9-bis(3'-(N,N-dimethylamino)propyl)-2,7-fluorene)-alt-4,7-(2,1,3-benzothiadiazole)]), and FN backbone with a dithienyl-benzothiadiazole unit named PFN-TBT (poly- [(9,9-bis(3'-(N,N-dimethylamino)propyl)-2,7-fluorene)-alt-4,7-(dithienyl)-2,1,3(benzothiadiazole)]).

The second category is quaternized FN polymer derivatives (salt polymer category) with a tetraalkylammonium salt named PFN-T salt (poly[(9,9-bis(3'-(N-ethyl-N, N-dimethylamino)propyl)dibromide-2,7-

fluorene)-alt-4,7 (thiophene)]), PFN-BT salt (poly[(9,9-bis(3'-(N-ethyl-N,N-dimethylamino)propyl)dibromo-2,7-fluorene)-alt-4,7-(2,1,3 benzothiadiazole)]), and PFN-TBT salt (poly-[(9,9-bis(3'-(N-ethyl, N, N-dimethylamino) propyl) dibromide-2,7-fluorene)-alt-4,7-(dithienyl)-2,1,3(benzothia-diazole)]).

The last category is quaternized neutral polymer with ethyl hydroxy trialkyl ammonium salt (OH salt polymer category) named PFN-T-OH salt (poly[(9,9-bis(3'-(N-hydroxyethyl-N,N-dimethyl amino) propyl)dibromide-2,7-fluorene)-alt-4,7-(thiophene)]), PFN-BT-OH salt (poly[(9,9-bis(3'-(N-hydroxyethyl-N,N-dimethylamino) propyl)dibromo-2,7-fluorene)-alt-4,7-(2,1,3 benzothiadiazole)]), and PFN-TBT-OH salt (poly- [(9,9-bis(3'-(N-hydroxyethyl, N,N-dimethylamino) propyl)dibromide-2,7-fluorene)-alt-4,7-(dithienyl)-2,1,3 (benzothiadiazole)]).

The first category with PFN-T, PFN-BT, and PFN-TBT, contains hydrophilic amino and hydrophobic parts in the backbone. A small amount of acetic acid should be added to the polymer to improve its solubility in MeOH leading to orthogonal solubility with the active layer. However, this may deteriorate the ZnO layer because of its acidic nature.⁶⁹

Modifying the hydrophilic amino part to increase solubility in MeOH by quaternization is required to overcome the ZnO layer deterioration. Two kinds

of quaternized agents were used: bromoethane and bromoethanol. In previous studies, organic electrolytes with hydroxyl groups were prepared and deposited as interlayers for inverted PSCs.^{70,71}

Inspired by its excellent interface characteristics, we focused on interface dipole modification by introducing a hydroxyl group and quaternary ammonium bromide salt. The presence of a quaternary ammonium salt, which contains CPE, leads to a high J_{SC} in solar cells. The synergistic effect of the interlayer allows its embedding in the ZnO layer. This is due to the formation of a favorable interface dipole between the ZnO and quaternary ammonium salt layer. The electron collection ability from the active to the electron transport layer is improved by reducing the interface energy barrier.⁷²⁻⁷⁴

Upon using the neutral polymer and polymer salt as the interlayer in the inverted device structure (ITO/ZnO/interlayer/PTB7-Th:PC₇₁BM/MoO₃/Ag), we found that CPEs with OH salt category offered the highest PCEs as compared to neutral polymer PCEs. For the neutral polymer, the PCEs of the PSCs were 8.80%, 9.94%, and 9.43% for PFN-T, PFN-BT, and PFN-TBT, respectively.

PCEs of the PSCs in the polymer salt category were 9.43%, 9.87%, and 9.74% for PFN-T salt, PFN-BT salt, and PFN-TBT salt, respectively. Finally, for the polymer hydroxy salt, PCEs of the PSCs were 9.85%, 10.6%, and 10.0%

for PFN-T-OH, PFN-BT-OH, and PFN-TBT-OH salts, respectively. Introducing a quaternized polymer between the ZnO and active layer could achieve excellent PCE of the PSCs. Additionally, the PCE of devices with quaternized OH salt reached 10.6% owing to the synergistic effect of hydrogen bonding between the ZnO layer and the hydroxyl group in the quaternary salt. Moreover, a robust intramolecular charge transfer occurred due to improved electron affinity in the electron-withdrawing moiety of BT.

2. Result and Discussion

1). Optical and electrochemical properties

We performed ultraviolet-visible (UV–Vis) spectroscopy to investigate the optical properties of the polymers. The polymer solutions were prepared by dissolution in methanol with a 6:1 acetic acid to polymer molar ratio. Figure 6 shows the absorption spectra of the CPE-based polymer thin film, and its optical properties are listed in Table 2.

The maximum absorption of the PFN-T film appeared at 430 nm (Figure 6a), which is slightly blue-shifted as compared to the PFN-T salt (414 nm) and PFN-T-OH salt (426 nm). A similar hypochromic shift was caused by the sodium salt end group to produce a conformational change in thiophene, as studied by Holdcroft et al.⁷⁵ The salts are held closer to the thienyl ring and exhibit steric effects, and the interaction between the salt substituent and

sulfur lone pair on adjacent rings plays a dominant role. Therefore, leading to the adjacent thienyl rings twisting and shortening of conjugation lengths.⁷⁶

As shown in Figure 6b, PFN-BT showed two broad absorption bands at 322 and 446 nm, respectively. A band in the shorter wavelength region corresponds to the $\pi-\pi^*$ transition and an extended wavelength region correspond to the intramolecular charge transfer (ICT) absorption, which is characteristic of conjugated polymers with donor-acceptor architecture. In the ICT region, the PFN-BT salt and PFN-BT-OH salt film showed absorption bands at 448 and 444 nm, respectively, which are nearly the same as the absorption maxima of PFN-BT. This is presumably because the terminal amino salt groups are unlikely to affect adjacent benzothiadiazole ring interactions in the film state.

The optimized molecular orbitals of PFN-BT (Figure 7b) showed no steric effect as the dimethyl aminopropyl fluorene and benzothiazole were far from each other. The PFN-TBT film exhibited two absorption bands (Figure 6c) at 395 and 565 nm, respectively.

The former band corresponds to the $\pi-\pi^*$ transition of the backbone, while the latter is related to ICT absorption. The absorption spectra of the PFN-TBT salt and PFN-TBT-OH salt showed the same features.

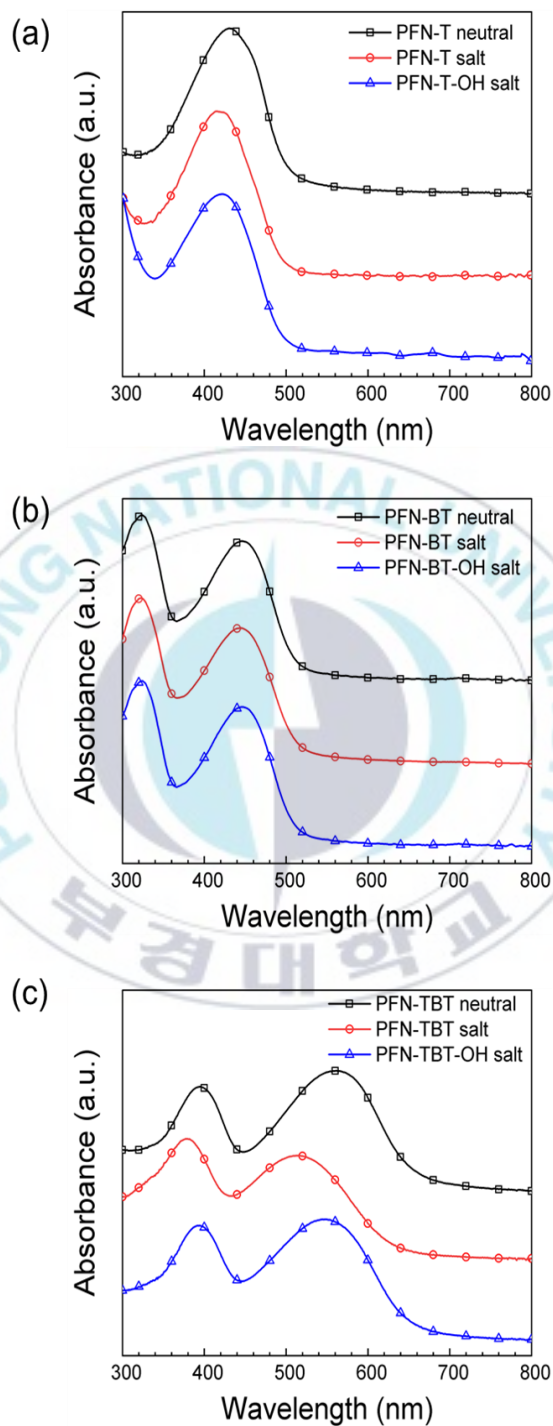


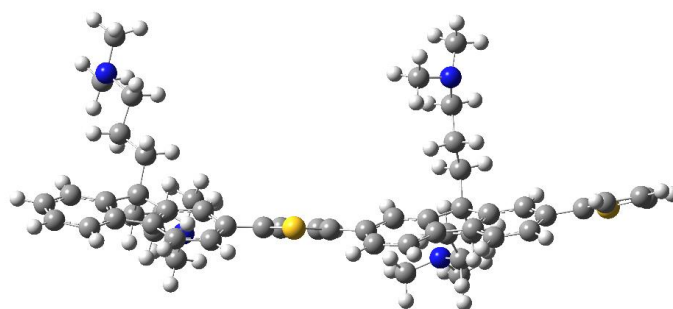
Figure 36. UV-Vis spectra of (a) PFN-T series, (b) PFN-BT series, and (c) PFN-TBT series films.

The maximum ICT absorption wavelengths of PFN-TBT salt and PFN-TBT-OH salt were 512 and 549 nm, respectively, which were blue-shifted than that of PFN-TBT. This is possibly due to the steric hindrance between the thienyl segment in the TBT group. The FN group causes twisting of the adjacent thienyl rings and shortening of conjugation lengths.

In the optimized computational structure of PFN-TBT (Figure 7c), the aminopropyl chain, in the fluorene unit, is settled in opposite directions to minimize electrostatic interactions. This effect bends the linkage between the two repeating units and produces a slight twist of the thiophene rings with the benzothiadiazole group.⁷⁷

The HOMO and LUMO energy levels of the polymers were determined from the oxidation and reduction onset potentials in cyclic voltammograms (CVs) (Figure 8). The CVs were calibrated referring to the ferrocene/ferrocenium (Fc/Fc^+) redox couple. Based on the onset reduction potential, the LUMO energy levels of PFN-T, PFN-BT, and PFN-TBT were -3.32, -3.18, and -3.43 eV, respectively

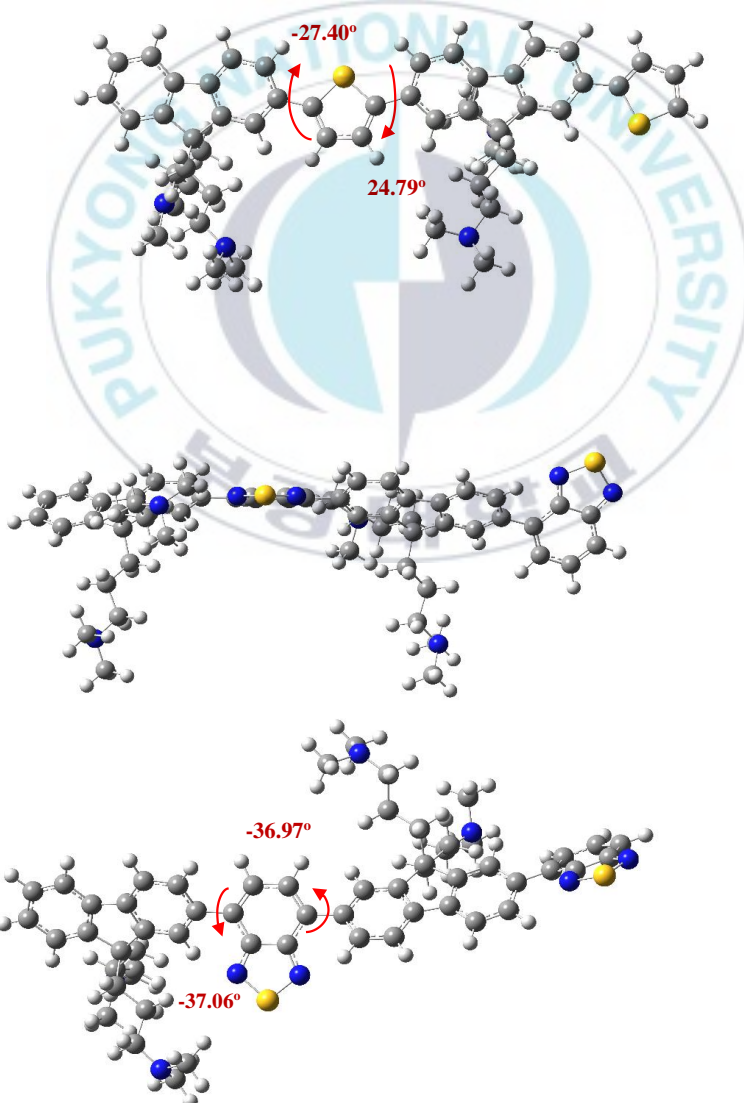
(a)



Dipole
Moment

1.60 D

(b)



Dipole
Moment

3.45 D

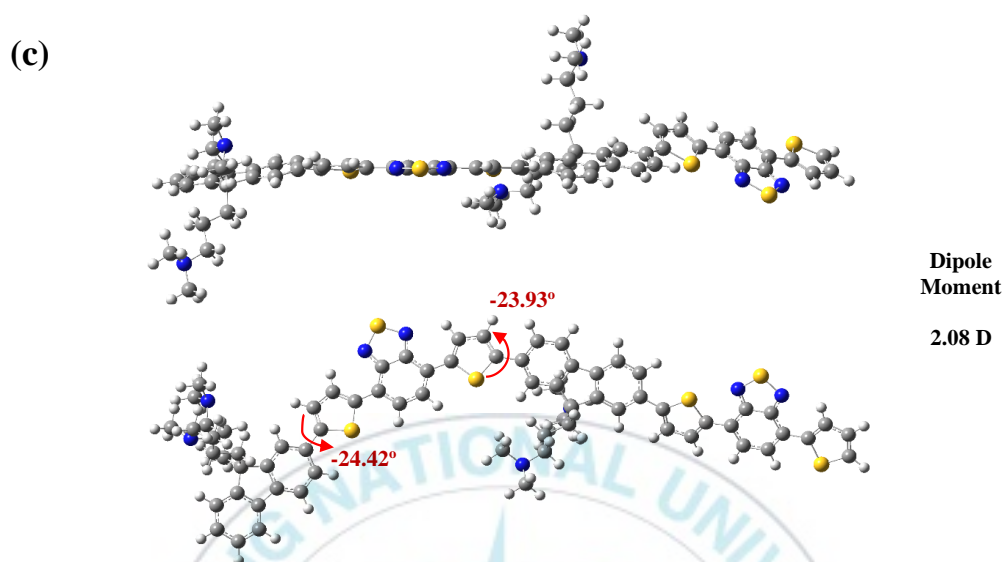


Figure 38. DFT-optimized geometries and dipolar properties of (a) PFN-T (b) PFN-BT (c) PFN-TBT calculated by B3LYP/6-31G (d) level

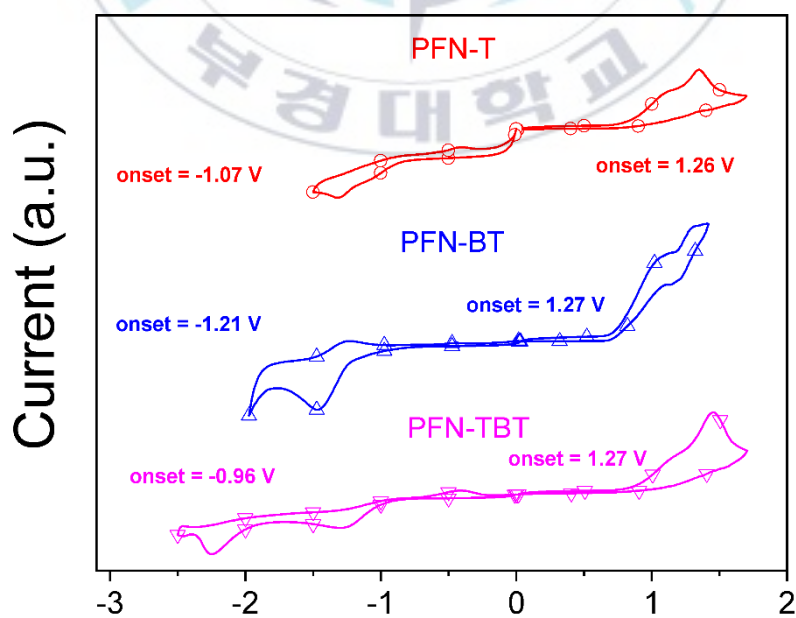


Figure 37. Cyclic voltammograms of CPEs

Table 7. Optical and electrochemical properties of CPE.

Sample	λ_{max}^a (nm)	λ_{edge}^b (nm)	HOMO ^c (eV)	LUMO ^d (eV)
PFN-T	430	502	-5.65	-3.32
PFN-T salt	414	493	-	-
PFN-T-OH salt	426	493	-	-
PFN-BT	322, 446	507	-5.57	-3.18
PFN-BT salt	322, 448	507	-	-
PFN-BT-OH salt	322, 444	507	-	-
PFN-TBT	395, 562	654	-5.66	-3.43
PFN-TBT salt	379, 512	628	-	-
PFN-TBT-OH	394, 549	646	-	-

a) maximum absorption

b) optical bandgap obtained from onset wavelength (λ_{edge}) of the film

c), d) obtained from oxidation and reduction onset potential of the cyclic voltammogram

The HOMO energy levels of PFN-T, PFN-BT, and PFN-TBT are estimated to be -5.65, -5.57, and -5.66 eV, respectively. The result indicates that different electron-donating functional groups influence the HOMO level of the fluorene-based polymer, unlike the LUMO level, which is stabilized by

introducing electron-withdrawing and electron-donating units on both sides of the FN.

2). Theoretical calculation of the polymers

The theoretical calculation was initially adopted to explore the electronic properties and provide preliminary insight into the geometric structures and dipolar properties of the interlayer materials. For simple computational calculations, the long side chains and polymer backbones were replaced with a methyl group and two repeating units. Density functional theory calculations were carried out with a B3LYP/6-31G(d) basis set based on the Gaussian suite of programs (Gaussian 09).⁷⁸

The optimized geometries of the CPE interlayer materials with dihedral angles and dipole moments are depicted in Figure 7. Dihedral angles are defined as the 180° torsional angle deviation between the adjacent fluorene units surrounding the connecting bond. A small dihedral angle (i.e., planar structure) promotes the delocalization of the π -electron system. Similarly, the bond length alternation parameter provides a quantitative measure of the homogeneous distribution of π electrons over the bonds (Peierls distortion) by comparing the consecutive bond length along the chain. Enhancing the electronic delocalization tends to equalize the bond lengths, reducing the bond length alternation.⁷⁹

The dihedral angles between the dimethylamino fluorene and thiophene moiety in PFN-T are -27.40° and 24.79° . The preferred conformation for thienyl rings is to be oriented anti, which minimizes the effect of steric hindrance.⁶³ The dihedral angles between dimethyl amino fluorene and benzothiadiazole moiety are -37.06° and -36.97° , suggesting that a strong steric hindrance effect occurs between the fluorene and BT moieties, adopting a nonplanar configuration, as depicted in (Figure 7b).⁸⁰ PFN-TBT showed the most planar geometry with dihedral angles of -24.42° and 23.93° . The thiophene linker between the FN segment and benzothiadiazole caused conformational effects. The structural variation resulted in a distinctly different dihedral angle between the thiophene unit and flanked benzene in the fluorene moiety.

In contrast to one thiophene bridge in PFN-T shows higher dihedral angles than PFN-TBT, which has two thiophene bridges. This thiophene bridge makes the backbone of PFN-TBT more flexible and increases the distance between the two polar groups, which weakens the repulsion to a certain degree to obtain smaller dihedral angles of PFN-TBT. The largest dihedral angle was observed from PFN-BT due to the interchain interaction. A reasonable conformation for fluorene-based polymer features all-trans or near trans conformation dihedral angle due to the fully trans conformation is energetically unfavorable (in case of being sterically hindered).⁸¹

The calculated dipole moments of the polymers are depicted in Figure 7. The trend was estimated as follows: PFN-BT (3.45 D) > PFN-TBT (2.08 D) > PFN-T (1.60 D). As shown in Figure 7, the thiophene (T) bridge in PFN-TBT and PFN-T caused small permanent dipoles. Distinguishingly, the PFN-BT has a benzothiadiazole group in the backbone at the opposite side of the polar group, which helps acquire a more decisive dipole moment (3.45 D). The dipole moment in this calculated result corresponds to the dihedral angle. Seo et al. reported that the larger interfacial dipole on the CPE could arise from the higher permanent dipole moment.¹⁷ The primary requirement of an interlayer is its ability to produce large interfacial dipoles that induce a vacuum-level shift to modify the electrode work function.⁸²

The frontier molecular orbitals of the two repeating units with theoretical HOMO/LUMO energy levels are shown in Figure 9. The calculated HOMO/LUMO energy levels exhibited similar trends in the UV–Vis and CV experiments. However, the CPE interlayer dimer orbital character showed different delocalized electrons. In particular, the HOMO energy levels are accessed when thiophene and benzothiadiazole are incorporated into the polymer backbone in PFN-T, PFN-BT, and PFN-TBT. Additionally, at the HOMO level, electrons are delocalized along the chain direction, whereas their localization takes place in the electron-withdrawing unit at the LUMO level for PFN-BT and PFN-TBT.

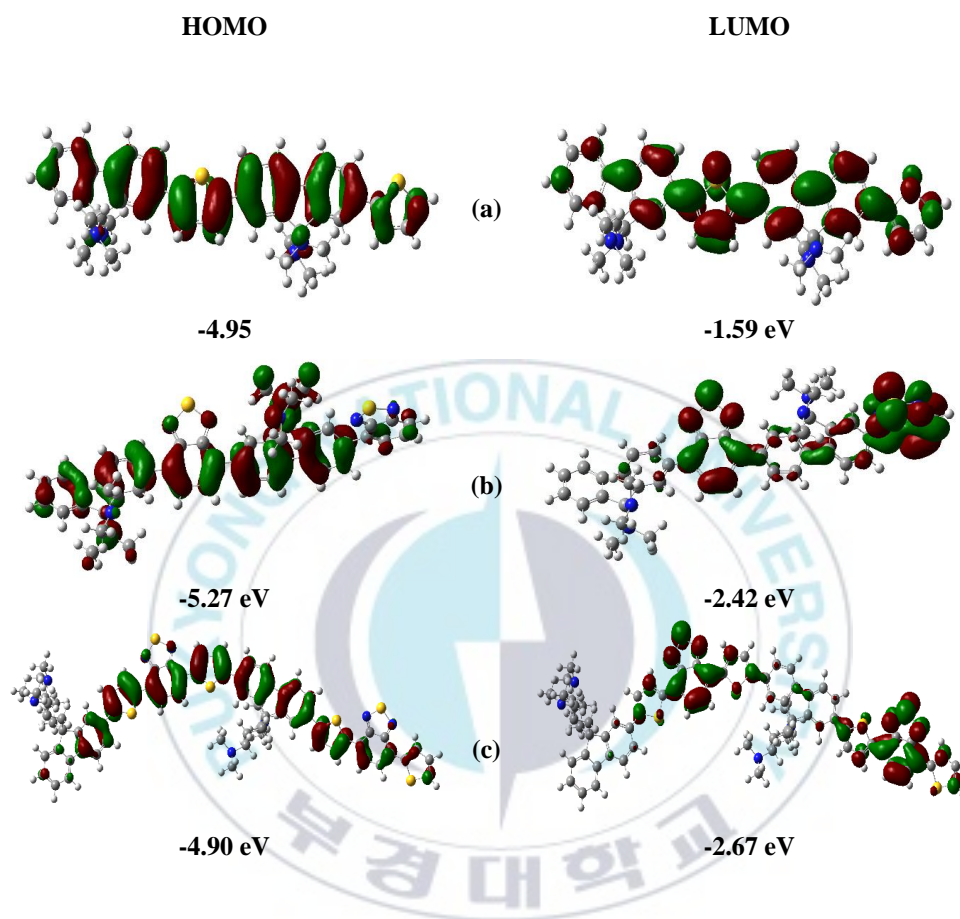


Figure 39. Frontier molecular orbitals of two-repeating unit models with HOMO/LUMO energy levels calculated at the B3LYP/6-31G** level for (a) PFN-T, (b) PFN-BT, and (c) PFN-TBT.

3). Optical simulation characteristic of CPEs using transfer matrix formalism

To confirm the role of the interlayer, an optical model for CPEs based devices was carried out using transfer matrix formalism (TMF). This provides a guideline for predicting the optimized device architecture. The optical constants, refractive index (n), and extinction coefficient (k) values of the CPEs, PTB7-Th:PC₇₁BM, were determined using ellipsometry spectroscopy and that of ITO, ZnO, MoO₃, and Ag were obtained from previous literature.^{83–86}

In this study, a MATLAB script was developed by the McGhee group, for transfer matrix optical modeling.⁸³ The absorption distribution over the film thickness was calculated in the wavelength range of 300–800 nm. Multiplying with the AM 1.5 sun spectrum and integration over the film thickness results in optical electric field profiles corresponding to various position wavelengths are depicted in Figure 10.⁸⁷ The device with interlayer showed prominent electrical field peaks located inside the active layer for the three incident lights from 350 to 650 nm.

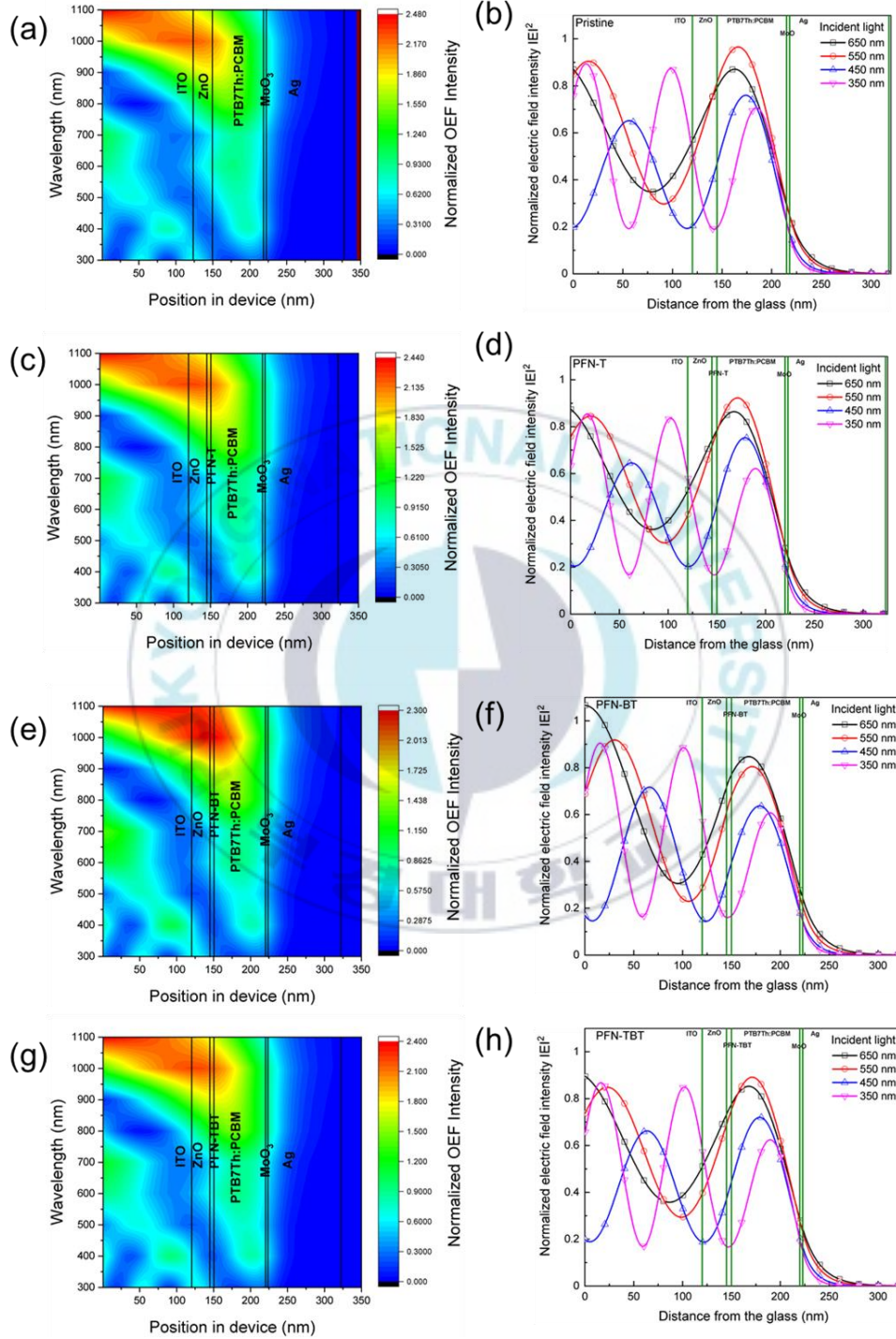


Figure 40. Optical electric field intensity of (a, b) pristine, (c, d) PFN-T, (e, f) PFN-BT, and (g, h) PFN-TBT by TMF optical

This simulation indicates that the interlayer structures cause a slight change in the optical electric field (OEF) distribution. As depicted in Figure 10a, c, e, and g the device with pristine ZnO showed the lowest OEF intensity as compared to devices with interlayer, while the device based on PFN-BT showed the highest OEF intensity.

The field intensity over the entire wavelength range of 300–1100 nm was mapped to obtain OEF distribution details. Figure 10b, d, f, and h, show the normalized field intensity versus distance for each layer in the solar cell and incident light wavelength. Visibly, the 350–650 nm wavelength region shows the slight influence of thin-film interference, with higher OEF developing from constructive interference.

Although very thin, ± 5 nm CPE layers exist, the alteration in the OEF distribution spectra indicates that the optical effect of the CPE backbone is responsible for the modifications in the interlayer active layer region in the device. The OEF spectra of devices with PFN-BT show the highest intensity, which is strongly influenced by the parasitic absorption of CPEs and the constructive and destructive interference between incident and reflected light.⁸⁵

4). Investigation of CPE-covered ZnO surface

Water contact angle characterization is used to provide intuitive information about surface component wettability. The ZnO/CPEs surface properties were investigated by water contact angle measurements (Figure 11). The water contact angle of the ZnO/neutral polymer category was higher than that of the ZnO/salt polymers and OH salt polymers due to the hydrophobic properties of the neutral polymer category. The water contact angles of the ZnO surface with PFN-T, PFN-BT, and PFN-TBT were 50.9°, 51.3°, and 51.9°, respectively, which was higher than the pristine ZnO value (28.6°). In Figure 11, quaternized CPEs showed a low water contact angle due to increased polymer salt hydrophilicity and hydrogen bond formation of the polymer-OH salt. The values for PFN-T salt, PFN-BT salt, and PFN-TBT salt are 42.3°, 37.3°, and 48.7°, respectively and those for PFN-T-OH salt, PFN-BT-OH salt, and PFN-TBT-OH salt are 31.3°, 32.8°, and 44.6°, respectively. In general, a small water contact angle indicates a suitable wetting property and is advantageous for using PFN-modified interlayer in solar cells.

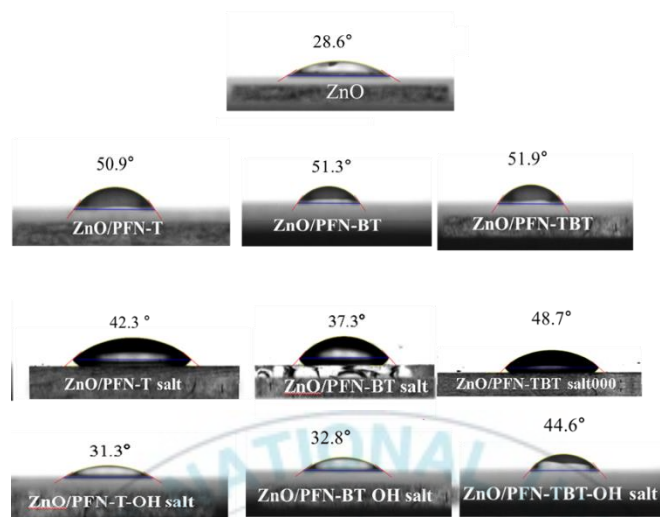


Figure 41. Static water contact angle data of ZnO, ZnO/neutral polymers, ZnO/salt polymers, and ZnO/OH salt polymers

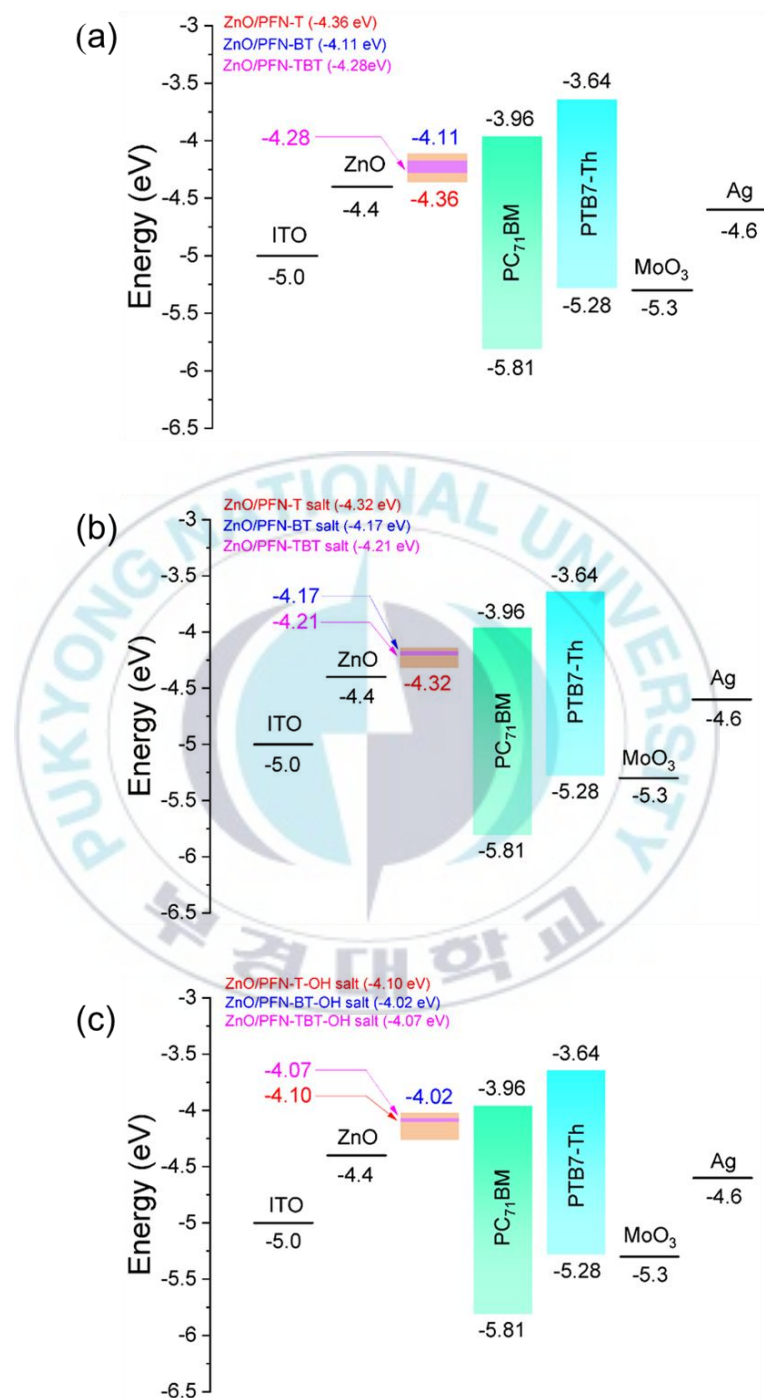


Figure 42. Energy level diagrams of (a) ZnO/neutral, (b) ZnO/salt, and (c) ZnO/OH salt polymer categories.

Kelvin probe microscopy measurements were performed to investigate the influence of CPEs on the ZnO work function. Figure 12 shows the work function (WF) of ZnO with neutral, salt, and OH salt polymer categories. The WF of ZnO with neutral PFN-T, PFN-BT, and PFN-TBT were -4.36, -4.11, and -4.28 eV, respectively. The WF based on PFN-T salt, PFN-BT salt, and PFN-TBT salt were -4.32, -4.17, and -4.21 eV, respectively. The WF based on PFN-T-OH salt, PFN-BT-OH salt, and PFN-TBT-OH salt were -4.10, -4.02, and -4.07 eV, respectively. The WF values for ZnO with interlayers were higher than that of ZnO without an interlayer (-4.4 eV). The mechanism resulting in PCE improvement is attributed to the WF change at the ZnO surface by interface dipole formation,⁸⁸ which can be tuned by introducing an interlayer, that is the transition from a Schottky to an Ohmic contact. Thus, the reduced barrier height at the ZnO surface might improve the charge collection capability.^{65,89,90}

For polymer salts, a higher interface dipole can be expected because the polymer salt dipole moment magnitude may be greater than that of neutral polymers. The neutral polymer is soluble in alcohol in the presence of a small amount of acetic acid due to weak interaction between the nitrogen atoms in the side chain and the acetic acid. Compared to polymer salts, it is easily dissolvable in a polar solvent. Neutral amine groups in neutral polymers are primarily physisorbed onto the ZnO surface.^{91,92}

The WF reduction and energy level adjustment are due to the amine CPE intrinsic molecular dipole (μMD) synergistic effect acting perpendicular to the surface and the interfacial dipole (μID) formed at the interface of the modifier molecules and electrode surface.⁹³ The contribution of μID is attributed to partial electron transfer from the amine-containing molecules to the electrode surface.⁹⁴ It has been demonstrated that amine and hydroxyl groups can be spontaneously adsorbed on the ZnO surface, resulting in dipolar polymerization.⁹⁵ The magnitude of dipole moment based on the OH salt polymer category is higher than that of polymer salts due to polar $-\text{OH}$ groups, which generate a synergistic effect in the dipole moment magnitude. Thus, the magnitude of the interface dipole moment for OH salt polymer category > salt polymer category > neutral polymer category. The trend for J_{SC} is the trend of the WF. Generally, the WF difference in the charge transporting layer is not the main factor affecting the built-in potential and V_{OC} for Fermi-level pinning.⁹⁶

J. Park et al. studied the spontaneous organization of side chains on CPE.⁹⁷ Based on our previous study, we discovered that the CPE quaternized side chain affects the WF and wetting ability due to the spontaneous arrangement of the side chain.^{98,99} In the stacking device architecture, upon introducing an interlayer between ZnO and the active layer, the ionic groups on the CPE backbone are directed away from the active layer surface.

Simultaneously, the side chains pointed toward the ZnO layer owing to the spontaneous re-organization. The increased number of accumulated ionic groups on the CPE led to an Ohmic contact and better wettability of the active layer.

5). Photovoltaic properties

To investigate the photovoltaic properties of the device with CPE interlayers, we constructed and tested inverted-type PSCs with an ITO/ZnO/interlayer/PTB7-Th:PC₇₁BM/MoO₃/Ag structure (Figure 13a). The current density–voltage ($J - V$) curves of the PSCs with the PFN CPE interlayer under illumination (inset under the dark condition) are shown in Figure 13b–c. Additionally, the photovoltaic parameters are summarized in Table 3. Devices based on the PFN interlayer showed higher PCEs than those based on pristine ZnO. This indicates that PFN derivatives are potential materials for interfacial modification to improve device performance. The PCEs of the PSCs with the neutral category of PFN-T, PFN-BT, and PFN-TBT were 8.80%, 9.94%, and 9.43%, respectively. The relative improvements in the PCE based on PFN-BT, and PFN-TBT were 13.7%, and 7.89%, respectively, upon comparison with the pristine ZnO-based device. However, the PCE of the device based on PFN-T was almost identical to that of the device based on pristine ZnO. The improvement in the performance of

neutral PFN category devices mainly arise from the enhancement of J_{SC} and FF , simultaneously.

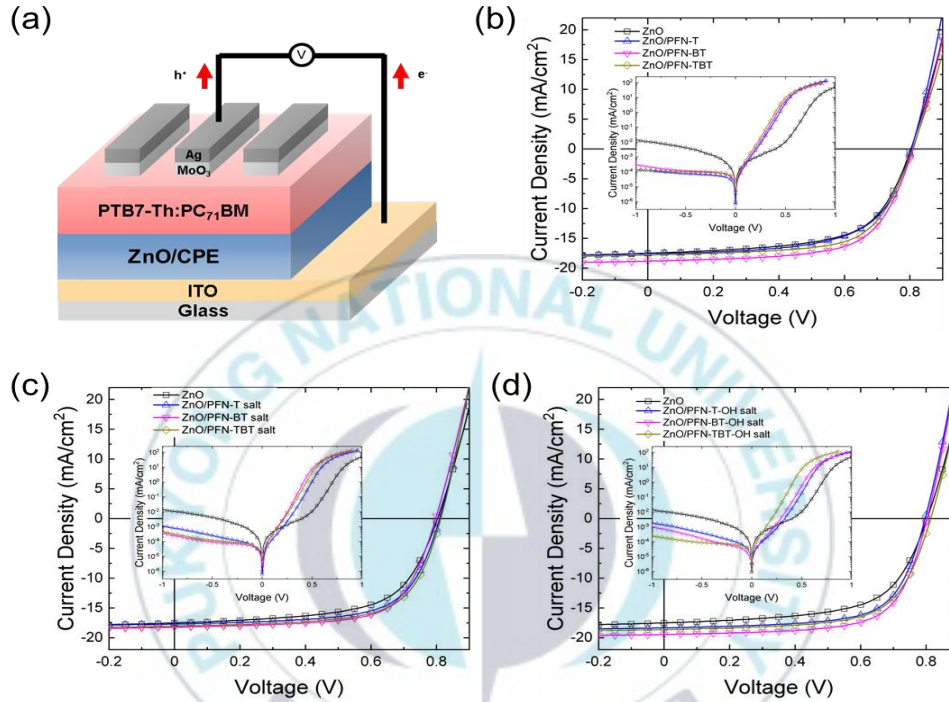


Figure 43. Figure (a) Device architecture, J - V curves of PSCs based on (b) neutral, (c) salt, and (d) OH salt polymer

The devices based on the salt polymer category exhibited improved performance as compared to the device based on pristine ZnO. The PCEs of the devices based on the PFN-T salt, PFN-BT salt, and PFN-TBT salt were 9.43%, 9.87%, and 9.74%, respectively. The highest PCE was observed for the device with PFN-BT. The PCE improvement of the devices based on PFN-T salt, PFN-BT salt, and PFN-TBT salt were 7.89%, 12.93%, and 11.4%, respectively upon comparison with pristine ZnO devices. The PCEs of the

Table 8. The performances of the PSCs with CPEs with the best PCE. The averages (20 devices are averaged) are summarized in parentheses.

	J_{sc}^a (mA/cm ²)	$J_{sc, cal}^b$ (mA/cm ²)	V_{oc} (V)	FF (%)	PCE (%)	R_s^b (Ω cm ²)	R_{sh}^c (Ω cm ²)
ZnO	17.5 (17.4)	17.5	0.80 (0.80)	62.2 (62.1)	8.74 (8.71)	5.26	552
ZnO/PFN-T	17.6 (17.5)	17.6	0.81 (0.80)	62.3 (61.6)	8.80 (8.69)	4.40	578
ZnO/PFN-BT	18.8 (18.7)	18.8	0.81 (0.81)	65.4 (63.9)	9.94 (9.78)	4.05	710
ZnO/PFN-TBT	17.8 (17.7)	17.9	0.81 (0.81)	65.4 (64.7)	9.43 (9.32)	4.29	714
ZnO/PFN-T salt	17.7 (17.6)	17.7	0.81 (0.80)	66.3 (65.4)	9.43 (9.28)	4.34	792
ZnO/PFN-BT salt	18.2 (18.1)	18.2	0.80 (0.80)	67.4 (66.7)	9.87 (9.65)	4.09	899
ZnO/PFN-TBT salt	18.0 (17.9)	18.1	0.81 (0.81)	66.7 (65.6)	9.74 (9.64)	4.17	814
ZnO/PFN-T-OH salt	18.3 (18.2)	18.9	0.80 (0.80)	67.0 (66.4)	9.85 (9.79)	4.04	911
ZnO/PFN-BT-OH salt	19.4 (19.3)	19.5	0.80 (0.80)	68.4 (67.3)	10.6 (10.5)	3.76	916
ZnO/PFN-TBT-OH salt	18.6 (18.5)	19.2	0.81 (0.80)	66.4 (66.3)	10.0 (9.96)	3.98	905

^a calculated from the IPCE curves, ^b series, and ^c shunt resistance under illumination

devices based on PFN-T-OH salt, PFN-BT-OH salt, and PFN-TBT-OH salt were 9.85%, 10.6%, and 10.0%, respectively. The devices with the OH salt polymer category showed significantly improved PCEs. Essentially, the side chain functionality helped increase device performance. Note that the calculated J_{sc} values obtained from the Incident photon-to-current

efficiency (IPCE) curves (Figure 14) were in good agreement with the values obtained under 1.0 sun illumination.

The PCE of the devices based on the neutral polymer category was in the order of PFN-BT > PFN-TBT > PFN-T. The result well agreed with the calculated dipole. The synergistic effect from the side chain and different backbone structures influence the interfacial dipole magnitude and direction. PFN-T exhibited the lowest PCE among the neutral polymers owing to the lowest interfacial dipole moment and optical effect. The thienyl rings were twisted and had shorter conjugation lengths.⁷⁵

The comprehensive and planar π -conjugated system in PFN-TBT affects WF and charge mobility. Thus, PFN-TBT showed a higher PCE than PFN-T. The benzothiadiazole, in PFN-BT, enhanced electron mobility due to the high content of electron-deficient BT units. This was probably due to the non-covalent attractive interactions between S, C, H (in thiophene), and nitrogen (in BT), which minimized the torsional angle.⁷⁶

A smaller torsional angle maximizes the polymer planarity chain, resulting in efficient charge transport. Thus, PFN-BT showed better performance as compared to PFN-T and PFN-TBT. The PCE of the devices based on salt polymer and OH salt polymer category follows the trend of the PCEs in the neutral polymer category.

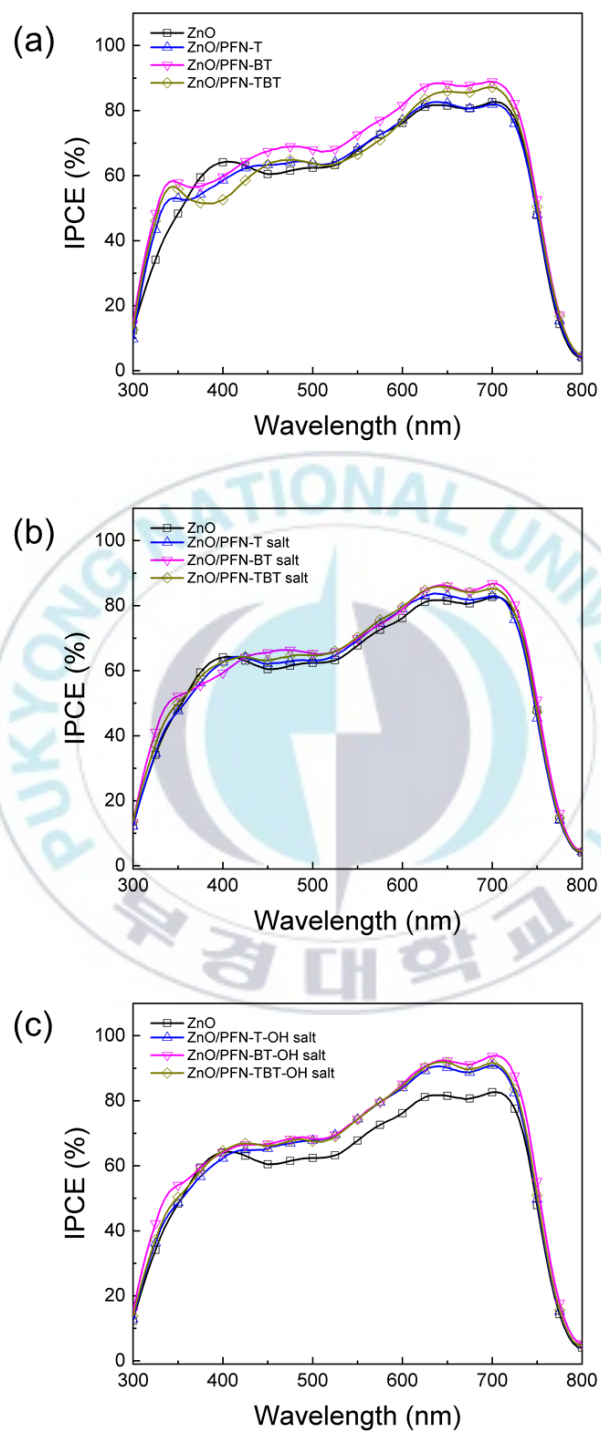


Figure 44. . IPCE graph of (a) neutral polymer category, (b) salt polymer category, (c) OH salt polymer category

Devices without an interlayer exhibited the lowest performance, where the combination of low V_{OC} , J_{SC} , and FF resulted in an 8.74% PCE. The lowest performance of the device based on pristine ZnO among the devices can be explained by a mismatch of the WF between the active and electrode layers and low charge extraction due to high contact resistance.^{65,89,90}

A noticeable correlation was found between the CPE functionality and the PCEs of the devices. Devices based on salt polymers as the interlayer exhibited improved PCEs as compared to devices based on neutral polymers. Notably, the PCE improvement mainly resulted from the J_{SC} enhancement.^{61,71,100,101} The work function data agree well with the trend of J_{SC} data. (Figure 15)

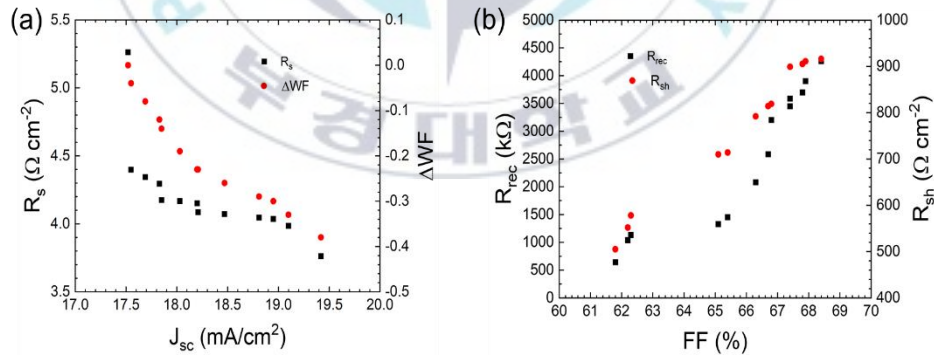


Figure 45. Correlation of (a) J_{sc} and R_s as function ΔWF (WF of ZnO with interlayer – WF of ZnO) work function as a function of J_{sc} and (b) R_{rec} and R_{sh} as a function of FF

The electron mobilities of the devices [ITO/ZnO with or without interlayer/PC₇₁BM (60 nm)/Al (100 nm)] were studied to understand the effect of the interlayer on the device electron transport properties. The Mott-Gurney law was adopted to calculate electron mobility.¹⁰² We can easily notice that the electron mobilities of the devices with PFN as the interlayer are higher than the device based on pristine ZnO ($2.64 \times 10^{-3} \text{ cm}^2\text{V}^{-1}\text{s}^{-1}$). The electron mobilities of devices with PFN-T, PFN-BT, and PFN-TBT were 2.76×10^{-3} , 4.13×10^{-3} , and $3.41 \times 10^{-3} \text{ cm}^2\text{V}^{-1}\text{s}^{-1}$, respectively. The calculated electron mobilities of the devices based on PFN-T salt, PFN-BT salt, and PFN-TBT salt were 3.01×10^{-3} , 3.87×10^{-3} , and $3.71 \times 10^{-3} \text{ cm}^2\text{V}^{-1}\text{s}^{-1}$, respectively. Besides, the electron mobilities of devices based on PFN-T-OH salt, PFN-BT-OH salt, and PFN-TBT-OH salt were 4.27×10^{-3} , 4.66×10^{-3} , and $4.3 \times 10^{-3} \text{ cm}^2\text{V}^{-1}\text{s}^{-1}$, respectively.

The higher electron mobilities of the devices with salt polymer and OH salt polymer category were higher than those of the devices based on the neutral polymer category, which can be explained by their better cathode modification capability, and the larger electron mobilities of the devices with interlayer based devices can be ascribed to the trend of J_{SC} data of the PSCs.

As summarized in Table 3, the series resistance (R_s) was determined from the inverse slope near the high current regime in the current density–

voltage curves obtained under 1.0 sun conditions. The R_s , under the illuminated condition, of the devices with PFN-T, PFN-BT, and PFN-TBT were 4.40, 4.05, and 4.29 Ωcm^2 , respectively. As for the polymer salt category, PFN-T salt, PFN-BT salt, and PFN-TBT salt-based device, the R_s values were 4.34, 4.09, and 4.17 Ωcm^2 , respectively. The R_s values for devices based on PFN-T-OH salt, PFN-BT-OH salt, and PFN-TBT-OH salt were 4.04, 3.76, and 3.98 Ωcm^2 , respectively. The R_s data for pristine ZnO was 5.26 Ωcm^2 . The R_s values of the devices have strong correlations with the trend in the PSC polymer photovoltaic properties (Figure 15).

This R_s could be attributed to the Ohmic loss of the entire device, including bulk and contact resistance. Therefore, R_s was affected by the resistivity of the pristine ZnO, ZnO/interlayer, and factors such as the contact resistance between different layers.¹⁰³ The excellent FF can be further verified by R_s and shunt resistance (R_{sh}) calculated from the $J - V$ curves. The smallest R_s and the largest R_{sh} values indicate that the charge carrier transport and collection ability are enhanced by using ZnO/CPEs, resulting in an increase in FF and PCE.¹⁰⁴ R_{sh} represents current leakage from the cell edges and the device. Several groups have reported that metal atoms, during thermal evaporation, can damage the active layer surface and diffuse inside the blend. Metal atoms are active centers for carrier recombination; hence, the current loss increases as reflected by a decrease in R_{sh} .¹⁰⁵ The R_{sh}

value was obtained from the $J - V$ curve under illumination. The R_s of the devices based on PFN-T, PFN-BT, and PFN-TBT were 578, 710, and 714 $k\Omega cm^2$. For the devices based on PFN-T salt, PFN-BT salt, and PFN-TBT salt, the R_{sh} values were 505, 792, 899, and 814 $k\Omega cm^2$. The R_{sh} values for the device based on PFN-T-OH salt, PFN-BT-OH salt, and PFN-TBT-OH salt were 911, 916, and 905 $k\Omega cm^2$, respectively, which are higher than that of devices with pristine ZnO (552 $k\Omega cm^2$).

This R_{sh} is consistent with the device FF values, suggesting that the interlayer helps increase the R_{sh} by eliminating short circuits between the contacts, which contributes to increased device efficiency. However, the increased shunt resistance may not be the sole reason for the increased device efficiency. The incorporation of CPE as an interlayer in the devices can also influence their electrical characteristics.

The R_{sh} of the CPE-based device increases as neutral < salt < OH salt polymer category. Additionally, the R_{sh} tendency increases coherently with FF , indicating improved device characteristics. Electrical properties, such as low series resistance and high shunt resistance, of the devices, based on neutral polymer, salt polymer, and OH salt polymer category, are responsible for the increased FF .

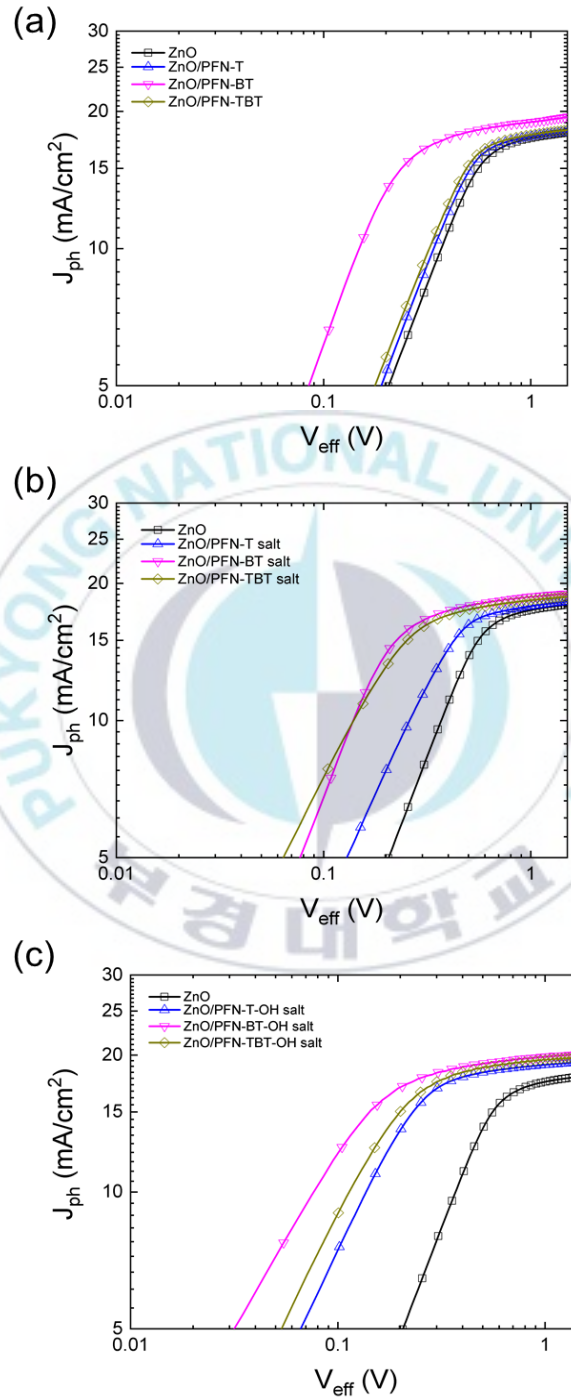


Figure 46. Photocurrent (J_{ph}) density vs. effective voltage (V_{eff}) of (a) neutral, (b) salt, and (c) OH salt polymer category.

We evaluated the relationship between photocurrent density (J_{ph}) and effective voltage (V_{eff}) to understand the charge transport and collection properties of the devices with and without an interlayer. Here, J_{ph} and V_{eff} were defined by J_L (measured current density under illumination) – J_D (measured current density in dark conditions) and V_0 (voltage at $J_{ph} = 0$) – V_a (applied voltage), respectively.

As shown in Figure 16, the $\log(J_{ph})$ vs. $\log(V_{eff})$ showed a linear relationship with a low V_{eff} range and began saturating at a high V_{eff} region. The V_{eff} values of the devices, in the saturated photocurrent regime (V_{sat}), based on PFN-T, PFN-BT, and PFN-TBT were 0.53, 0.22, and 0.53 V, respectively, which were smaller than that of the pristine ZnO-based device (0.56 V). The V_{sat} values of the devices based on PFN-T salt, PFN-BT salt, and PFN-TBT salt were 0.44, 0.33, and 0.26 V, respectively. Additionally, the V_{sat} values of the devices with PFN-T-OH salt, PFN-BT-OH salt, and PFN-TBT-OH salt were 0.27, 0.18, and 0.24 V, respectively.

Noticeably, the magnitude of the V_{sat} is in the order of neutral polymer > salt polymer > OH salt polymer categories. This trend corresponds with the change in J_{SC} and PCE of the devices because a smaller V_{sat} indicates a faster transition from the space-charge-limited to the saturation regime. In other words, there is a low V_{sat} energy barrier in the devices.

The saturation current density (J_{sat}) can be correlated with the maximum exciton generation rate (G_{max}), exciton dissociation probability, carrier transport, and collection probability at high V_{eff} . The G_{max} depends on the absorption of light on the active layer and was determined by $J_{ph}/q \cdot L$, where q is the electron charge and L is the thickness of the active layer.¹⁰⁶

Additionally, the carrier transporting and collecting probability current saturation point was estimated using J_{ph}/J_{sat} at any V_{eff} . The G_{max} under the J_{sat} condition of the devices based on pristine ZnO was $1.57 \times 10^{28} \text{ m}^{-3}\text{s}^{-1}$ and for the ZnO/PFN-T, ZnO/PFN-BT, and ZnO/PFN-TBT were 1.58×10^{28} , 1.68×10^{28} , and $1.61 \times 10^{28} \text{ m}^{-3}\text{s}^{-1}$, respectively. The PFN-T salt, PFN-BT salt, and PFN-TBT salt derivatives-based devices exhibited G_{max} values of 1.58×10^{28} , 1.62×10^{28} , and $1.59 \times 10^{28} \text{ m}^{-3}\text{s}^{-1}$, respectively. The G_{max} values for PFN-T-OH salt, PFN-BT-OH salt, and PFN-TBT-OH salt-based devices were 1.64×10^{28} , 1.69×10^{28} , and $1.73 \times 10^{28} \text{ m}^{-3}\text{s}^{-1}$, respectively.

No significant change was observed in G_{max} as it is dependent on the active layer absorbance. The J_{sat} is limited by carrier transport and collection upon dissociation of photo-generated excitons into free-charge carriers at high V_{eff} .⁶⁹ The point of V_{eff} reached at saturated photocurrent, G_{max} and the carrier transporting and collecting probability have strong

correlation with the trend in J_{SC} values. These values reveal that CPEs exhibited reduced charge recombination and increased charge collection capability at the cathode layer interfaces.

The dependence of J_{SC} and V_{OC} on light intensity (P_{light}) was measured to investigate charge carrier recombination, which has been shown via the J_{SC} vs. P_{light} and V_{OC} vs. P_{light} curves and their slopes. The relationship between J_{SC} and P_{light} is explained by the equation $J_{SC} \propto (P_{light})^\alpha$, where the value of α is unity when the bimolecular charge recombination is negligible.¹⁰⁷

As shown in Figure 17, the α value of the device without the interlayer was 0.960. α values of devices with PFN-T, PFN-BT, and PFN-TBT were 0.964, 0.967, and 0.972, respectively. α values for devices based on PFN-T salt, PFN-BT salt, and PFN-TBT salt were 0.975, 0.957, and 1.029, respectively. The devices based on PFN-T-OH salt, PFN-BT-OH salt, and PFN-TBT-OH salt showed α values of 0.966, 0.960, and 0.974, respectively. According to the results, devices, which exhibit bimolecular recombination, are suppressed in PSCs with CPE interlayers. In BHJ-type solar cells, bimolecular recombination occurs mainly at the donor-acceptor interfaces of the active layer and the interlayers. Devices have suppressed recombination because of the decreased space charge at the interfaces.¹⁵

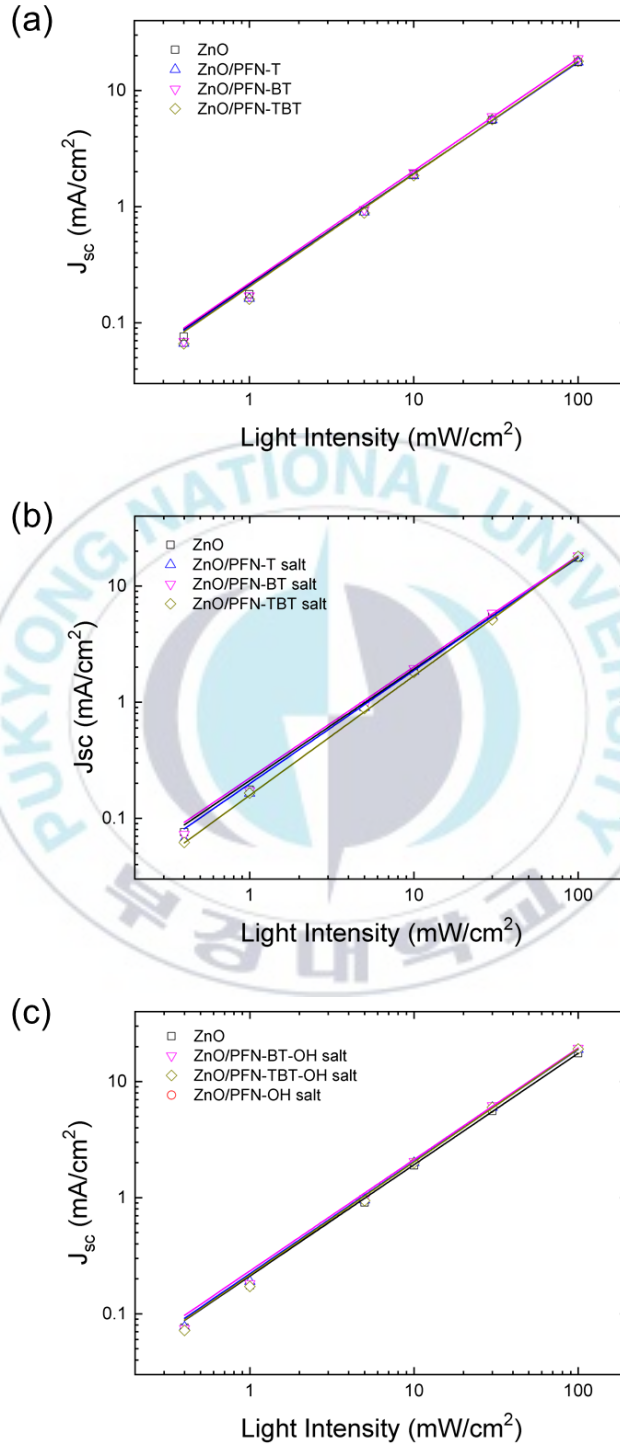


Figure 47. The dependence of J_{sc} on light intensity of (a) neutral, (b) salt, and (c) OH salt polymer category.

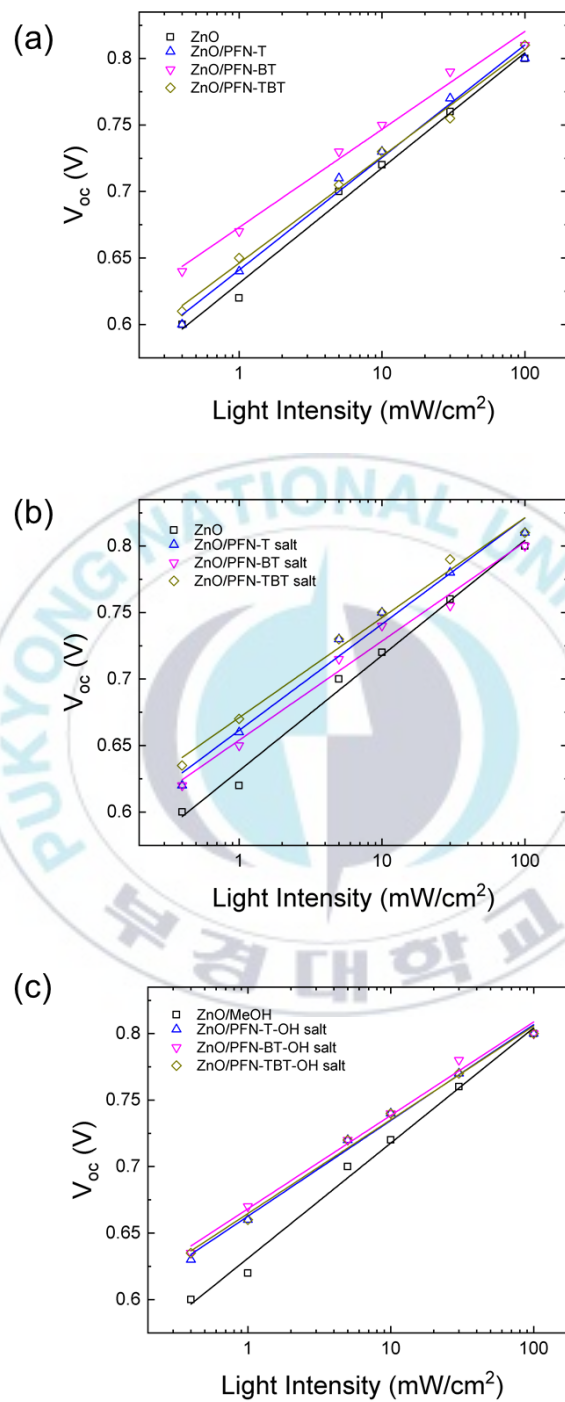


Figure 48. The dependence of V_{oc} on the light intensity of (a) neutral polymer category, (b) salt polymer category, (c) OH salt polymer category.

The relationship between V_{oc} and intensity (P_{light}) is explained by $V_{oc} \propto \frac{skT}{q} \ln \ln (P_{light})$, where k, T, q , and P_{light} are the Boltzmann constant, temperature in Kelvin, electron charge, and illumination intensity, respectively. The slope s of the V_{oc} vs. P_{light} curve provides information about trap-assistance recombination. The slope has a value of 1 when band-to-band (Langevin) recombination is superior to trap-assistance recombination. If devices have only trap-assisted recombination, the s value is 2. The slopes of the V_{oc} vs. P_{light} curves with and without the PFN of CPE-based devices are shown in Figure 18.

For neutral polymers, devices without the PFN interlayer exhibited an s value of 1.46. The s values of devices based on PFN-T, PFN-BT, and PFN-TBT were 1.43, 1.25, and 1.36, respectively. The s values for devices based on PFN-T salt, PFN-BT salt, and PFN-TBT salt were 1.35, 1.87, and 1.27, respectively. The devices based on PFN-T-OH salt, PFN-BT-OH salt, and PFN-TBT-OH salt have s values of 1.22, 1.19, and 1.19, respectively. These results prove the effectiveness of CPEs on less trap existence. The changes in the s values of devices correspond with the trend shown by PCEs of PSCs and follow the FF trend.

6). Electronic impedance spectroscopy (EIS) of PSCs

Electronic impedance spectroscopy (EIS) was performed to investigate the carrier transport and recombination mechanism. As shown in Figure 19 were fitted to estimate the recombination resistance (R_{rec}).

Efficient charge collection was implied by transport resistance, which is smaller than the R_{rec} . The EIS spectra followed the Gerischer impedance model for intense recombination situations. The absence of a transmission line indicates that the devices experienced strong recombination.

In the Nyquist plots, the respective electrochemical steps, with different time constants, are represented by semicircles. The distance between the intercepts at the real axis corresponds to the charge-transfer resistance of the device.^{107–114} The larger the EIS semicircle, the greater the R_{rec} . The higher R_{rec} values are related to the charge extraction capability at the ZnO interfaces.

The R_{rec} values for devices based on PFN-T, PFN-BT, and PFN-TBT were 1133, 1326, and 1450 k Ω , respectively. The R_{rec} values for devices based on PFN-T salt, PFN-BT salt, and PFN-TBT salt were 2081, 3585, and 2582 k Ω , respectively. The R_{rec} values for devices based on PFN-T-OH salt, PFN-BT-OH salt, and PFN-TBT-OH salt were 3899, 4620, and 3694 k Ω , respectively. The semicircle size increased, leading to an increase in R_{rec} .

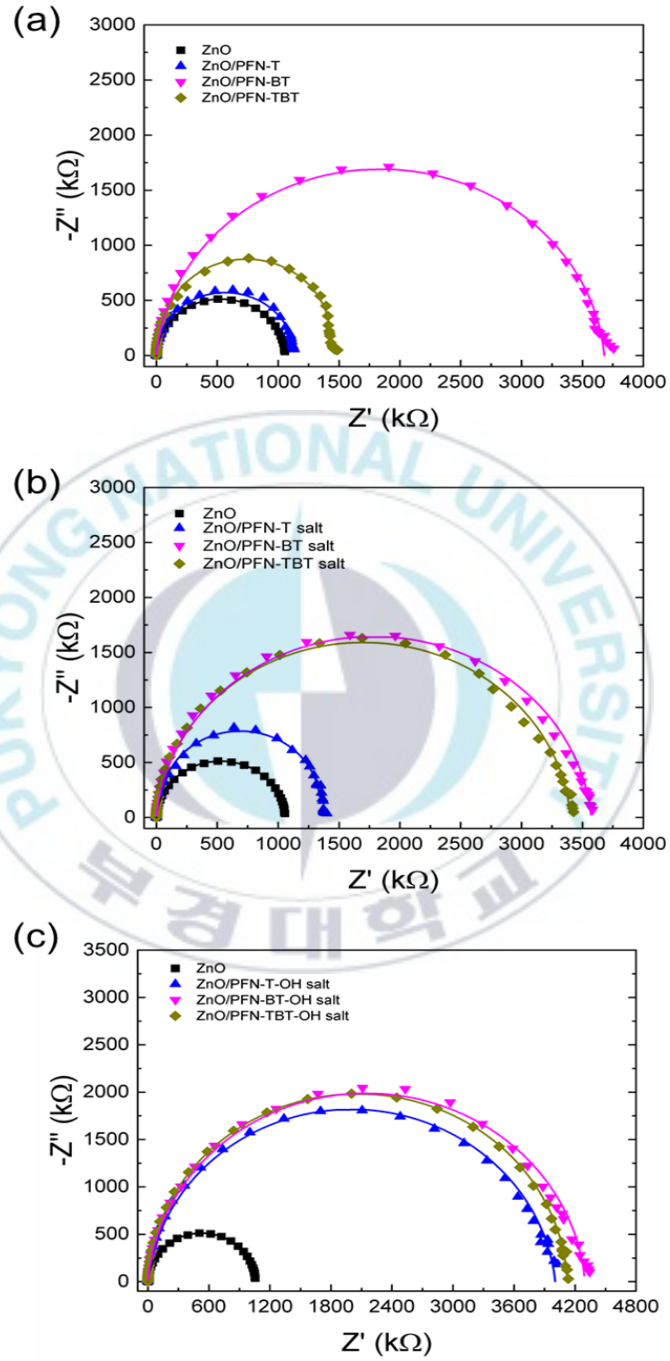


Figure 49. Impedance spectra of (a) neutral, (b) salt, and (c) OH salt polymer category

The R_{rec} magnitude of the device was in the order: neutral polymer < salt polymer < OH salt polymer categories indicating that the lowest reduced interfacial recombination corroborates with the R_{sh} and FF of PSCs. Additionally, the EIS results are consistent with the relationship between the V_{oc} and intensity (P_{light}) of PSCs.

3. Conclusion

We synthesized and characterized a series of CPEs divided into three categories: neutral polymer, salt polymer, and OH salt polymer. Each category contained four different backbones (thiophene, benzothiadiazole, and dithienylbenzothiadiazole). The CPEs were introduced as interlayers in inverted PSCs with an ITO/ZnO/CPE/PTB7-Th: PC71BM/MoO₃/Ag structure. The highest PCE, of 10.6%, was achieved with the PFN-BT-OH salt. Combined with surface contact angle measurement, optical simulation, and photovoltaic characterization of solar cells, we found that PCEs of the CPE-based devices depended on the backbone structure and side chain functionality. Different backbone structures resulted in varied molecular dipole moments, and the side chain functionality induced a larger interface dipole and spontaneous organization. This synergistic effect of the backbone and the side chain functionality, and J_{sc} improvement heavily contributed to PCE enhancement due to energy offset reduction at the cathode interface.

Chapter III

Effect of the Side Chain Functionality of the Conjugated Polyelectrolytes as a Cathode Interlayer Material on the Photovoltaic Performances



Reproduces with permission from

[Macromolecular Research 30, 2 (2022) 146]

Copyright © The polymer Society of Korea and Springer 2021

Effect of the Side Chain Functionality of the Conjugated Polyelectrolytes as a Cathode Interlayer Material on the Photovoltaic Performances

1. Introduction

As a promising photovoltaic technology, polymer bulk heterojunction solar cells (PSCs) based on the combination of an electron donor and an electron acceptor with a bulk heterojunction (BHJ) is more advantageous over the conventional device structure.^{115–118} PSCs are attractive, clean, and renewable energy generations. PSCs based on conjugated polymers have a great deal of attention due to mechanical flexibility, lightweight, low-cost energy sources, large scale, and fabrication through roll-to-roll printing.^{46,48,49,119–122}

The excitons (electron-hole pair) in BHJ generated in the photoactive layer need to dissociate into holes and electrons for charge extraction. However, owing to the short exciton diffusion lengths typically less than 10 nm, and lifetimes of 10 ns organic semiconductors. Such distances are within the exciton pair mean free-path lengths (the minimum diffusion distance before the exciton can be annihilated via recombination). The BHJ

morphology with a well-interpenetrating network is required to assure efficient exciton dissociation and transport before their decay to the ground state.^{50,51,123,124} At optimized conditions between the donor-acceptor interfacial area in bulk can phase separate into the desired nanoscale architecture with an interpenetrating network and appropriate domain size resulting in efficient charge collection, which is essentially important for BJH PSCs.^{51,125}

The active layer materials are important for device performance, much effort has also been directed at improving overall device structures and interfacial materials.¹²⁶ Besides the synthesis of photoactive materials, cathode interlayer material (CIM) modification is also essential for enhancing device performance. By placing a CIM between the active layer and the metal cathode, the work function (WF) of the metal electrode will be aligning the energy levels of the electrode and the active layer.

The most promising n-type metal compound for the metal cathode is ZnO due to its electron mobility, stability, and solution processability. However, the drawback of ZnO is the terminal hydroxy group in addition to anion vacancy sites, obtained through the low-temperature annealing process, which are known to act as electron traps and recombination centers. They can affect the interfacial properties between the metal oxide and organic active

layers, and thus, result in severe recombination losses and energy level mismatch^{127–130}

The intrinsic limitation of mismatched energy levels and unbalanced carrier mobility can be conquered by interlayer modification^{131,132} The CIM can alleviate the interfacial energy barriers and facilitate the charge transporting/collection capability when holes are collected at the anode and electrons are extracted at the cathode.⁶⁰ Appropriate materials could efficiently hamper the recombination of charges and lower the contact resistance at the active layer/electrode interface, which leads to enhance hole/electron extraction. As a result, the parameter for enhancing power conversion efficiency (PCE) such as the short-circuit current (J_{SC}), open-circuit voltage V_{OC} and fill factor FF can be selectively or even simultaneously enhanced in PSC devices.^{60,133}

The conjugated polymer electrolytes (CPEs) which comprise conjugated compounds in the main chain and polar ionic compounds in the side group are used as cathode interlayer material in PSCs to improve the PCE. The conjugated main chains yield typical organic semiconducting properties such as intra-chain and/or inter-chain energy transfer, large optical densities, and fluorescence resonance transfer.¹³⁴

The polar ionic group that makes CPEs soluble in polar solvents such as dimethylsulfoxide (DMSO), dimethyl-formamide (DMF), and methanol (MeOH), and their compensating ions can migrate under external electric fields.¹³⁴ This allows a formation of an interfacial dipole at the cathode interface and improves the built-in electrical field.^{64,65} The favoring intimate contact with both the hydrophobic organic active layer and hydrophilic electrode alcohol-soluble fabrication without intermixing with the halogenated solvent processed active layer.^{62,63} An ideal CIM would lower the electrode WF, have solubility properties orthogonal to those of the photoactive layer, exhibit good film-forming properties (wettability/uniformity), transport electrons selectivity, possess large electron affinity, and exhibit long-term stability.^{135,136}

In this paper, we synthesize and modify the side chain of poly[(9,9-bis(3'-(N,N-dimethylamino)propyl)-2,7-fluorene)-alt-2,7-(9,9-dihexylfluorene)] (PFN) to investigate the effect of different chain functionality as CIM on the photovoltaic properties. As shown in Figure 20, the CPEs with different side chains are poly [(9,9-bis(3'-(N-ethyl-N- dimethylamino) propyl)-dibromide-2,7-fluorene)-alt-2,7-(9,9-dihexylfluorene)], denote as PFN salt and poly[(9,9-bis(3'-(N-hydroxyethyl-N-dimethylamino) propyl) dibromide-2,7-fluorene)-alt-2,7-(9,9dihexyl-fluorene)]), denote as PFN-OH salt. PFN salt and PFN-OH salt were synthesized by quaternization with

bromoethane and bromoethanol. By applying the CPE as the CIM with quaternary ammonium bromide salt in the inverted device structure (ITO/ZnO/interlayer/PTB7-Th: PC71BM/MoO₃/Ag), we found that the PFN-OH salt category offers the highest PCEs compared with the PFN salt and PFN precursor. The PCE of the devices with quaternized OH-salt reached up to 9.62% due to the synergy effect of hydrogen bonding between the ZnO layer and hydroxyl group in the quaternary salt.

The presence of a quaternary ammonium salt containing CIM affects the J_{SC} in solar cells. The synergy effect of the CIM makes it possible to be embedded in the ZnO layer. This is due to the formation of a favorable interface dipole between the ZnO layer and the quaternary ammonium salt layer. The fact that electron collection ability from the active layer to the electron transport layer is improved by reducing the energy barrier at the interface.^{74,137}

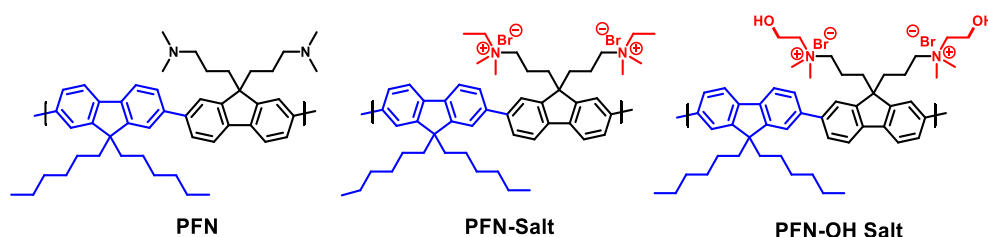


Figure 50. Chemical structure of the interlayer

2. Result and Discussion

1.) Optical and electrochemical properties

The PFN salt and PFN-OH salt are soluble in alcohol, while the PFN precursor needs the assistance of a small amount of acetic acid. The PFN salt and PFN-OH salt are insoluble in chloroform, chlorobenzene, and dichlorobenzene, which is suitable for multilayer device fabrication.⁸² UV-vis spectroscopy was performed to investigate the optical properties of the CIM. The PFN precursor was prepared by dissolving in methanol with the molar ratio of acetic acid to polymer 6:1, while the PFN salt and PFN-OH salt solutions were prepared in methanol only. Figure 21 shows the absorption spectra of the thin film of the polymers based on PFN precursor, and the optical properties are listed in Table 4.

The PFN film exhibited a maximum absorption wavelength band showed at 358 nm due to the π - π^* transition of the polymer backbone.¹³⁸ The maximum absorption wavelength of PFN salt and PFN-OH salt appeared at 400, and 399 nm, respectively, which are red-shifted than PFN due to the interchain interaction of PFN being more robust than that of PFN salt and PFN-OH salt.¹³⁹ Their aggregation properties mainly cause a more vital interchain interaction in the polyelectrolyte.¹⁴⁰

Table 9. Optical and electrochemical properties of PFN, PFN salt, PFN-OH salt

Sample	λ_{max}^a (nm)	λ_{edge}^b (nm)	HOMO ^c (eV)	LUMO (eV)
PFN	358	421	-5.51	-2.13
PFN salt	400	433	-	-
PFN-OH salt	399	433	-	-

^a Absorption maximum

^b Optical bandgap was obtained from the onset wavelength (λ edge) of the film

^c Obtained from oxidation and reduction onset potential of the cyclic voltammogram

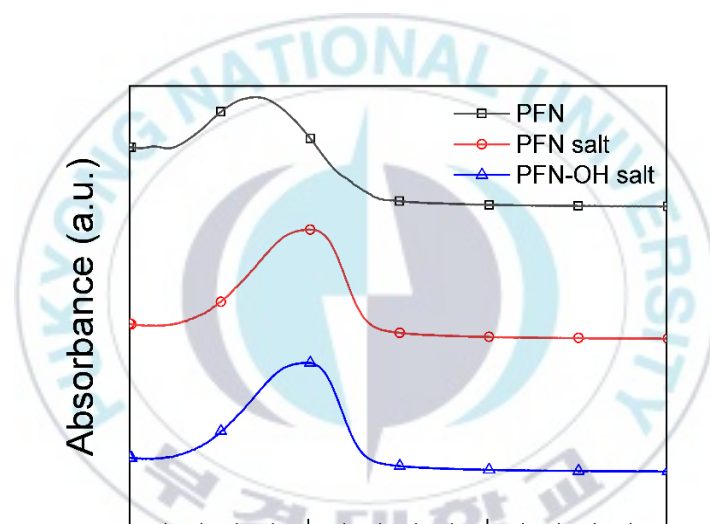


Figure 51. UV-Vis spectra of PFN, PFN salt, PFN-OH salt.

Based on the onset reduction potential in cyclic voltammograms (CVs). The LUMO energy level of PFN is estimated to be -2.13 eV and the HOMO energy level of PFN to be -5.51 eV. The CVs were calibrated using the ferrocene/ferrocenium (Fc/Fc⁺) redox couple as the reference. (Figure 22)

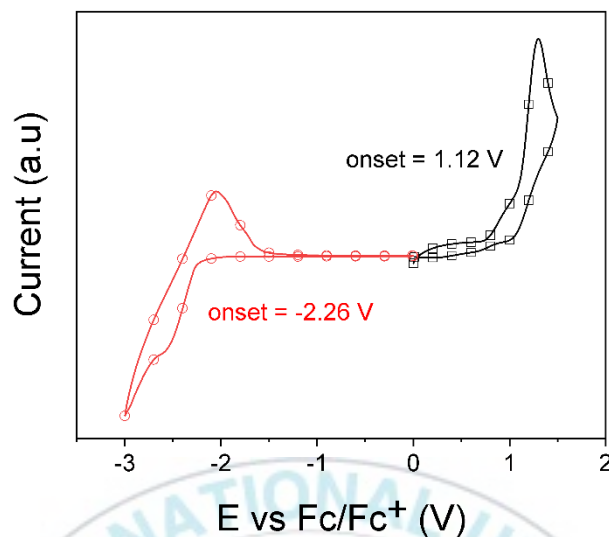


Figure 52. Figure 3. Cyclic voltammograms of PFN.

2.) Theoretical calculation of the polymers

In identifying the bond interaction of interlayers in PSCs, we point out that predicting modeling this system at the molecular scale requires density functional theory (DFT). The theoretical calculation explores the electronic properties and gives a preliminary insight into the geometric structures and dipolar properties of the CIM. The density functional theory (DFT) calculation was carried out with simple molecular geometries on the Gaussian suite of programs (Gaussian 09).⁷⁸ The optimized geometries of the interlayer materials with dihedral angles and dipole moments are depicted in figure 23. Dihedral angles are defined as the deviation from 180° of the torsional angles between the adjacent fluorene units around the bond that connects them. A

small dihedral angle (i.e., planar structure) promotes the delocalization of the π -electron system. Similarly, the bond length alternation parameter provides a quantitative measure of the homogeneity in the distribution of π electrons over the bonds (Peierls distortion) by comparing the length of consecutive bonds along the chain. An enhancement in the electronic delocalization tends to equalize the bond lengths, reducing the bond length alternation.⁷⁹

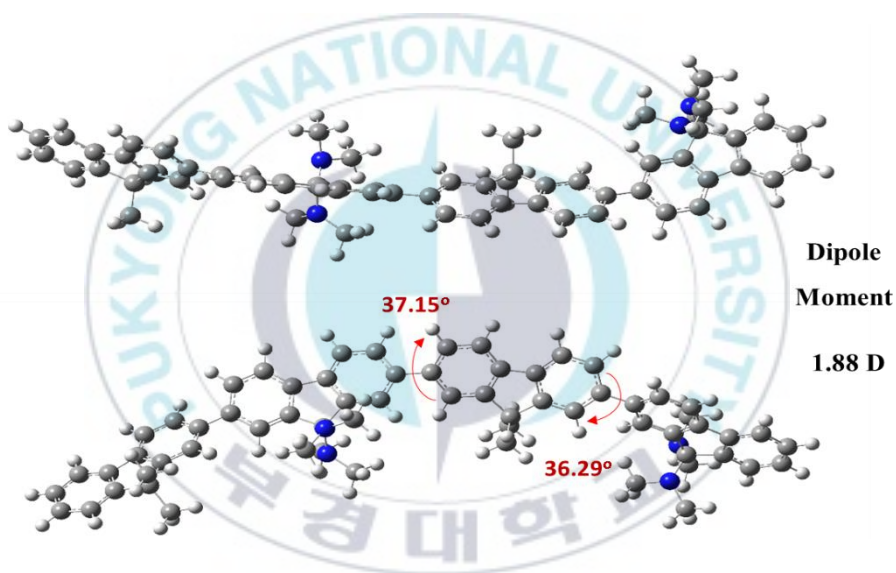


Figure 53. DFT-optimized geometries and dipolar properties of PFN calculated by B3LYP/6-31G (d) level.

As shown in Figure 23, the polar groups situated as the side group on the fluorene unit in PFN lead to 1.07 D. The PFN shows geometry with the dihedral angles between the fluorene ring in the backbone are 37.78° and 37.63°. This calculation indicates that the combination of two fluorenes

groups increases the steric hindrance and leads to twisted conformation permanent dipole moment. The frontier molecular orbitals of the two repeating units with theoretical HOMO/LUMO energy levels are shown in Figure 24. The calculated HOMO/LUMO energy levels exhibit similar trends in the UV-Vis and CV experiments. The HOMO/LUMO of PFN is delocalized in the fluorene backbone.



Figure 54. Frontier molecular orbitals of two-repeating unit models with HOMO/LUMO energy levels calculated at the B3LYP/6-31G** level for PFN

3.) Investigation of the ZnO surface covered with CPEs

The ZnO/CIM surface properties were investigated by the water contact angle measurement (Figure 25). The water contact angle of the ZnO/PFN precursor was higher than the ZnO/PFN salt and ZnO/PFN-OH salt, which resulted from the hydrophobic properties of PFN. The water contact angle of the ZnO surface with PFN, PFN salt, and PFN-OH salt were 60.8°, 49.7°, and 44.1°, respectively, which are increased from the value of pristine ZnO (28.6°). The quaternized PFN showed a lower water contact angle due to the

increment of hydrophilicity of PFN-salt and the formation of hydrogen bonding of PFN-OH salt. In general, the small water contact angle indicates the suitable wetting property, and the advantage of the PFN-modified interlayers for use in solar cells.

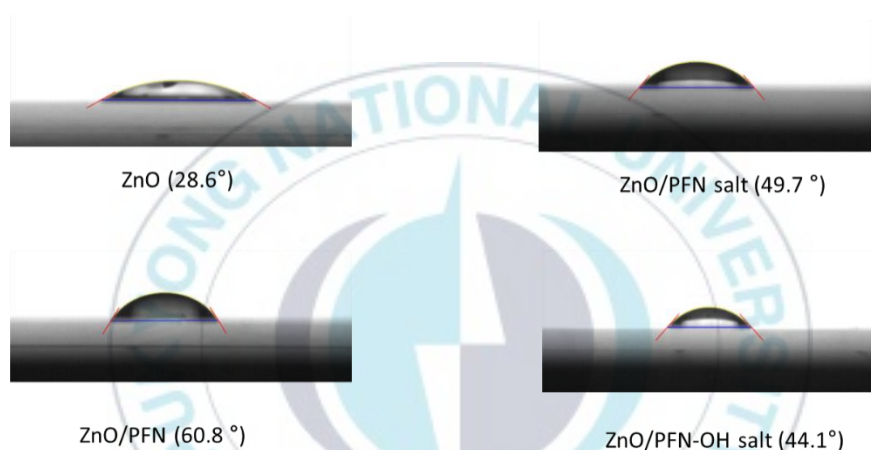


Figure 55. Static water contact angle data of ZnO, ZnO/PFN, ZnO/PFN-salt, and ZnO/PFN-OH salt.

To investigate the influence of interlayer on the work function of ZnO, Kelvin Probe Microscopy (KPM) measurements were performed. Figure 26 showed the work function of ZnO with PFN, PFN salt, and PFN-OH salt. The work function (WF) of ZnO with PFN, PFN salt, and PFN-OH salt -4.17, -4.14, and -4.26 eV, respectively. The WF data of ZnO with interlayers were higher than that of ZnO without interlayers (-4.4 eV). The mechanism behind the improvement of the PCE has generally attributed to the WF change at the

surface of ZnO by the formation of interface dipole⁸⁸, which can be tuned by introducing the interlayer, i.e., transition from a Schottky to an Ohmic contact. Thus, the reduced barrier height at the ZnO surface might improve the charge collection capability.^{65,89,90}

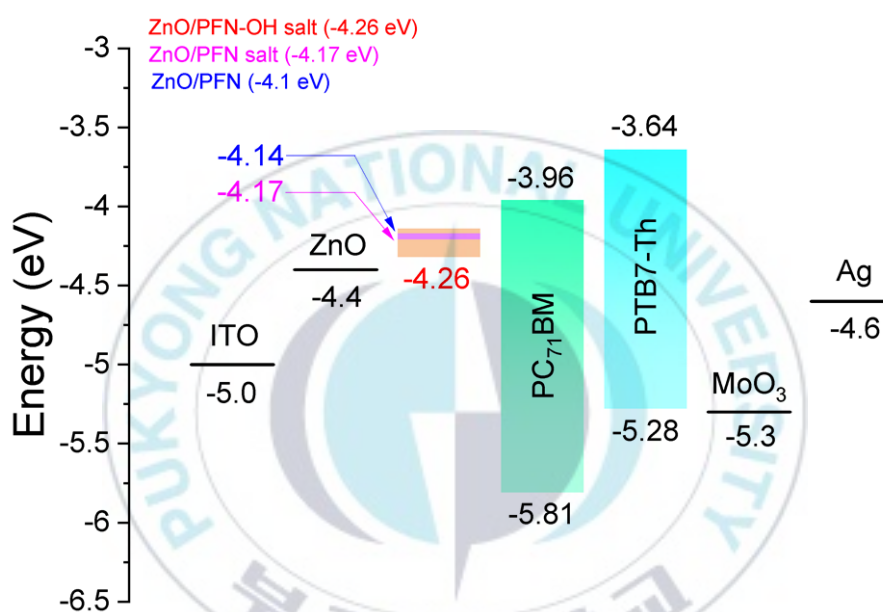


Figure 56. Energy level diagrams of ZnO/PFN, ZnO/PFN salt, and ZnO/PFN-OH salt.

As for polymer salts, a higher interface dipole can be expected because the magnitude of the dipole moment of polymer salts could be higher than those of neutral polymer categories. PFN can be dissolved in alcohol in the presence of a small amount of acetic acid due to the weak interaction between the nitrogen atoms in the side chain and the acetic acid. Neutral amine groups

in PFN polymer are primarily physisorbed onto the ZnO surface.^{91,92} The reduction of the work function and energy level adjustment is a synergistic effect from the PFN intrinsic molecular dipole (μ_{MD}) and the interfacial dipole (μ_{ID}) formed at the interface between the modifier molecules and electrode surface.⁹³ The contribution of μ_{ID} is attributed to partial electron transfer from the amine-containing molecules to the electrode surface⁹⁴. It has been demonstrated that the amine and hydroxyl groups can spontaneously adsorb on the ZnO surface resulting in dipolar polymerization.⁹⁵ The magnitude of the dipole moment of PFN-OH salts is higher than that of polymer salts due to polar -OH groups generating a synergy effect in the magnitude of dipole moment. Thus, the magnitude of interface dipole for PFN-OH salts > PFN salts > neutral PFN.

The trend of the J_{SC} follow the trend of the WF of ZnO. Generally, the work function difference in the charge transporting layer is not the main factor affecting the built-in potential and the V_{OC} in the case of Fermi-level pinning.⁹⁶ J. Park et al. also studied the spontaneous organization of side chains on CPE.⁹⁷ Based on our previous study, we discovered that the quaternized side chain of CPE affects the WF and wetting ability by the spontaneous arrangement of the side chain.^{98,99} In the stacking devices architecture, when we introduce an interlayer between ZnO and the active layer, the ionic groups on the CPE backbone are directed away from the surface of the active layer.

Simultaneously, the side chains pointed out toward the ZnO layer owing to the spontaneous re-organization. The more significant number of the accumulated ionic group at the CPE leads to an Ohmic contact and better wettability on the active layer.

4.) Photovoltaic Properties

The photovoltaic properties of the device with CIMs were investigated and studied. The structure of ITO/ZnO/CIM/PTB7-Th:PC71BM/MoO₃/Ag (figure 27a). The current density-voltage ($J - V$) curves of the PSCs with PFN as the interlayer under illumination (inset: under the dark condition) showed in figure 27b. In addition, the photovoltaic parameters were summarized in table 5. The devices with CIM showed higher PCEs than that of the device based on pristine ZnO.

This indicated that PFNs as CIMs are the potential materials for interfacial modification to enhance the device's performance. The PCEs of the PSCs with the neutral PFN, PFN-salt, and PFN-OH salt, were 8.80, 9.18, and 9.62%, respectively, which are higher than that of the device without interlayer. The improvement in the performance of neutral PFN category devices mainly arises from the enhancement of the J_{sc} and FF , simultaneously. Device-based on PFN-OH salt showed significantly improved PCE. This is due to the side chain functionality enhancing the

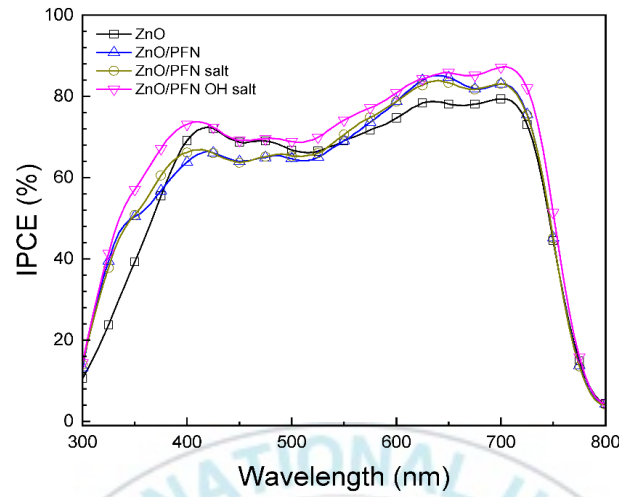


Figure 57. IPCE graph of (a) neutral polymer category, (b) salt polymer category, (c) OH salt polymer category.

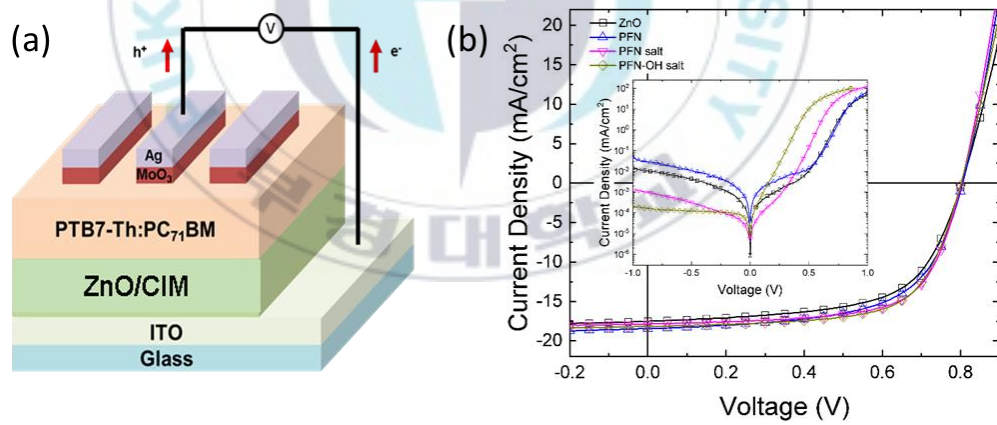


Figure 58. (a) device architecture and (b). J - V curves of PFN, PFN salt, PFN-OH salt

device performance. The J_{SC} values obtained from the Incident photon-to-current efficiency (IPCE) curves (Figure 27) were in good agreement with the values obtained under 1.0 sun illumination.

The devices without interlayer exhibited the lowest performance where the combination of low open-circuit voltage (V_{oc}), short-circuit current (J_{sc}), and the fill factor (FF) resulted in a PCE of 8.74%. The mismatch of the WF between the active and electrode layers and low charge extraction due to high contact resistance occurred in the device based on pristine ZnO^{65,89,141}.

We evaluated the relationship between the photocurrent density (J_{ph}) and effective voltage (V_{eff}) to understand the charge transport and collection properties of the devices with and without interlayers. Here, the J_{ph} and V_{eff} were defined by J_L (measured current density under illumination) – J_D (measured current density in dark conditions) and V_0 (voltage at $J_{ph} = 0$) – V_a (applied voltage), respectively. The $\log(J_{ph})$ vs. $\log(V_{eff})$ showed a linear relationship between a low V_{eff} range and start to saturate at a high V_{eff} value region. The V_{eff} values of the devices in the saturated photocurrent regime (V_{sat}). The V_{sat} values of the devices based on PFN, PFN salt, and PFN-OH salt were 0.55, 0.35, and 0.26 V, which are smaller than that of the device based on pristine ZnO (0.56 V). The trend of V_{sat} well agreed with the change of the J_{sc} and PCE of the devices because a smaller V_{sat} indicated a faster transition from the space-charge-limited regime to the saturation regime. In the other word V_{sat} means the low energy barrier in the devices.

Table 10. The performances of the PFN polymer series show the best PCE. The averages (20 devices are averaged) are summarized in parentheses

	J_{sc}^a (mA/cm ²)	$J_{sc, cal}^b$ (mA/cm ²)	V_{oc} (V)	FF (%)	PCE (%)	R_s^b (Ω cm ²)	R_{sh}^c (Ω cm ²)
ZnO	17.5 (17.4)	17.5	0.80 (0.80)	62.2 (62.1)	8.74 (8.71)	5.26	552
ZnO/PFN	18.16 (18.1)	18.1	0.81 (0.81)	60.2 (59.9)	8.80 (8.70)	4.04	911
ZnO/PFN salt	18.5 (18.4)	18.5	0.81 (0.80)	61.8 (60.8)	9.18 (8.95)	4.07	505
ZnO/PFN-OH salt	17.9 (17.8)	17.9	0.80 (0.80)	67.4 (66.0)	9.62 (9.47)	4.18	899

^a calculated from the IPCE curves, ^b series, and ^c shunt resistance under illumination

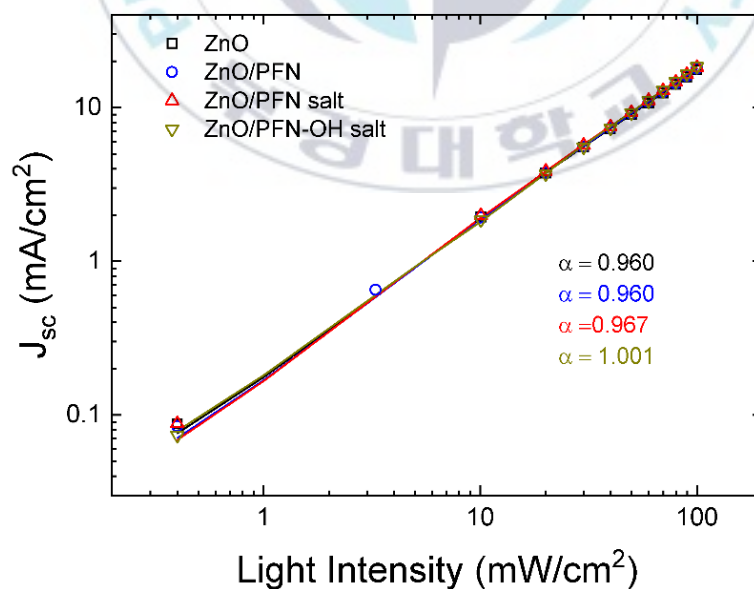


Figure 59. Dependence of J_{sc} on light intensity of PFN, PFN salt, and PFN-OH salt

The saturation current density (J_{sat}) can be correlated with the maximum exciton generation rate (G_{max}), exciton dissociation probability, and carrier transport and collection probability at high V_{eff} . The G_{max} depends on the absorption of light on the active layer and was determined by $J_{ph}/q \cdot L$, where q is the electron charge, and L is the thickness of the active layer.¹⁴² The carrier transporting and collecting probability at the point of saturated current was estimated from the ratio of J_{ph} / J_{sat} at any V_{eff} . The G_{max} under the J_{sat} condition of the devices based on pristine ZnO was $1.57 \times 10^{28} \text{ m}^{-3} \text{ s}^{-1}$ and ZnO/PFN interlayer for the PFN, PFN salt, and PFN-OH salt were 1.56, 1.62, and $1.62 \times 10^{28} \text{ m}^{-3} \text{ s}^{-1}$, respectively.

The J_{sat} is limited by the carrier transport and collection, when all the photo-generated excitons are dissociated into free charge carriers at high V_{eff} .¹⁴³ The point of V_{eff} reached at saturated photocurrent, the G_{max} and the carrier transporting and collecting probability are strongly related to the trend of the J_{sc} values. These values reveal that the CPEs exhibited decreased charge recombination and increased charge collection capability at the interfaces of cathode layers.

The dependence of J_{sc} and V_{oc} on light intensity (P_{light}) was measured to investigate the charge carrier recombination, which has been shown via J_{sc} vs. P_{light} and V_{oc} vs. P_{light} curves and the slope of those curves.

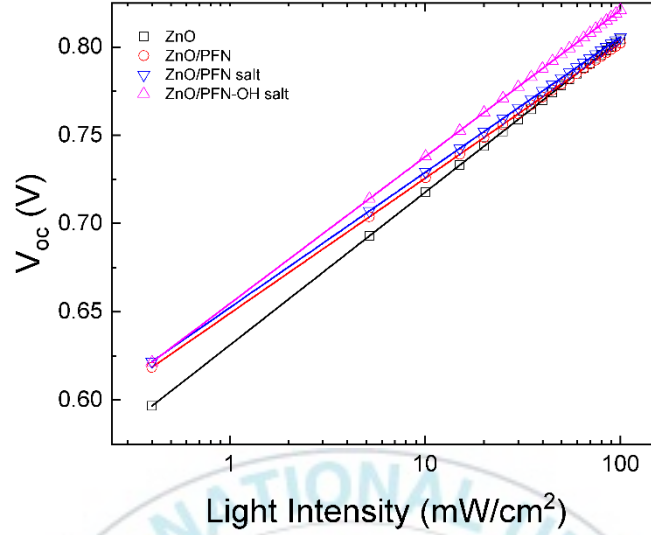


Figure 60. The dependence of V_{oc} on the light intensity of PFN, PFN salt, and PFN-OH salt

The relationship between J_{SC} and P_{light} is explained by the equation of $J_{SC} \propto (P_{light})^\alpha$ and the value of α indicates the balance of electron-hole mobility. When α is close to 1, the device exhibited bimolecular recombination under short-circuit conditions. As shown in Figure 29, α of the device without interlayer exhibited 0.960. The α values of the devices with PFN, PFN salt, and PFN-BT OH salts were 0.960, 0.967, 1.001, and 0.962, respectively.

The electron mobility of the devices indicates that the devices exhibited slight bimolecular recombination because of the decreased space charge at the interfaces. The value of α from our measurement indicates that bimolecular recombination is suppressed in PSCs with CPE interlayers. In

BHJ-type solar cells, bimolecular recombination occurs mainly at the donor-acceptor interfaces of the active layer and the interlayers. Devices suppress recombination because of the decreased space charge at the interface¹⁵. The trap-assisted recombination is explained by the relationship between V_{OC} and intensity (P_{light}). The slope of the V_{OC} vs P_{light} curve has a value of 1 when the band-to-band (Langevin) recombination is superior to the trap-assisted recombination. When the devices have only trap-assisted recombination, the s value is 2.

The relationship is explained by this equation $V_{OC} \propto \frac{skT}{q \ln(P_{light})}$, where k , T , q and P_{light} are the Boltzmann constant, temperature in Kelvin, electron charge, and illumination intensity, respectively. The slopes of the V_{OC} vs. P_{light} curves with and without the CIM of the devices are shown in Figure 30. Devices without the CIM exhibited an s value of 1.46. The s values of the devices based on PFN, PFN salt, and PFN-OH sat were 1.290, 1.294, and 1.410, respectively. These results prove the effectiveness of CPEs in reducing the number of traps. The changes in the s values of devices correspond with the trend shown by the PCEs of PSCs and follow the FF trend.

To investigate the carrier transport and recombination mechanism we performed electronic impedance spectroscopy (EIS). As shown in Figure 31

were fitted to estimate the recombination resistance (R_{rec}) at 0 bias. The efficient charge collection was implied by transport resistance, which is smaller than recombination resistance R_{rec} .

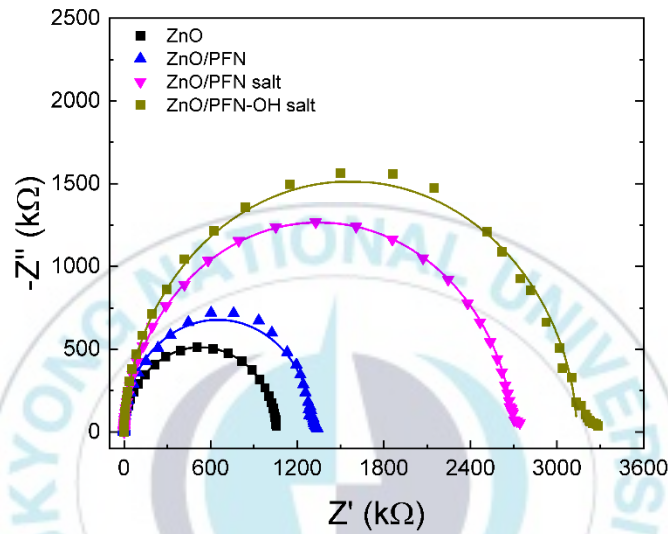


Figure 61. Impedance spectra of PFN, PFN salt, and PFN-OH salt

The EIS spectra followed the Gerischer impedance model in an intense recombination situation. The absence of a transmission line indicates that the devices experience strong recombination. In the Nyquist plots, the respective electrochemical steps with different time constants were represented by the semicircles. The length between the intercepts at the real axis corresponds to the charge transfer resistance of the device.^{107–114} The larger size of the EIS semicircle shows a greater R_{rec} . The higher R_{rec} values are related to the charge extraction capability at the ZnO interfaces. The R_{rec} of the device based on PFN, PFN salt, and PFN-OH salt

were 1300, 2703, and 3141 k Ω , respectively. The size of the semicircle is increased, leading to increased R_{rec} . The magnitude of R_{rec} of the device was in the order of neutral PFN < PFN salt < PFN-OH salt. This indicates that the lowest reduced interfacial recombination has a good agreement with the R_{sh} and FF of the PSCs.

3. Conclusion

We have synthesized and characterized cathode interlayer material (CIM) that contain neutral polymer (PFN), polymer salt (PFN salt), and polymer-OH salt (PFN-OH salt). The CIM was introduced in an inverted PSCs with a structure: ITO/ZnO/CIM/PTB7-Th: PC71BM/MoO₃/Ag. The highest PCE of 9.62% was achieved by PFN-OH salt. Combined with surface contact angle measurement, optical simulation, and photovoltaic characterization of the solar cells, we found that the PCEs of the device based on CPEs depend on the side chain functionality. The quaternized salt and OH salt induces a larger interface dipole and spontaneous organization. This synergy effect from the backbone and side chain functionality are the major significant contribution to enhancing the PCEs. Main contribution in enhancing the PCE resulted from the improving the J_{SC} . This is due to the reduction of the energy offset at the cathode interface.

References

- (1) Sharma, S.; Jain, K. K.; Sharma, A. Solar Cells: In Research and Applications—A Review. *Mater. Sci. Appl.* **2015**, *06* (12), 1145–1155. <https://doi.org/10.4236/msa.2015.612113>.
- (2) Chopra, K. L.; Paulson, P. D.; Dutta, V. Solar Cell Current Scenario and Future Trends. *Prog. Photovoltaics Res. Appl.* **2004**, *12* (2–3), 69–92.
- (3) Muñoz, D.; Ozanne, A. S.; Harrison, S.; Danel, A.; Souche, F.; Denis, C.; Favier, A.; Desrues, T.; De Nicolás, S. M.; Nguyen, N.; Hickel, P. E.; Mur, P.; Salvétat, T.; Moriceau, H.; Le-Tiec, Y.; Kang, M. S.; Kim, K. M.; Janin, R.; Pesenti, C.; Blin, D.; Nolan, T.; Kashkoush, I.; Ribeyron, P. J. Towards High Efficiency on Full Wafer A-Si:H/c-Si Heterojunction Solar Cells: 19.6% ON 148cm². *Conf. Rec. IEEE Photovolt. Spec. Conf.* **2010**, 39–43. <https://doi.org/10.1109/PVSC.2010.5614179>.
- (4) Dou, L.; You, J.; Hong, Z.; Xu, Z.; Li, G.; Street, R. A.; Yang, Y. 25th Anniversary Article: A Decade of Organic/Polymeric Photovoltaic Research. *Adv. Mater.* **2013**, *25* (46), 6642–6671. <https://doi.org/10.1002/adma.201302563>.
- (5) Forrest, S. R. The Limits to Organic Photovoltaic Cell Efficiency. *MRS Bull.* **2005**, *30* (1), 28–32. <https://doi.org/10.1557/mrs2005.5>.

- (6) Green, M. A.; Emery, K.; Hishikawa, Y.; Warta, W.; Dunlop, E. D. Solar Cell Efficiency Tables (Version 39). *Prog. Photovoltaics Res. Appl.* **2012**, *20* (1), 12–20.
<https://doi.org/https://doi.org/10.1002/pip.2163>.
- (7) Günes, S.; Neugebauer, H.; Sariciftci, N. S. Conjugated Polymer-Based Organic Solar Cells. *Chem. Rev.* **2007**, *107* (4), 1324–1338.
<https://doi.org/10.1021/cr050149z>.
- (8) Reynolds, J. R.; Thompson, B. C.; Skotheim, T. A. *Conjugated Polymers*, 4th ed.; Reynolds, J. R., Thompson, B. C., Skotheim, T. A., Eds.; CRC Press, 2019. <https://doi.org/10.1201/9780429190520>.
- (9) Heeger, A. J. 25th Anniversary Article: Bulk Heterojunction Solar Cells: Understanding the Mechanism of Operation. *Adv. Mater.* **2014**, *26* (1), 10–28. <https://doi.org/10.1002/adma.201304373>.
- (10) McCulloch, I.; Heeney, M.; Bailey, C.; Genevicius, K.; MacDonald, I.; Shkunov, M.; Sparrowe, D.; Tierney, S.; Wagner, R.; Zhang, W.; Chabinyc, M. L.; Kline, R. J.; McGehee, M. D.; Toney, M. F. Liquid-Crystalline Semiconducting Polymers with High Charge-Carrier Mobility. *Nat. Mater.* **2006**, *5* (4), 328–333.
<https://doi.org/10.1038/nmat1612>.

- (11) Zaumseil, J.; Sirringhaus, H. Electron and Ambipolar Transport in Organic Field-Effect Transistors. *Chem. Rev.* **2007**, *107* (4), 1296–1323. <https://doi.org/10.1021/cr0501543>.
- (12) Pope, M.; Swenberg, C. E. *Electronic Processes in Organic Crystals and Polymers*, 2nd ed.; Oxford University Press, 1999.
- (13) Wannier, G. H. The Structure of Electronic Excitation Levels in Insulating Crystals. *Phys. Rev.* **1937**, *52* (3), 191–197. <https://doi.org/10.1103/PhysRev.52.191>.
- (14) Nunzi, J. M. Organic Photovoltaic Materials and Devices. *Comptes Rendus Phys.* **2002**, *3* (4), 523–542. [https://doi.org/10.1016/S1631-0705\(02\)01335-X](https://doi.org/10.1016/S1631-0705(02)01335-X).
- (15) Gusain, A.; Faria, R. M.; Miranda, P. B. Polymer Solar Cells-Interfacial Processes Related to Performance Issues. *Front. Chem.* **2019**, *7* (February), 61. <https://doi.org/10.3389/fchem.2019.00061>.
- (16) Li, W.; Albrecht, S.; Yang, L.; Roland, S.; R. Tumbleston, J.; McAfee, T.; Yan, L.; Allison Kelly, M.; Ade, H.; Neher, D.; You, W. Mobility-Controlled Performance of Thick Solar Cells Based on Fluorinated Copolymers. *J. Am. Chem. Soc.* **2014**, *136* (44), 15566–15576. <https://doi.org/10.1021/ja5067724>.

- (17) Seo, J. H.; Jin, Y.; Brzezinski, J. Z.; Walker, B.; Nguyen, T. Q. Exciton Binding Energies in Conjugated Polyelectrolyte Films. *ChemPhysChem* **2009**, *10* (7), 1023–1027. <https://doi.org/10.1002/cphc.200800751>.
- (18) Petritsch, K. Organic Solar Cell Architectures. *Tech. Univ. Graz Austria, Dr. Thesis* **2000**, *1* (July), 159. <https://doi.org/10.1161/01.RES.0000127175.21818.C2>.
- (19) Krebs, F. C.; Gevorgyan, S. A.; Alstrup, J. A Roll-to-Roll Process to Flexible Polymer Solar Cells: Model Studies, Manufacture and Operational Stability Studies. *J. Mater. Chem.* **2009**, *19* (30), 5442. <https://doi.org/10.1039/b823001c>.
- (20) Jørgensen, M.; Norrman, K.; Gevorgyan, S. A.; Tromholt, T.; Andreasen, B.; Krebs, F. C. Stability of Polymer Solar Cells. *Adv. Mater.* **2012**, *24* (5), 580–612. <https://doi.org/10.1002/adma.201104187>.
- (21) Wang, K.; Liu, C.; Meng, T.; Yi, C.; Gong, X. Inverted Organic Photovoltaic Cells. *Chem. Soc. Rev.* **2016**, *45* (10), 2937–2975. <https://doi.org/10.1039/C5CS00831J>.
- (22) Wang, Y.; Suna, A. Fullerenes in Photoconductive Polymers. Charge Generation and Charge Transport. *J. Phys. Chem. B* **1997**, *101* (29), 5627–5638. <https://doi.org/10.1021/jp964019t>.
- (23) Xie, C.; Chen, L.; Chen, Y. Electrostatic Self-Assembled Metal Oxide/Conjugated Polyelectrolytes as Electron-Transporting Layers for

- Inverted Solar Cells with High Efficiency. *J. Phys. Chem. C* **2013**, *117* (47), 24804–24814. <https://doi.org/10.1021/jp405176u>.
- (24) Thompson, B. J.; York, N.
OPV__mechanism__materials__and_devices; 2005.
- (25) Bao, J.; Liang, X. X. Surface and Interface Phonon-Polaritons in Bilayer Systems of Polar Ternary Mixed Crystals. *J. Appl. Phys.* **2008**, *104* (3), 033545. <https://doi.org/10.1063/1.2965190>.
- (26) Campoy-Quiles, M.; Ferenczi, T.; Agostinelli, T.; Etchegoin, P. G.; Kim, Y.; Anthopoulos, T. D.; Stavrinou, P. N.; Bradley, D. D. C.; Nelson, J. Morphology Evolution via Self-Organization and Lateral and Vertical Diffusion in Polymer:Fullerene Solar Cell Blends. *Nat. Mater.* **2008**, *7* (2), 158–164. <https://doi.org/10.1038/nmat2102>.
- (27) Nelson, J. Polymer:Fullerene Bulk Heterojunction Solar Cells. *Mater. Today* **2011**, *14* (10), 462–470. [https://doi.org/10.1016/S1369-7021\(11\)70210-3](https://doi.org/10.1016/S1369-7021(11)70210-3).
- (28) Irwin, M. D.; Buchholz, D. B.; Hains, A. W.; Chang, R. P. H.; Marks, T. J. P-Type Semiconducting Nickel Oxide as an Efficiency-Enhancing Anode Interfacial Layer in Polymer Bulk-Heterojunction Solar Cells. *Proc. Natl. Acad. Sci.* **2008**, *105* (8), 2783–2787. <https://doi.org/10.1073/pnas.0711990105>.

- (29) Shrotriya, V.; Li, G.; Yao, Y.; Chu, C.-W.; Yang, Y. Transition Metal Oxides as the Buffer Layer for Polymer Photovoltaic Cells. *Appl. Phys. Lett.* **2006**, 88 (7), 73508. <https://doi.org/10.1063/1.2174093>.
- (30) Steim, R.; Choulis, S. A.; Schilinsky, P.; Brabec, C. J. Interface Modification for Highly Efficient Organic Photovoltaics. *Appl. Phys. Lett.* **2008**, 92 (9), 93303. <https://doi.org/10.1063/1.2885724>.
- (31) White, M. S.; Olson, D. C.; Shaheen, S. E.; Kopidakis, N.; Ginley, D. S. Inverted Bulk-Heterojunction Organic Photovoltaic Device Using a Solution-Derived ZnO Underlayer. *Appl. Phys. Lett.* **2006**, 89 (14), 143517. <https://doi.org/10.1063/1.2359579>.
- (32) Seo, J. H.; Gutacker, A.; Sun, Y.; Wu, H.; Huang, F.; Cao, Y.; Scherf, U.; Heeger, A. J.; Bazan, G. C. Improved High-Efficiency Organic Solar Cells via Incorporation of a Conjugated Polyelectrolyte Interlayer. *J. Am. Chem. Soc.* **2011**, 133 (22), 8416–8419. <https://doi.org/10.1021/ja2037673>.
- (33) Na, S.-I.; Kim, S.-S.; Jo, J.; Kim, D.-Y. Efficient and Flexible ITO-Free Organic Solar Cells Using Highly Conductive Polymer Anodes. *Adv. Mater.* **2008**, 20 (21), 4061–4067. [https://doi.org/https://doi.org/10.1002/adma.200800338](https://doi.org/10.1002/adma.200800338).
- (34) Kim, S.; Yim, J.; Wang, X.; Bradley, D. D. C.; Lee, S.; deMello, J. C. Spin- and Spray-Deposited Single-Walled Carbon-Nanotube Electrodes

- for Organic Solar Cells. *Adv. Funct. Mater.* **2010**, *20* (14), 2310–2316.
<https://doi.org/https://doi.org/10.1002/adfm.200902369>.
- (35) Kim, E.-H.; Yang, C.-W.; Park, J.-W. The Crystallinity and Mechanical Properties of Indium Tin Oxide Coatings on Polymer Substrates. *J. Appl. Phys.* **2011**, *109* (4), 043511–043511–043518.
<https://doi.org/10.1063/1.3556452>.
- (36) Gu, Y.; Zhu, Z.; Song, J.; Zeng, H. Triangle-, Tripod-, and Tetrapod-Branched ITO Nanocrystals for Anisotropic Infrared Plasmonics. *Nanoscale* **2017**, *9* (48), 19374–19383.
<https://doi.org/10.1039/C7NR07895A>.
- (37) Kim, K.-B.; Tak, Y.-H.; Han, Y.-S.; Baik, K.-H.; Yoon, M.-H.; Lee, M.-H. Relationship between Surface Roughness of Indium Tin Oxide and Leakage Current of Organic Light-Emitting Diode. *Jpn. J. Appl. Phys.* **2003**, *42* (Part 2, No. 4B), L438–L440.
<https://doi.org/10.1143/JJAP.42.L438>.
- (38) Kirchartz, T. Influence of Diffusion on Space-Charge-Limited Current Measurements in Organic Semiconductors. *Beilstein J. Nanotechnol.* **2013**, *4*, 180–188. <https://doi.org/10.3762/bjnano.4.18>.
- (39) de Jong, M. P.; van IJendoorn, L. J.; de Voigt, M. J. A. Stability of the Interface between Indium-Tin-Oxide and Poly(3,4-Ethylenedioxythiophene)/Poly(Styrenesulfonate) in Polymer Light-

- Emitting Diodes. *Appl. Phys. Lett.* **2000**, 77 (14), 2255–2257.
<https://doi.org/10.1063/1.1315344>.
- (40) Li, Z.; Li, S.; Zhang, Z.; Zhang, X.; Li, J.; Liu, C.; Shen, L.; Guo, W.; Ruan, S. Enhanced Electron Extraction Capability of Polymer Solar Cells via Modifying the Cathode Buffer Layer with Inorganic Quantum Dots. *Phys. Chem. Chem. Phys.* **2016**, 18 (16), 11435–11442.
<https://doi.org/10.1039/C6CP00989A>.
- (41) Crispin, X.; Marciniak, S.; Osikowicz, W.; Zotti, G.; van der Gon, A. W. D.; Louwet, F.; Fahlman, M.; Groenendaal, L.; De Schryver, F.; Salaneck, W. R. Conductivity, Morphology, Interfacial Chemistry, and Stability of Poly(3,4-Ethylene Dioxythiophene)-Poly(Styrene Sulfonate): A Photoelectron Spectroscopy Study. *J. Polym. Sci. Part B Polym. Phys.* **2003**, 41 (21), 2561–2583.
<https://doi.org/10.1002/polb.10659>.
- (42) Yu, T.; Xu, J.; Liu, L.; Ren, Z.; Yang, W.; Yan, S.; Ma, Y. Electrochemically Deposited Interlayer between PEDOT:PSS and Phosphorescent Emitting Layer for Multilayer Solution-Processed Phosphorescent OLEDs. *J. Mater. Chem. C* **2016**, 4 (40), 9509–9515.
<https://doi.org/10.1039/C6TC03039D>.

- (43) Ma, H.; Yip, H. L.; Huang, F.; Jen, A. K. Y. Interface Engineering for Organic Electronics. *Adv. Funct. Mater.* **2010**, *20* (9), 1371–1388. <https://doi.org/10.1002/adfm.200902236>.
- (44) Hu, Z.; Zhong, Z.; Chen, Y.; Sun, C.; Huang, F.; Peng, J.; Wang, J.; Cao, Y. Energy-Level Alignment at the Organic/Electrode Interface in Organic Optoelectronic Devices. *Adv. Funct. Mater.* **2016**, *26* (1), 129–136. <https://doi.org/10.1002/adfm.201503420>.
- (45) Stubhan, T.; Oh, H.; Pinna, L.; Krantz, J.; Litzov, I.; Brabec, C. J. Letter. *Org. Electron.* **2011**, *12* (9), 1539–1543. <https://doi.org/10.1016/j.orgel.2011.05.027>.
- (46) Li, X.; Liu, X.; Zhang, W.; Wang, H. Q.; Fang, J. Fullerene-Free Organic Solar Cells with Efficiency over 12% Based on EDTA-ZnO Hybrid Cathode Interlayer. *Chem. Mater.* **2017**, *29* (10), 4176–4180. <https://doi.org/10.1021/acs.chemmater.7b01615>.
- (47) Xu, X.; Feng, K.; Lee, Y. W.; Woo, H. Y.; Zhang, G.; Peng, Q. Subtle Polymer Donor and Molecular Acceptor Design Enable Efficient Polymer Solar Cells with a Very Small Energy Loss. *Adv. Funct. Mater.* **2020**, *1907570*, 1–9. <https://doi.org/10.1002/adfm.201907570>.
- (48) Lv, M.; Li, S.; Jasieniak, J. J.; Hou, J.; Zhu, J.; Tan, Z.; Watkins, S. E.; Li, Y.; Chen, X. A Hyperbranched Conjugated Polymer as the Cathode

- Interlayer for High-Performance Polymer Solar Cells. *Adv. Mater.* **2013**, 25 (47), 6889–6894. <https://doi.org/10.1002/adma.201302726>.
- (49) Brabec, B. C. J.; Cravino, A.; Meissner, D.; Sariciftci, N. S.; Fromherz, T.; Rispen, M. T.; Sanchez, L.; Hummelen, J. C. Origin of the Open Circuit Voltage of Plastic Solar Cells. *Adv. Funct. Mater.* **2001**, 11 (5), 374–380.
- (50) Yu, G.; Gao, J.; Hummelen, J. C.; Wudl, F.; Heeger, A. J. Device Structure Consisted Polymer Photovoltaic Cells : Enhanced Efficiencies via a (Ca The on a g || G. *Science* (80-.). **1995**, 270, 1789–1791. <https://doi.org/10.1126/science.270.5243.1789>.
- (51) Rwenyagila, E. R. Review Article A Review of Organic Photovoltaic Energy Source and Its. *Int. J. Photoenergy* **2017**, 2017, 1–12. <https://doi.org/10.1155/2017/1656512>.
- (52) Koster, L. J. A.; Mihailetschi, V. D.; Ramaker, R.; Blom, P. W. M. Light Intensity Dependence of Open-Circuit Voltage of Polymer:Fullerene Solar Cells. *Appl. Phys. Lett.* **2005**, 86 (12), 1–3. <https://doi.org/10.1063/1.1889240>.
- (53) Jiang, J.; Chen, H.; Lin, H.; Yu, C.; Lan, S. Polymer Chemistry Benzooxadiazole – Diketopyrrolopyrrole with Full Visible Light Absorption for Bulk Heterojunction Solar Cells. *Polym. Chem.* **2013**, 4, 5321–5328. <https://doi.org/10.1039/c3py00132f>.

- (54) Gilles Dennler; Scharber, M. C.; Brabec, C. J. Polymer-Fullerene Bulk-Heterojunction Solar Cells. *Adv. Mater.* **2009**, *21*, 1323.
<https://doi.org/DOI: 10.1002/adma.200801283>.
- (55) Kim, M.; Kim, B.; Kim, J. Effective Variables To Control the Fill Factor of Organic Photovoltaic Cells. *ACS Appl. Mater. Interfaces* **2009**, *1* (6), 1264–1269. <https://doi.org/10.1021/am900155y>.
- (56) Chen, H.; Hou, J.; Zhang, S.; Liang, Y.; Yang, G.; Yang, Y. Polymer Solar Cells with Enhanced Open-Circuit Voltage and Efficiency. *Nat. Photonics* **2009**, *3* (November), 649–653.
<https://doi.org/10.1038/NPHOTON.2009.192>.
- (57) Piliego, C.; Holcombe, T. W.; Douglas, J. D.; Woo, C. H.; Beaujuge, P. M.; Fre, J. M. J. Synthetic Control of Structural Order in N-Alkylthieno [3,4-c] Pyrrole-4,6-Dione-Based Polymers for Efficient Solar Cells. *J. Am. Chem. Soc.* **2010**, *132*, 7595–7597.
- (58) Zhao, B. G.; He, Y.; Li, Y. 6.5 % Efficiency of Polymer Solar Cells Based on by Device Optimization. *Adv. Mater.* **2010**, *22*, 4355–4358.
<https://doi.org/10.1002/adma.201001339>.
- (59) Duan, C.; Zhang, K.; Guan, X.; Zhong, C.; Xie, H.; Huang, F.; Chen, J.; Peng, J.; Cao, Y. Conjugated Zwitterionic Polyelectrolyte-Based Interface Modification Materials for High Performance Polymer

- Optoelectronic Devices. *Chem. Sci.* **2013**, 4 (3), 1298–1307.
<https://doi.org/10.1039/c3sc22258f>.
- (60) Yip, H.; Jen, A. K. Environmental Science Recent Advances in Solution-Processed Interfacial Materials for Efficient and Stable Polymer Solar Cells. *Energy Environ. Sci.* **2012**, 5, 5994–6011.
<https://doi.org/10.1039/c2ee02806a>.
- (61) TT, D.; HS, H.; YE, H.; SI, Y.; YS, W.; MJ, M.; JH, K. Synthesis and Characterization of Conjugated Oligoelectrolytes Based on Fluorene and Carbazole Derivative and Application of Polymer Solar Cell as a Cathode Buffer Layer. *Macromol. Res.* **2015**, 23 (4), 367–376.
<https://doi.org/10.1007/s13233-015-3042-0>.
- (62) Zhang, L.; Liu, C.; Lai, T.; Huang, H.; Peng, X.; Huang, F. Small Molecule as a Cathode Interfacial Layer for Efficient Organic Photovoltaics †. *J. Mater. Chem. A* **2016**, 4, 15156–15161.
<https://doi.org/10.1039/c6ta05726h>.
- (63) Li, Y. L.; Cheng, Y. S.; Yeh, P. N.; Liao, S. H.; Chen, S. A. Structure Tuning of Crown Ether Grafted Conjugated Polymers as the Electron Transport Layer in Bulk-Heterojunction Polymer Solar Cells for High Performance. *Adv. Funct. Mater.* **2014**, 24 (43), 6811–6817.
<https://doi.org/10.1002/adfm.201401428>.

- (64) Li, G.; Zhu, R.; Yang, Y. Nphoton.2012.11.Pdf. *Nat. Photonics* **2012**, 6, 153–161. <https://doi.org/10.1038/nphoton.2012.11>.
- (65) He, Z.; Zhong, C.; Huang, X.; Wong, W.; Wu, H. Simultaneous Enhancement of Open-Circuit Voltage , Short-Circuit Current Density , and Fill Factor in Polymer Solar Cells. *Adv. Mater.* **2011**, 23, 4636–4643. <https://doi.org/10.1002/adma.201103006>.
- (66) Zhang, X.; Chen, X.; Huang, S.; Peng, X. Fluorene Dimers as the Cathode Interlayers in Organic Solar Cells. *Synth. Met.* **2019**, 253 (March), 110–115. <https://doi.org/10.1016/j.synthmet.2019.05.007>.
- (67) Page, Z. A.; Liu, Y.; Duzhko, V. V. Fulleropyrrolidine Interlayers: Tailoring Electrodes to Raise Organic Solar Cell Efficiency. *Science* (80-.). **2014**, 346 (6208), 441–444.
- (68) Xu, G.; Gao, L.; Xu, H.; Huang, L.; Xie, Y.; Cheng, X.; Li, Y.; Chen, L.; Chen, Y. N-Type Conjugated Electrolytes Cathode Interlayer with Thickness-Insensitivity for Highly Efficient Organic Solar Cells. *J. Mater. Chem. A* **2017**, 5 (26), 13807–13816. <https://doi.org/10.1039/c7ta02444d>.
- (69) Jin, H. C.; Salma, S. A.; Moon, D. K.; Kim, J. H. Effect of Conjugated Polymer Electrolytes with Diverse Acid Derivatives as a Cathode Buffer Layer on Photovoltaic Properties. *J. Mater. Chem. A* **2020**, 8 (8), 4562–4569. <https://doi.org/10.1039/c9ta12931f>.

- (70) Kim, Y. H.; Sylvianti, N.; Marsya, M. A.; Park, J.; Kang, Y. C.; Moon, D. K.; Kim, J. H. A Simple Approach to Fabricate an Efficient Inverted Polymer Solar Cell with a Novel Small Molecular Electrolyte as the Cathode Buffer Layer. *ACS Appl. Mater. Interfaces* **2016**, 8 (48), 32992–32997. <https://doi.org/10.1021/acsami.6b08628>.
- (71) Kim, Y. H.; Kim, D. G.; Maduwu, R. D.; Jin, H. C.; Moon, D. K.; Kim, J. H. Organic Electrolytes Doped ZnO Layer as the Electron Transport Layer for Bulk Heterojunction Polymer Solar Cells. **2018**, 2, 1800086. <https://doi.org/10.1002/solr.201800086>.
- (72) Kim, D. G.; Kim, Y. H.; Maduwu, R. D.; Jin, H. C.; Moon, D. K.; Kim, J. H. Organic Electrolyte Hybridized ZnO as the Electron Transport Layer for Inverted Polymer Solar Cells. *J. Ind. Eng. Chem.* **2018**, 65, 175. <https://doi.org/10.1016/j.jiec.2018.04.026>.
- (73) Jeong, M.; Jin, H. C.; Moon, D. K.; Kim, J. H. Simple Approach to Overcome Thickness Tolerance of Interlayer without Sacrificing the Performances of Polymer Solar Cells. *Adv. Mater. Interfaces* **2019**, 6 (18), 1–7. <https://doi.org/10.1002/admi.201900797>.
- (74) Jeong, M.; Jin, H. C.; Lee, J. H.; Moon, D. K.; Kim, J. H. Effect of Interface Modification in Polymer Solar Cells_ An In-Depth Investigation of the Structural Variation of Organic Dye for Interlayer

- Material _ Elsevier Enhanced Reader.Pdf. *Dye. Pigment.* **2020**, *173*, 107927.
- (75) Arroyo-Villan, M. I.; Diaz-Quijada, G. A.; Abdou, M. S. A.; Holdcroft, S. Poly(n-(3-Thienyl)Alkanesulfonates): Synthesis, Regioregularity, Morphology, and Photochemistry. *Macromolecules* **1995**, *28* (4), 975–984. <https://doi.org/10.1021/ma00108a027>.
- (76) Ahmed, M. Ultra High Resolution Crystallography of Small Molecules and Proteins, Université de Lorraine, 2018. hal.univ-lorraine.fr/tel-01749192.
- (77) Canestraro, C. D.; Rodrigues, P. C.; Marchiori, C. F. N.; Schneider, C. B.; Akcelrud, L.; Koehler, M.; Roman, L. S. The Role of the Double Peaked Absorption Spectrum in the Efficiency of Solar Cells Based on Donor-Acceptor-Donor Copolymers. *Sol. Energy Mater. Sol. Cells* **2011**, *95* (8), 2287–2294. <https://doi.org/10.1016/j.solmat.2011.03.043>.
- (78) M.J. Frisch, G.W. Trucks, H.B. Schlegel, G.E. Scuseria, M.A. Robb, J.R. Cheeseman, J.A. Montgomery Jr., T. Vreven, K.N. Kudin, J.C. Burant, J.M. Millam, S.S. Iyengar, J. Tomasi, V. Barone, B. Mennucci, M. Cossi, G. Scalmani, N. Rega, G.A. Petersson, H. Na, 2004. Gaussian"16 {R}evision {C}.01. 2016, p Gaussian Inc. Wallingford CT.

- (79) Franco, I.; Tretiak, S. Electron-Vibrational Dynamics of Photoexcited Polyfluorenes. *J. Am. Chem. Soc.* **2004**, *126* (38), 12130–12140. <https://doi.org/10.1021/ja0489285>.
- (80) Reza, K. M.; Gurung, A.; Bahrami, B.; Mabrouk, S.; Elbohy, H.; Pathak, R.; Chen, K.; Chowdhury, A. H.; Rahman, M. T.; Letourneau, S.; Yang, H. C.; Saianand, G.; Elam, J. W.; Darling, S. B.; Qiao, Q. Tailored PEDOT:PSS Hole Transport Layer for Higher Performance in Perovskite Solar Cells: Enhancement of Electrical and Optical Properties with Improved Morphology. *J. Energy Chem.* **2020**, *44*, 41–50. <https://doi.org/10.1016/j.jechem.2019.09.014>.
- (81) Knaapila, M.; Konôpková, Z.; Torkkeli, M.; Haase, D.; Liermann, H. P.; Guha, S.; Scherf, U. Structural Study of Helical Polyfluorene under High Quasihydrostatic Pressure. *Phys. Rev. E - Stat. Nonlinear, Soft Matter Phys.* **2013**, *87* (2), 1–9. <https://doi.org/10.1103/PhysRevE.87.022602>.
- (82) Zhang, Z. G.; Qi, B.; Jin, Z.; Chi, D.; Qi, Z.; Li, Y.; Wang, J. Perylene Diimides: A Thickness-Insensitive Cathode Interlayer for High Performance Polymer Solar Cells. *Energy Environ. Sci.* **2014**, *7* (6), 1966–1973. <https://doi.org/10.1039/c4ee00022f>.
- (83) Burkhard, G. F.; Hoke, E. T.; McGehee, M. D. Accounting for Interference, Scattering, and Electrode Absorption to Make Accurate

Internal Quantum Efficiency Measurements in Organic and Other Thin Solar Cells. *Adv. Mater.* **2010**, 22 (30), 3293–3297.
<https://doi.org/10.1002/adma.201000883>.

- (84) Zhang, X.; Hägglund, C.; Johansson, E. M. J. Electro-Optics of Colloidal Quantum Dot Solids for Thin-Film Solar Cells. *Adv. Funct. Mater.* **2016**, 26 (8), 1253–1260.
<https://doi.org/10.1002/adfm.201503338>.
- (85) Mubarak, M. Al; Aqoma, H.; Tri, F.; Wibowo, A.; Lee, W.; Kim, H. M.; Ryu, D. Y.; Jeon, J.; Jang, S. Molecular Engineering in Hole Transport π -Conjugated Polymers to Enable High Efficiency Colloidal Quantum Dot Solar Cells. *Adv. Energy Mater.* **2020**, 1902933, 1–9.
<https://doi.org/10.1002/aenm.201902933>.
- (86) Zhang, K.; Fan, B.; Xia, R.; Liu, X.; Hu, Z.; Gu, H.; Liu, S.; Yip, H. L.; Ying, L.; Huang, F.; Cao, Y. Highly Efficient Tandem Organic Solar Cell Enabled by Environmentally Friendly Solvent Processed Polymeric Interconnecting Layer. *Adv. Energy Mater.* **2018**, 8 (15), 1–9.
<https://doi.org/10.1002/aenm.201703180>.
- (87) Kitova, S.; Stoyanova, D.; Dikova, J.; Kandinska, M.; Vasilev, A.; Angelova, S. Optical Modeling of Bulk-Heterojunction Organic Solar Cells Based on Squaraine Dye as Electron Donor. *J. Phys. Conf. Ser.* **2014**, 558 (1). <https://doi.org/10.1088/1742-6596/558/1/012052>.

- (88) Zilberberg, K.; Behrendt, A.; Kraft, M.; Scherf, U.; Riedl, T. Ultrathin Interlayers of a Conjugated Polyelectrolyte for Low Work-Function Cathodes in Efficient Inverted Organic Solar Cells. *Org. Electron.* **2013**, *14* (3), 951–957. <https://doi.org/10.1016/j.orgel.2013.01.018>.
- (89) Bini, K.; Xu, X.; Andersson, M. R.; Wang, E. Alcohol-Soluble Conjugated Polymers as Cathode Interlayers for All-Polymer Solar Cells. *ACS Appl. Energy Mater.* **2018**, *1* (5), 2176–2182. <https://doi.org/10.1021/acsaem.8b00225>.
- (90) He, Z.; Wu, H.; Cao, Y. Recent Advances in Polymer Solar Cells: Realization of High Device Performance by Incorporating Water/Alcohol-Soluble Conjugated Polymers as Electrode Buffer Layer. *Adv. Mater.* **2014**, *26* (7), 1006–1024. <https://doi.org/10.1002/adma.201303391>.
- (91) Zhou, Y.; Fuentes-Hernandez, C.; Shim, J.; Meyer, J.; Giordano, A. J.; Li, H.; Winget, P.; Papadopoulos, T.; Cheun, H.; Kim, J.; Fenoll, M.; Dindar, A.; Haske, W.; Najafabadi, E.; Khan, T. M.; Sojoudi, H.; Barlow, S.; Graham, S.; Brédas, J. L.; Marder, S. R.; Kahn, A.; Kippelen, B. A Universal Method to Produce Low-Work Function Electrodes for Organic Electronics. *Science* (80-.). **2012**, *336* (6079), 327–332. <https://doi.org/10.1126/science.1218829>.

- (92) Van Reenen, S.; Kouijzer, S.; Janssen, R. A. J.; Wienk, M. M.; Kemerink, M. Origin of Work Function Modification by Ionic and Amine-Based Interface Layers. *Adv. Mater. Interfaces* **2014**, *1* (8), 1–11. <https://doi.org/10.1002/admi.201400189>.
- (93) Wang, C.; Luo, Y.; Zheng, J.; Liu, L.; Xie, Z.; Huang, F.; Yang, B.; Ma, Y. Spontaneous Interfacial Dipole Orientation Effect of Acetic Acid Solubilized PFN. *ACS Appl. Mater. Interfaces* **2018**, *10* (12), 10270–10279. <https://doi.org/10.1021/acsami.8b00975>.
- (94) Lim, K. G.; Park, S. M.; Woo, H. Y.; Lee, T. W. Elucidating the Role of Conjugated Polyelectrolyte Interlayers for High-Efficiency Organic Photovoltaics. *ChemSusChem* **2015**, *8* (18), 3062–3068. <https://doi.org/10.1002/cssc.201500631>.
- (95) Hu, Z.; Zhang, K.; Huang, F.; Cao, Y. Water/Alcohol Soluble Conjugated Polymers for the Interface Engineering of Highly Efficient Polymer Light-Emitting Diodes and Polymer Solar Cells. *Chem. Commun.* **2015**, *51* (26), 5572–5585. <https://doi.org/10.1039/c4cc09433f>.
- (96) Ratcliff, E. L.; Zacher, B.; Armstrong, N. R. Selective Interlayers and Contacts in Organic Photovoltaic Cells. *J. Phys. Chem. Lett.* **2011**, *2* (11), 1337–1350. <https://doi.org/10.1021/jz2002259>.

- (97) Park, J.; Yang, R.; Hoven, C. V.; Garcia, A.; Fischer, D. A.; Nguyen, T. Q.; Bazan, G. C.; Delongchamp, D. M. Structural Characterization of Conjugated Polyelectrolyte Electron Transport Layers by NEXAFS Spectroscopy. *Adv. Mater.* **2008**, *20* (13), 2491–2496.
<https://doi.org/10.1002/adma.200702995>.
- (98) Jo, M. Y.; Do, T. T.; Ha, Y. E.; Won, Y. S.; Kim, J. H. Enhanced Efficiency in Polymer Solar Cells by Incorporation of Phenothiazine-Based Conjugated Polymer Electrolytes. *Org. Electron.* **2015**, *16*, 18–25. <https://doi.org/10.1016/j.orgel.2014.10.042>.
- (99) Jo, M. Y.; Ha, Y. E.; Won, Y. S.; Yoo, S. Il; Kim, J. H. Effect of Side Chain Arrangement of Conjugated Polyelectrolytes Buffer Layer on the Photovoltaic Properties. *Org. Electron.* **2015**, *25*, 85–91.
<https://doi.org/10.1016/j.orgel.2015.06.014>.
- (100) Young Jo, M.; Eun Ha, Y.; Hyun Kim, J. Polyviologen Derivatives as an Interfacial Layer in Polymer Solar Cells. *Sol. Energy Mater. Sol. Cells* **2012**, *107*, 1–8. <https://doi.org/10.1016/j.solmat.2012.08.003>.
- (101) Do, T. T.; Bae, J. H.; Yoo, S. Il; Lim, K. T.; Woo, H. Y.; Kim, J. H. Synthesis and Characterization of π -Conjugated Polymers Based on 2-Arylbenzimidazole and 4,7-Di-Thiophene-2-Yl-4,5,6,7-Tetrahydro-Benzo[1,2,5] Thiadiazole. *Mol. Cryst. Liq. Cryst.* **2013**, *581* (1), 31–37.
<https://doi.org/10.1080/15421406.2013.808145>.

- (102) Bagui, A.; Iyer, S. S. K. Increase in Hole Mobility in Poly (3-Hexylthiophene-2,5-Diyl) Films Annealed under Electric Field during the Solvent Drying Step. *Org. Electron.* **2014**, *15* (7), 1387–1395.
<https://doi.org/10.1016/j.orgel.2014.03.042>.
- (103) Park, S.; Jang, W.; Wang, D. H. Alignment of Cascaded Band-Gap via PCBM/ZnO Hybrid Interlayers for Efficient Perovskite Photovoltaic Cells. *Macromol. Res.* **2018**, *26* (5), 472–476.
<https://doi.org/10.1007/s13233-018-6086-0>.
- (104) Shen, P.; Yao, M.; Wang, G.; Mi, R.; Guo, W.; Bai, Y.; Shen, L. High-Efficiency Polymer Solar Cells with Low Temperature Solution-Processed SnO₂/PFN as a Dual-Function Electron Transporting Layer. *J. Mater. Chem. A* **2018**, *6* (36), 17401–17408.
<https://doi.org/10.1039/c8ta06378h>.
- (105) Qi, B.; Zhang, Z. G.; Wang, J. Uncovering the Role of Cathode Buffer Layer in Organic Solar Cells. *Sci. Rep.* **2015**, *5*, 1–8.
<https://doi.org/10.1038/srep07803>.
- (106) Jia, X.; Jiang, Z.; Chen, X.; Zhou, J.; Pan, L.; Zhu, F.; Sun, Z.; Huang, S. Highly Efficient and Air Stable Inverted Polymer Solar Cells Using LiF-Modified ITO Cathode and MoO₃/AgAl Alloy Anode. *ACS Appl. Mater. & Interfaces* **2016**, *8* (6), 3792–3799.
<https://doi.org/10.1021/acsami.5b10240>.

- (107) Nho, S.; Baek, G.; Park, S.; Lee, B. R.; Cha, M. J.; Lim, D. C.; Seo, J. H.; Oh, S. H.; Song, M. H.; Cho, S. Highly Efficient Inverted Bulk-Heterojunction Solar Cells with a Gradiently-Doped ZnO Layer. *Energy Environ. Sci.* **2016**, 9 (1), 240–246. <https://doi.org/10.1039/c5ee03045e>.
- (108) Liu, H.; Huang, L.; Cheng, X.; Hu, A.; Xu, H.; Chen, L.; Chen, Y. N-Type Self-Doping of Fluorinate Conjugated Polyelectrolytes for Polymer Solar Cells: Modulation of Dipole, Morphology, and Conductivity. *ACS Appl. Mater. Interfaces* **2017**, 9 (1), 1145–1153. <https://doi.org/10.1021/acsami.6b15678>.
- (109) Li, Y.; Li, X.; Liu, X.; Zhu, L.; Zhang, W.; Fang, J. Realizing High Performance Inverted Organic Solar Cells via a Nonconjugated Electrolyte Cathode Interlayer. *J. Phys. Chem. C* **2016**, 120 (46), 26244–26248. <https://doi.org/10.1021/acs.jpcc.6b10558>.
- (110) Rainer, K.; Sastrawan, R.; Ferber, J.; Stangl, R.; Luther, J. Modeling and Interpretation of Electrical Impedance Spectra of Dyesolar Cells Operated under Open-Circuit Condition. *Electrochim. Acta* **2002**, No. 47, 4213–4425. [https://doi.org/https://doi.org/10.1016/S0013-4686\(02\)00444-9](https://doi.org/10.1016/S0013-4686(02)00444-9).
- (111) Sankar, K. V.; Selvan, R. K. The Preparation of MnFe₂O₄ Decorated Flexible Graphene Wrapped with PANI and Its Electrochemical

- Performances for Hybrid Supercapacitors. *RSC Adv.* **2014**, *4* (34), 17555–17566. <https://doi.org/10.1039/c3ra47681b>.
- (112) Qu, Q.; Zhang, P.; Wang, B.; Chen, Y.; Tian, S.; Wu, Y.; Holze, R. Electrochemical Performance of MnO₂ Nanorods in Neutral Aqueous Electrolytes as a Cathode for Asymmetric Supercapacitors. *J. Phys. Chem. C* **2009**, *113* (31), 14020–14027. <https://doi.org/10.1021/jp8113094>.
- (113) Huang, Y.; Li, Y.; Hu, Z.; Wei, G.; Guo, J.; Liu, J. A Carbon Modified MnO₂ Nanosheet Array as a Stable High-Capacitance Supercapacitor Electrode. *J. Mater. Chem. A* **2013**, *1* (34), 9809–9813. <https://doi.org/10.1039/c3ta12148h>.
- (114) Toyohisa, H.; Ryuji, K.; Kazunari, S.; Koichi, E. Impedance Analysis of Electronic Transport in DSSC. *Electrochemistry* **2002**, *70*, 675. <https://doi.org/https://doi.org/10.5796/electrochemistry.70.675>.
- (115) Li, Y. Molecular Design of Photovoltaic Materials for Polymer Solar Cells: Toward Suitable Electronic Energy Levels and Broad Absorption. *Acc. Chem. Res.* **2012**, *45* (5), 723–733. <https://doi.org/10.1021/ar2002446>.
- (116) Zhang, W.; Wu, Y.; Bao, Q.; Gao, F.; Fang, J. Morphological Control for Highly Efficient Inverted Polymer Solar Cells via the Backbone

- Design of Cathode Interlayer Materials. *Adv. Energy Mater.* **2014**, 4 (12). <https://doi.org/10.1002/aenm.201400359>.
- (117) Handoko, S. L.; Jin, H. C.; Whang, D. R.; Kim, J. H.; Chang, D. W. Effect of Cyano Substituent on Photovoltaic Properties of Quinoxaline-Based Polymers. *J. Ind. Eng. Chem.* **2020**, 86, 244–250. <https://doi.org/10.1016/j.jiec.2020.03.018>.
- (118) Handoko, S. L.; Jin, H. C.; Whang, D. R.; Putri, S. K.; Kim, J. H.; Chang, D. W. Synthesis of Quinoxaline-Based Polymers with Multiple Electron-Withdrawing Groups for Polymer Solar Cells. *J. Ind. Eng. Chem.* **2019**, 73, 192–197. <https://doi.org/10.1016/j.jiec.2019.01.024>.
- (119) Wu, Z.; Sun, C.; Dong, S.; Jiang, X. F.; Wu, S.; Wu, H.; Yip, H. L.; Huang, F.; Cao, Y. N-Type Water/Alcohol-Soluble Naphthalene Diimide-Based Conjugated Polymers for High-Performance Polymer Solar Cells. *J. Am. Chem. Soc.* **2016**, 138 (6), 2004–2013. <https://doi.org/10.1021/jacs.5b12664>.
- (120) Reddy, S. S.; Aryal, U. K.; Jin, H.; Gokulnath, T.; Rajalapati, D. G.; Kranthiraja, K.; Shin, S. T.; Jin, S. H. A New Benzodithiophene Based Donor-Acceptor π -Conjugated Polymer for Organic Solar Cells. *Macromol. Res.* **2020**, 28 (2), 179–183. <https://doi.org/10.1007/s13233-020-8079-z>.

- (121) Lee, S.; Ha, J. W.; Park, H. J.; Hwang, D. H. Synthesis and Characterization of Benzotriazole-Based Polymer Donors with Good Planarity for Organic Photovoltaics. *Macromol. Res.* **2020**, 903–909. <https://doi.org/10.1007/s13233-020-8124-y>.
- (122) Cha, H.; Li, J.; Li, Y.; Kim, S.-O.; Kim, Y.-H.; Kwon, S.-K. Effects of Bulk Heterojunction Morphology Control via Thermal Annealing on the Fill Factor of Anthracene-Based Polymer Solar Cells. *Macromol. Res.* **2020**, 28 (9), 820–825. <https://doi.org/10.1007/s13233-020-8107-z>.
- (123) Koster, L. J. A.; Smits, E. C. P.; Mihailetschi, V. D.; Blom, P. W. M. Device Model for the Operation of Polymer / Fullerene Bulk Heterojunction Solar Cells. *Phys. Rev. B* **2005**, 72 (March), 085205. <https://doi.org/10.1103/PhysRevB.72.085205>.
- (124) Abdullah; Akhtar, M. S.; Kim, E. B.; Fijahi, L.; Shin, H. S.; Ameen, S. A Symmetric Benzoselenadiazole Based D–A–D Small Molecule for Solution Processed Bulk-Heterojunction Organic Solar Cells. *J. Ind. Eng. Chem.* **2020**, 81, 309–316. <https://doi.org/10.1016/j.jiec.2019.09.019>.
- (125) Cheng, Y. J.; Yang, S. H.; Hsu, C. S. Synthesis of Conjugated Polymers for Organic Solar Cell Applications. *Chem. Rev.* **2009**, 109 (11), 5868–5923. <https://doi.org/10.1021/cr900182s>.

- (126) Bini, K.; Xu, X.; Andersson, M. R.; Wang, E. Alcohol-Soluble Conjugated Polymers as Cathode Interlayers for All-Polymer Solar Cells. *ACS Appl. Energy Mater.* **2018**, *1* (5), 2176–2182. <https://doi.org/10.1021/acsaem.8b00225>.
- (127) Song, C. E.; Ryu, K. Y.; Hong, S. J.; Bathula, C.; Lee, S. K.; Shin, W. S.; Lee, J. C.; Choi, S. K.; Kim, J. H.; Moon, S. J. Enhanced Performance in Inverted Polymer Solar Cells with D- π -A-Type Molecular Dye Incorporated on ZnO Buffer Layer. *ChemSusChem* **2013**, *6* (8), 1445–1454. <https://doi.org/10.1002/cssc.201300240>.
- (128) Chua, L.; Zaumseil, J.; Chang, J.; Ou, E. C. 2005Chua Sirringhaus Friend Nature General Observation of N-Type Field-Effect Behaviour in Organic Semiconductors_JZ.Pdf. *Nature* **2005**, *434* (March), 194–199. <https://doi.org/10.1038/nature03293.1>.
- (129) Cheng, Y. J.; Hsieh, C. H.; He, Y.; Hsu, C. S.; Li, Y. Combination of Indene-C60 Bis-Adduct and Cross-Linked Fullerene Interlayer Leading to Highly Efficient Inverted Polymer Solar Cells. *J. Am. Chem. Soc.* **2010**, *132* (49), 17381–17383. <https://doi.org/10.1021/ja108259n>.
- (130) Sun, Y.; Seo, J. H.; Takacs, C. J.; Seifert, J.; Heeger, A. J. Inverted Polymer Solar Cells Integrated with a Low-Temperature-Annealed Sol-Gel-Derived ZnO Film as an Electron Transport Layer. *Adv. Mater.* **2011**, *23* (14), 1679–1683. <https://doi.org/10.1002/adma.201004301>.

- (131) Duan, C.; Zhang, K.; Zhong, C.; Huang, F.; Cao, Y. *Chem Soc Rev.*
Chem Soc Rev **2013**, *42*, 9071–9104.
<https://doi.org/10.1039/c3cs60200a>.
- (132) Chueh, C.; Li, C.; Jen, A. K. Environmental Science Recent Progress
and Perspective in Solution- Processed Interfacial Materials for e Ffi
Cient and Stable Polymer and Organometal Perovskite Solar Cells.
energy and **2015**, *8*, 1160–1189. <https://doi.org/10.1039/c4ee03824j>.
- (133) Do, T. T.; Hong, H. S.; Ha, Y. E.; Yoo, S. Il; Won, Y. S.; Moon, M. J.;
Kim, J. H. Synthesis and Characterization of Conjugated
Oligoelectrolytes Based on Fluorene and Carbazole Derivative and
Application of Polymer Solar Cell as a Cathode Buffer Layer.
Macromol. Res. **2015**, *23* (4), 367–376. <https://doi.org/10.1007/s13233-015-3042-0>.
- (134) Kang, R.; Oh, S. H.; Kim, D. Y. Influence of the Ionic Functionalities
of Polyfluorene Derivatives as a Cathode Interfacial Layer on Inverted
Polymer Solar Cells. *ACS Appl. Mater. Interfaces* **2014**, *6* (9), 6227–
6236. <https://doi.org/10.1021/am500708k>.
- (135) Liu, Y.; Page, Z. A.; Russell, T. P.; Emrick, T. Finely Tuned Polymer
Interlayers Enhance Solar Cell Efficiency. *Angew. Chemie - Int. Ed.*
2015, *54* (39), 11485–11489. <https://doi.org/10.1002/anie.201503933>.

- (136) Seo, J. H.; Gutacker, A.; Sun, Y.; Wu, H.; Huang, F.; Cao, Y.; Scherf, U.; Heeger, A. J.; Bazan, G. C. Improved High-Efficiency Organic Solar Cells via Incorporation of a Conjugated Polyelectrolyte Interlayer. *J. Am. Chem. Soc.* **2011**, *133* (22), 8416–8419.
<https://doi.org/10.1021/ja2037673>.
- (137) Jeong, M.; Jin, H. C.; Moon, D. K.; Kim, J. H. Simple Approach to Overcome Thickness Tolerance of Interlayer without Sacrificing the Performances of Polymer Solar Cells. *Adv. Mater. Interfaces* **2019**, *1900797* (6), 1–7. <https://doi.org/10.1002/admi.201900797>.
- (138) Huang, F.; Hou, L.; Shen, H.; Jiang, J.; Wang, F.; Zhen, H.; Cao, Y. Synthesis, Photophysics, and Electroluminescence of High-Efficiency Saturated Red Light-Emitting Polyfluorene-Based Polyelectrolytes and Their Neutral Precursors. *J. Mater. Chem.* **2005**, *15* (25), 2499–2507.
<https://doi.org/10.1039/b503920g>.
- (139) Huang, F.; Wu, H.; Wang, D.; Yang, W.; Cao, Y. Novel Electroluminescent Conjugated Polyelectrolytes Based on Polyfluorene. *Chem. Mater.* **2004**, *16* (4), 708–716.
<https://doi.org/10.1021/cm034650o>.
- (140) Huang, F.; Wu, H.; Peng, J.; Yang, W.; Cao, Y. Polyfluorene Polyelectrolytes and Their Precursors Processable from Environment-Friendly Solvents (Alcohol or Water) for PLED Applications. *Curr.*

Org. Chem. **2007**, *11* (14), 1207–1219.

<https://doi.org/10.2174/138527207781696017>.

- (141) Yin, Z.; Wei, J.; Zheng, Q. Interfacial Materials for Organic Solar Cells:

Recent Advances and Perspectives. *Adv. Sci.* **2016**, *3* (8), 1–37.

<https://doi.org/10.1002/advs.201500362>.

- (142) Jia, X.; Jiang, Z.; Chen, X.; Zhou, J.; Pan, L.; Zhu, F.; Sun, Z.; Huang,

S. Highly Efficient and Air Stable Inverted Polymer Solar Cells Using LiF-Modified ITO Cathode and MoO₃/AgAl Alloy Anode. *ACS Appl. Mater. Interfaces* **2016**, *8* (6), 3792–3799.

<https://doi.org/10.1021/acsami.5b10240>.

- (143) Jin, H. C.; Salma, S. A.; Moon, D. K.; Kim, J. H. Effect of Conjugated

Polymer Electrolytes with Diverse Acid Derivatives as a Cathode

Buffer Layer on Photovoltaic Properties. *J. Mater. Chem. A* **2020**, *8* (8),

4562–4569. <https://doi.org/10.1039/C9TA12931F>.

Acknowledgement

Alhamdulillah Rabbil Alamin, Thanks to merciful Lord, Allah SWT for the countless rahmah that have offered me which can strengthen me during my study in Pukyong National University.

I would like to say a special thank you to my supervisor, Prof Joo Hyun Kim's support, guidance and overall insights in this field have made this an inspiring experience for me.

From the bottom of my heart, I would like to say big thank you for all the OOM lab research group members for their energy, understanding and help throughout my project research, especially to Mr. Son Dong Hwan for the teamwork throughout the device fabrication. I would like to thank my fellow lab mates: Rahma, Ayuni, Indah, Young Seok, Gain, and Jueon. Their teamwork, caring and encouragement have been valuable to me survive in this laboratory. I'd also like to thank to all of my Indonesian friends, Astrini, Ajeng, Nurmaulia, Merreta, and Intan who took the time to supported me during my stressful time. I will be grateful forever for our friendship. And of course, to the party friends Brahma, Benny, Nicholas, Tony, Haris Gian and David. Thanks for cheering me up.

And to my parents Lilik and Feriko my brother Rian and Gilang, who set me off on the road to this pathway of Ph.D a long time ago. For my beloved husband who always be my side during this 8 years study time. Their support launched the greater part of the sustainability my life in this overseas country.